ISSN: 1949-243X (Print), 1947-3818 (Online)   Volume 1, Number 1, August 2009

Energy and Power Engineering

電力與能源 國際期刊

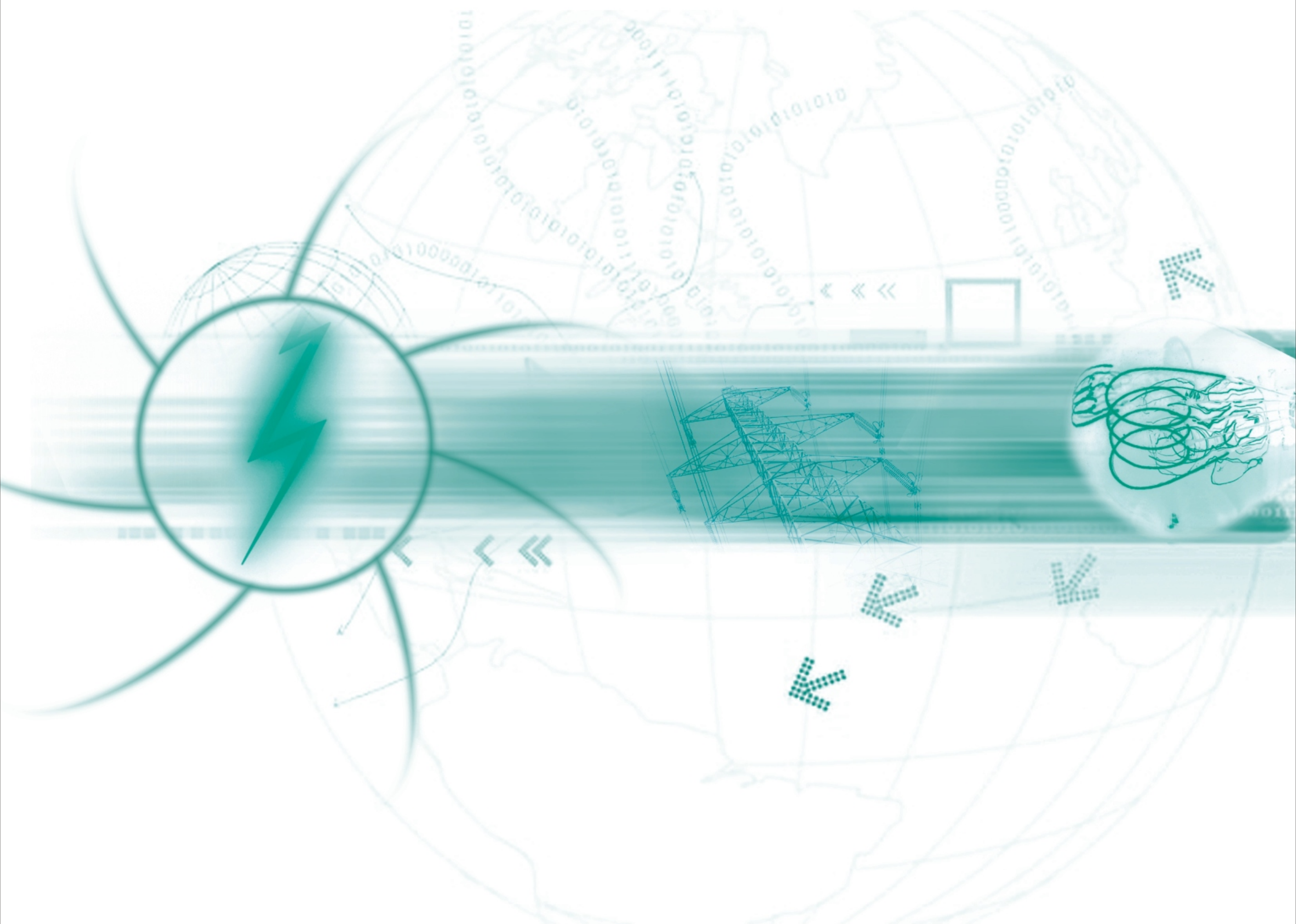

www.scirp.org/journal/epe

Scientific Research

Journal Editorial Board

ISSN: 1949-243X (Print) ISSN: 1947-3818 (Online)

http://www.scirp.org/journal/epe

Energy and Power Engineering, 2009, 01-64
http://www.scirp.org/journal/epe

Table of Contents

Energy and Power Engineering (EPE)

Journal Information

SUBSCRIPTIONS

Energy and Power Engineering (Online at Scientific Research Publishing, www.SciRP.org) is published quarterly by Scientific Research Publishing, Inc., USA.

E-mail: epe@scirp.org

Subscription rates: Volume 1 2009
Print: $50 per copy.
Electronic: free, available on www.SciRP.org.
To subscribe, please contact Journals Subscriptions Department, E-mail: epe@scirp.org

Sample copies: If you are interested in subscribing, you may obtain a free sample copy by contacting Scientific Research Publishing, Inc. at the above address.

SERVICES

Advertisements
Advertisement Sales Department, E-mail: epe@scirp.org

Reprints (minimum quantity 100 copies)
Reprints Co-ordinator, Scientific Research Publishing, Inc., USA.
E-mail: epe@scirp.org

COPYRIGHT

PRODUCTION INFORMATION

For manuscripts that have been accepted for publication, please contact:
E-mail: epe@scirp.org

Energy and Power Engineering, 2009, 01-06
doi:10.4236/epe.2009.11001 Published Online August 2009 (http://www.scirp.org/journal/epe)

Scientific Research

Anti-Icing Method Based on Reducing Voltage of Transmission Lines

Xiaoming LI[1], Junjie HUANG[1], Youbin ZhOU[2]
[1]*School of Electrical Engineering, Wuhan University, Wuhan, China*
[2]*Hubei Electric Power Testing & Research Institute, Wuhan, China*
Email: *huangjjhwb@yahoo.com.cn*

Abstract: The icing of transmission lines threatens the security of power system. This paper proposes a novel anti-icing method based on reducing voltage of the transmission lines. The line voltage can be reduced by regulating the ratio of the transformers which install the both ends of the transmission lines. The line current can be increased and the power loss of the transmission lines can also be increased, which means the heat generated by power loss increases and the icing process of the transmission lines can be restrained. When the icing may occur in the atrocious weather, the anti-icing transformers installed the both ends of transmission line are put into operation. The ratios of transformers are regulated to the appropriate value. The current of transmission line can be increased to the value that is a little greater than the critical current, which can realize the purpose of anti-icing. At the same time, the conditions of normal running in the load side are kept invariably, which can ensure the security of power system. This method can be applicable to a wide range. It's an effective measure to prevent the icing of the transmission lines.

Keywords: anti-icing, transformer, critical current

1 引 言

架空輸電線路覆冰對電力系統的安全運行有著很大影響，會使輸電線路發生舞動，因電氣距離不足而閃絡，甚至斷線倒塔。所以，在惡劣天氣時，必須採取措施防止線路覆冰情況的出現。

防覆冰方法是在覆冰前採取各種有效技術措施，使各種形式的冰在導線上無法積覆。與已經覆冰達到危險狀態再採取措施的除冰方法相比，防範于未然，對系統的安全、經濟運行更為有利。目前常用的防止架空輸電線路覆冰的方法有[1]:（1）在線路設計時，避免線路穿越易覆冰區域，但在實際中線路往往無法完全避開這些區域;（2）在導線表面塗抹憎水性材料，但迄今為止，還沒有一種可以根本阻止冰雪形成的塗料，憎水性塗料只能最大限度地減小冰與導線的結合力，使其易於脫落;（3）增加導線電流防覆冰，利用電流通過導線時，電阻產生的焦耳熱使導線表面溫度維持在 0℃以上，即可防止導線覆冰。最簡單的增加導線電流的方法是調節電網的潮流分佈，使需要防覆冰的導線上流過更大的電流，但是這種方法的調節電流大小有限，而且有可能影響使其他線路，使其出現過電流。有文獻採用的方法是在變電所母線上裝設足夠容量的並聯電容器或電抗器，實現增加線路上無功電流的目的[2]。但是，對於變電所母線接有多條進出線的情況，增加的無功電流有可能流過其他的導線，而不流過需要防覆冰的導線，使這一方法失效，並有可能使其他線路過熱。

針對這一情況，本文提出了一種輸電線路降壓運行防覆冰的控制策略。通過調節安裝在輸電線路兩端的防覆冰變壓器，在確保線路以外節點電壓不越限的前提下，降低導線的電壓，使流過導線的電流增加。導線因為線損增加而發熱，使覆冰過程得到抑制。如果防覆冰變壓器採用有載調壓，輪流調節線路兩側變壓器變比，可實現防覆冰控制過程負荷不停電。

2 防覆冰變壓器調壓原理

2.1 系統結構

輸電線路是否覆冰主要與氣象條件、負載大小等因素有關係[3]。一般而言，當負載較重時由於線路上

流過的電流大，使導線發熱多，線路覆冰就不容易形成。但是，在惡劣的氣象條件下，線路負載不一定大。甚至在風雪災害較嚴重的情況下，即使線路重負載運行，線路仍有覆冰的危險。在保證負載不變的情況下，增加線路的電流，就可以防止覆冰。

防覆冰系統的總體結構如圖 1 所示。圖中 A、B 分別為變電站母線，每條母線上除了有進出線之外，還安裝有一台覆冰變壓器，通過開關（斷路器）和母線的各條線路相連。有載調壓覆冰變壓器的額定變比為 1，通過調節分接頭，可以改變線路一側的電壓大小。正常運行的情況下，開關 S_{A1}、S_{B1} 閉合，其餘開關斷開，防覆冰變壓器不工作。通過對氣象條件、線路負載等情況的綜合分析，如果 AB 之間的輸電線路有可能覆冰時，防覆冰變壓器應該投入。變壓器的投入操作程式是：（1）斷開 S_{A1}、S_{B1}，母線 A、B 間的線路停電；（2）調整變壓器 T_A、T_B 的變比到合適的值；（3）閉合 S_{A2}、S_{B2}，相當於把變壓器空載投入；（4）閉合 S_{A3}、S_{B3}，輸電線路恢復供電。如採用的是有載調壓變壓器調壓，則可直接投入變壓器，為避免環流，應把變壓器的變比設為 1。然後通過合理的調節方式，使變壓器 T_A、T_B 的分接開關同步動作，降低輸電線路電壓，增大電流。

當天氣轉好，不需要防覆冰時，再將防覆冰變壓器退出。防覆冰變壓器的退出操作程式是投入操作程的逆過程。

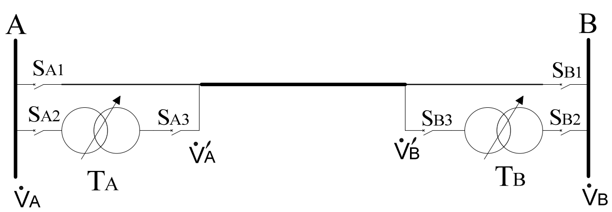

圖 1. 防覆冰系統結構圖

Figure 1. The structure of the anti-icing system

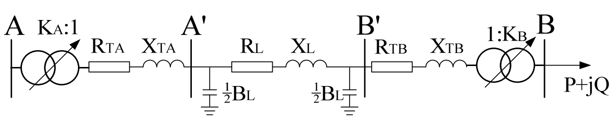

圖 2. 防覆冰系統等值電路圖

Figure 2. The equivalence circuit of the anti-icing system

2.2 防覆冰變壓器變比

圖 2 為防覆冰系統的等值電路圖，其中輸電線路用 π 型電路等值，變壓器用阻抗支路和理想變壓器串聯表示。

對於防覆冰變壓器，給出的阻抗為額定變比下的值，當變比為非額定時，阻抗值會發生改變。對調壓範圍較小的變壓器這個變化不明顯；而本文所述變壓器的額定變比為 1，調壓範圍可達到 30%～100%的額定電壓，所以阻抗值的變化較大，在等值電路中應作修正[4]。考慮到額定變比時變壓器一二次側繞組匝數相同，有

$$\begin{cases} R_T = \dfrac{1}{2}(1+k^2)R_{TN} \\ X_T = \dfrac{1}{2}(1+k^2)X_{TN} \end{cases} \quad (1)$$

其中 k 為變壓器實際變比，R_{TN}、X_{TN} 為額定變比下的變壓器電阻和電抗值。

設調壓之前，系統由母線 A 向母線 B 傳輸功率，母線 B 的輸出功率為 P+jQ，如圖 2 所示。調壓目標是使輸電線路的電流增加到一定值，確保線路不覆冰，同時維持母線 A 和 B 的電壓不變。

圖 2 中，母線 B 的電壓為 $\dot{V}_B$，相連的防覆冰變壓器變比為 k_B，流過的電流為：

$$\dot{I}_{TB} = \frac{P - jQ}{\tilde{V}_B} k_B \quad (2)$$

母線 B'的電壓為：

$$\dot{V}'_B = \frac{\dot{V}_B}{k_B} + \dot{I}_{TB}(R_{TB} + jX_{TB}) \quad (3)$$

輸電線路上的電流為：

$$\dot{I}_L = \dot{I}_{TB} + \dot{V}'_B \cdot j\frac{B_L}{2} \quad (4)$$

如果確定了線路導線不覆冰時流過的最小電流，即臨界電流 ILJ，則要求 $I_L \geq I_{LJ}$。由式(1)～(4)即可解出與母線 B 相連的變壓器變比 k_B 的大小。

母線 A'的電壓為：

$$\dot{V}'_A = \dot{V}'_B + \dot{I}_L(R_L + jX_L) \quad (5)$$

與母線 A 相連的防覆冰變壓器流過的電流為：

$$\dot{I}_{TA} = \dot{I}_L + \dot{V}'_A \cdot j\frac{B_L}{2} \tag{6}$$

母線 A 的電壓為：

$$\dot{V}_A = k_A[\dot{V}'_A + \dot{I}_{TA} \cdot (R_{TA} + jX_{TA})] \tag{7}$$

考慮到母線A的電壓大小在防覆冰變壓器投入前後不變，由式(5)～(7) 可解出與母線 A 相連的變壓器變比 k_A 的大小。

要注意的是，由於變壓器變比只能離散變化，按上述過程求出 k_A、k_B 後，應按實際變比取值。所以，實際節點電壓在調壓前後是有變化的，應確保調壓後節電電壓變化較小，不越限。

2.3 運行條件校驗

防覆冰變壓器投入後雖然保持了母線A和B的電壓大小不變，但輸電線路首末端的電壓都減小了，而且由於線損的增加和防覆冰變壓器的損耗，通過線路傳輸的功率會增加，因此要對輸電線路傳輸功率的穩定性進行校驗。傳輸功率極限值為：

$$P_{\max} = \frac{V'_A V'_B}{X_L} \tag{8}$$

要求線路上傳輸的有功功率應小於這個極限值，可以按相應的規程規定選取一定的裕度，否則要甩掉部分負荷保證線路的穩定性。

導線載流量的計算一般考慮的環境溫度為40℃，導線表面允許溫度為 70℃[5]，而防覆冰電流要求導線表面溫度大於 0℃即可，遠低於 70℃。但是母線 A 和 B 之間的輸電線路可能經過多個氣象區，對不需要防覆冰得區域，過大得電流可能超過線路的熱穩定極限，因此需要作熱穩定校驗。

允許的最大電流（即載流量）取決於環境溫度和風速，即

$$\begin{aligned} I^2R &= 9.92\Delta t(VD)^{0.485} + \\ &\pi\varepsilon\sigma D[(t+\Delta t)^4 - t^4] - \alpha I_s D \end{aligned} \tag{9}$$

其中 Δt 為導線載流時的溫升，K；V 為風速，m/s；D 為導線外徑，m；t 為環境溫度，K；ε 為導線表面的輻射散熱係數，與導線的新舊程度有關；σ 為 Stefan-Boltzmann 常數，5.67×10^{-8} W/m2；α 為導線吸熱係數，與導線的新舊程度有關；I_s 為日照強度，W/m2；R 為導線電阻。

3 防覆冰臨界電流的確定

臨界電流的確定，常用的方法有建立熱平衡方程來計算[6][7]，通過實際資料總結出經驗公式來求取[8]等。本文採用熱平衡方程來求解。

該方法是根據導線熱功率平衡原理求得臨界電流。引起導線發熱的功率有：電流流過導線時產生的熱功率，即 I_L^2R；日光對導線的日照功率，但是由於夜間更容易引起導線覆冰，故從最不利因素考慮，這一部分不考慮。導線散熱功率有：輻射散熱功率和對流散熱功率。如果導線溫度穩定在 0℃以上時，發熱功率等於散熱功率，導線就不會覆冰。因此導線溫度穩定在 0℃時對應的線路電流為臨界電流，即

$$I_{LJ}^2 R = W_R + W_F \tag{10}$$

其中 R 為導線溫度 0℃時，單位長度的交流電阻，$\Omega/_m$，近似用 20℃的直流電阻代替；W_R 為單位長度導線的輻射散熱功率，$W/_m$；WF 為單位長度導線的對流散熱功率，$W/_m$。

$$W_R = \pi\varepsilon\sigma D[273.2^4 - t^4] \tag{11}$$

$$W_F = 0.57\pi\lambda(273.2 - t)R_e^{0.485} \tag{12}$$

式中 λ 為導線表面空氣層的傳熱係數，與環境溫度有關；R_e 為雷諾數，與環境溫度、風速和導線外徑有關。

參考文獻[6]在熱功率平衡方程的基礎上，考慮了導線表面因水分蒸發而產生的潛熱損失和過冷卻液滴被加熱到表面溫度所產生的顯熱損失的影響，得出臨界電流計算公式為：

$$\begin{aligned} I_{LJ}^2 = \frac{D}{R}[&(273.2 - t)(\pi h + \pi\sigma\varepsilon t^3 \\ &+ 2EVwC_w) + 2EVW_e L_v] \end{aligned} \tag{13}$$

其中 V 為風速；h 為對流換熱係數，與環境溫度、

雷諾數和導線外徑有關；E 為液滴總體收集係數，與風速、導線外徑和液滴直徑有關；C_w為水的比定壓熱容，可取 4.18kj/kg.K；L_v 為水的汽化潛熱，可取 2260kj/kg；W_e為導線表面蒸發的液體水分，為：

$$W_E = 0.622\pi h \frac{P_{273.2} - P_t}{2EVPC_a} \quad \textbf{(14)}$$

其中 P 為氣壓；P_t為濕空氣溫度 t 時的飽和蒸汽壓，可由 Goff-Gratch 公式求得；C_a為空氣的比定壓熱容，可取 1.006kj/kg.K。

臨界電流值都主要取決於外部氣象條件和導線本身的特性參數。而導線型號一般不會改變，所以只要知道覆冰時導線所處的氣象條件，即可確定臨界電流值。圖 3 為導線 LGJ-120/25、LGJ-210/35、LGJ-300/25 和 LGJ-400/35 在環境溫度為 268.2K（-5℃）時的臨界電流隨風速變化情況。

上述四種導線在風速為 5m/s 時的臨界電流隨環境溫度變化的情況如圖 4 所示。

要能求出臨界電流，應知道輸電線路所在區域的氣象條件（氣溫和風速），目前中國部分輸電線路上安裝有冰風觀測系統，可以傳回這些資訊，甚至能傳回導線覆冰狀況的圖片。通過即時獲取這些資料，計算出臨界電流，控制變壓器的分接開關，就可以實現防止導線覆冰的目的。

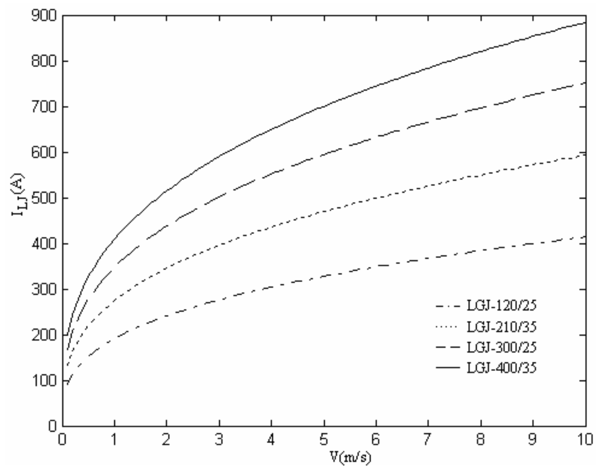

圖 3. 臨界電流與風速的關係圖

Figure 3. The relation between critical-currents and wind-speeds

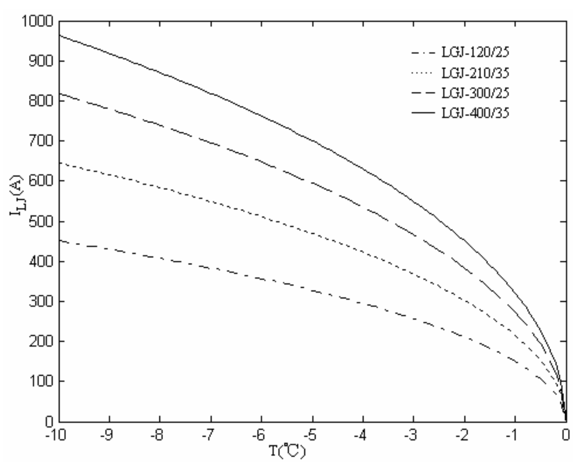

圖 4. 臨界電流與環境溫度的關係圖

Figure 4. The relation between critical-currents and environment-temperature

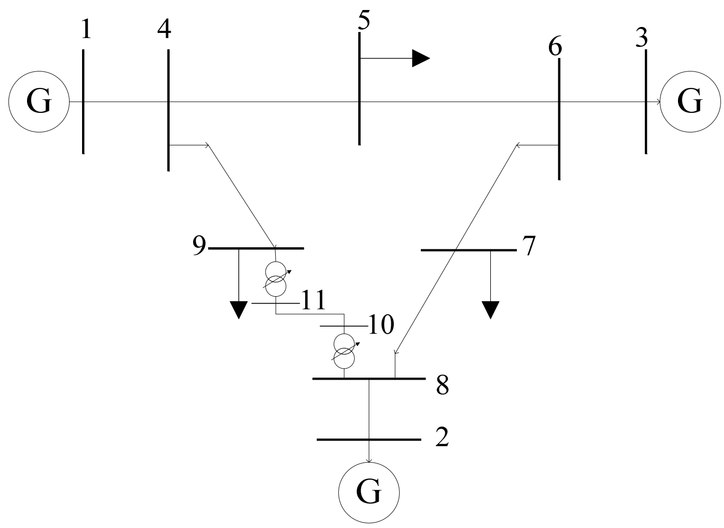

圖 5. 仿真系統電路圖

Figure 5. Circuit of simulating system

4 仿 真

為了驗證上述結論的正確性，採用 IEEE9 節點的模型來進行仿真，如圖 5 所示。設在惡劣的氣象條件下，編號為 8 和 9 的母線之間的線路需要增加電流防覆冰，線路基準容量為 100MVA，基準電壓為 230kV，導線型號為 LGJ-240/30。防覆冰變壓器沒有投入之前，經潮流計算可知，母線 8 和 9 的電壓分別為 $0.996\angle 3.8^0$ 、$0.958\angle -4.35^0$，線路流過的潮流為 $84.04 + j14.28MVA$，線路上流過的電流為 381.6A。

如果冰風觀測系統傳回的氣象條件為環境溫度 -5℃，風速 5m/s，那麼按公式（13）可計算出防覆冰臨界電流為 514A。防覆冰電流遠大於線路運行電流，這麼大的電流通過調節電網的潮流分佈是很難實現的。現採用調線路兩側的防覆冰變壓器來實現線路電流增大到臨界電流之上。

按公式（1）~（7），並設變壓器相鄰分接開關之間繞組對應電壓為 5%U_N，可求出 k_8、k_9 分別為 1.3 和 1.65，導線電流為 524.45A。導線的線損由調壓前的 $2.47 + j12.4MVA$ 變成了 $4.66 + j23.43MVA$。調壓前後各個節點的電壓變化情況如表 1 所示，表中節點 1 ~9 的電壓都在沒有越限。表 2 列出的是調壓前後發電機發的功率變化情況，因線損而增加的有功全部由與母線 1 相連的發電機承擔；而 3 台發電機發出的無功都有較大的增加。由於防覆冰線路的無功損耗也有較大增加，所以如果母線 8 處能投入無功補償設備，可大幅減少發電機的無功輸出。

按公式(8)作線路傳輸功率極限校驗，有

$$P_{\max} = \frac{V_A' V_B'}{X_L} S_{base} = \frac{0.74 \times 0.602}{0.161} \times 100$$
$$= 276.7MW$$

表 1 調壓前後節點電壓變化表（p.u.）

Table 1. The changes of node voltage before and after regulator (p.u.)

節點編號	調壓前電壓	調壓後電壓
1	1.000	1.000
2	1.000	1.000
3	1.000	1.000
4	0.987	0.994
5	0.975	0.977
6	1.003	0.998
7	0.986	0.967
8	0.996	0.97
9	0.958	0.983
10		0.74
11		0.602

表 2 調壓前後發電機功率變化表（MVA）

Table 2. The changes of generators power before and after regulator (MVA)

相連節點	調壓前	調壓後
1	71.95+j24.07	75.37+j11.37
2	163.00+j14.46	163.00+j56.58
3	85.00-j3.65	85.00+j5.55

而線路傳輸的有功功率為 69.6MW，小於傳輸極限，所以線路是穩定的。

如果採用有載調壓方式，則兩側變壓器相互配合，輪流進行有載調壓。由於每次調壓繞組數為 5%的額定繞組，對負載的影響很小。調壓過程中，母線 10 和 11 的電壓逐漸減小，而線路電流逐漸增加，其餘各母線電壓變化很小，負載的電流電壓變化也很小，因此調壓過程對用戶的影響小。

5 結 論

本文提出了輸電線路降壓運行防覆冰的控制策略，通過安裝在輸電線路兩端的防覆冰變壓器調壓，增加線路電流，從而使線路發熱增加，防止線路覆冰，保證輸電線路的安全運行。採用這種預防性措施，使輸電線路在惡劣的氣象條件下能夠正常工作。防覆冰變壓器如採用有載調壓，可實現帶負荷調壓，對用戶不產生影響。如果能與無功補償設備配合，將對電網的影響更小，調壓效果更好。

致謝

本文的研究成果在中國國家電網公司資助下取得。

REFERENCES

[1] LI Zai-hua, BAI Xiao-min, and ZHOU Zi-guan, “Prevention and treatment methods of ice coating in power networks and its recent study,” Power System Technology, China, Vol. 32, pp. 7-13, April 2008.

[2] CHANG Hao, SHI Yan, and YIN Wei-yang, “Ice-melting technologies for HVAC and HVDC transmission line,” Power System Technology, China, Vol. 32, pp. 1-6, May 2008.

[3] FARZENEHM, “Ice accretion on high-voltage conductors and insulators and related phenomena,” Philosophical Transactions of the Royal Society, Vol. 10, pp. 2971-3005, 2000.

[4] YAO Yu-bin, WU Zhi-liang, and WANG Dan, “Study on transformer representation in power system,” Relay, China, Vol. 35, pp. 16-20, 2007.

[5] HAN Fang, XU Qing-song, and HOU Wei, “Application of overhead transmission line dynamic ampacity calculation method,” Electric Power Construction, China, Vol. 29, pp. 39-43, January, 2008.

[6] LIU He-yun, ZHOU Di, and FU Jun-pin, “Heat transfer investigation on critical current to prevent wires from icing,” Electric Power, China, Vol. 34, pp. 42-44, April 2001.

[7] Maurice Huneault, Christian Langheit, and Josee Caron, “Combined models for glaze ice accretion and de-icing of current-carrying electrical conductors,” Transactions on Power Delivery, Vol. 20, No. 2, pp. 1611-1616, 2005.

[8] Hyde M. Merrill and James W. Feltes, “Transmission icing: A physical risk with a physical hedge,” IEEE PES General Meeting, Montreal, pp. 1-7, June 2006.

Energy and Power Engineering, 2009, 07-16
doi:10.4236/epe.2009.11002 Published Online August 2009 (http://www.scirp.org/journal/epe)

A Novel Real-Time Fault Diagnostic System for Steam Turbine Generator Set by Using Strata Hierarchical Artificial Neural Network

Changfeng YAN[1,2], Hao ZHANG[1], Lixiao WU[2]
[1]*CIMS Research Center, Tongji University, Shanghai, China*
[2]*School of mechanical & Electronical Engineering, Lanzhou University of Technology, Lanzhou, China*
Email: {changf_yan, lixiao_wu}@163.com; hzhangk@yahoo.com

Abstract: The real-time fault diagnosis system is very great important for steam turbine generator set due to a serious fault results in a reduced amount of electricity supply in power plant. A novel real-time fault diagnosis system is proposed by using strata hierarchical fuzzy CMAC neural network. A framework of the fault diagnosis system is described. Hierarchical fault diagnostic structure is discussed in detail. The model of a novel fault diagnosis system by using fuzzy CMAC are built and analyzed. A case of the diagnosis is simulated. The results show that the real-time fault diagnostic system is of high accuracy, quick convergence, and high noise rejection. It is also found that this model is feasible in real-time fault diagnosis.

Keywords: real-time, fault diagnosis, strata hierarchical artificial neural network, fuzzy CMAC

1 Introduction

Steam turbine generator set is a key device in power plant. The real-time fault diagnosis system is very great important for steam turbine generator set due to a serious fault results in a reduced amount of electricity supply in power plant. It can detect the incipient failure as early as possible, determine the location of the fault and identify size and nature of the faults according to the abnormal conditions appearing in the diagnosis process.

Presently, one of the widely used and effective methods for fault detection and diagnosis of rotating machines is vibration analysis. The subject of vibration generally deals with methods to determine the vibration characteristics of a system, its vibratory response to a given excitation and the means to reduce the vibration [1]. Attempts have been made towards fault diagnosis, through four steps such as vibration measurement, signal processing, feature extraction and fault identification [2].

Many different diagnosis methods have been successfully applied for turbine generator set and other rotating machines in real-time or off-line. A prototype expert system has been developed that provides decision support to condition monitoring experts who monitor British Energy turbine generators [3]. The expert system automatically interprets data from strategically positioned sensors and transducers on the turbine generator by applying expert knowledge in the form of heuristic rules. An expert system for the turbine generator diagnosis was modeled to help a plant operator interpret vibration evolution to diagnose developing faults and to recognize the observed situation among a hierarchy of typical situations in dealing with complex problems [4].

A real-time intelligent multiple fault diagnostic system for manufacturing systems is proposed by Bae et al. [5]. The expert systems and neural networks to gas turbine prognostics and diagnostics are reviewed in reference [6]. It presents recent developments in technology and strategies in engine condition monitoring including: application of statistical analysis and artificial neural network filters to improve data quality; neural networks for trend change detection, and classification to diagnose performance change; expert systems to diagnose, provide alerts and to rank maintenance action recommendations.

The application of neural networks and fuzzy logic to the diagnosis of 1x faults in rotating machinery is investigated by using the learning-vector-quantization (LVQ) neural network [7]. Yan and Gao presents a signal decomposition and feature extraction technique for the health diagnosis of rolling bearing, based on the empirical mode decomposition [8].

An on-line condition monitoring and diagnosis system for feed rolls was developed by Jeng and Wei [9]. This system measures the bearing vibration signals on-line and judges the feed roll condition automatically according to the diagnosis rules stored in the computer. Chen et al. proposed the detecting and predicting early faults of the complex rotating machinery model based on the cyclostationary time series [10]. Wang and Yang applied parallel processing and distributed artificial intelligence at four different levels in the fault diagnosis process for the turbine generator of a 300MW fossil power plant [11].

However, the real-time fault diagnosis is required to monitor the abnormal change and to judge the fault reason as soon as possible. This paper proposes a real-time intelligent fault diagnosis system by using strata hierarchical artificial neural. In this diagnostic system, it can real-time diagnose faults according to vibration feature on conditions of steam turbine generator sets. For the mechanical system, the fault characteristics can be classified systematically to be a hierarchical structure according to different levels. An independent engine module which manages the feature variables input the diagnostic modules in terms of result of the threshold value trigger in the higher level, and outputs the fault to operator by collecting the diagnostic result of the diagnostic module finally in our model. Because combined the advantage of interpreting the imprecise of fuzzy set with fast training, guaranteed converge and partial generalization of CMAC, this model can meet online fault diagnosis.

2 Framework of Fault Diagnosis System

In the viewpoint of system, every system is made up of components, and any components can be broken down into smaller components [12]. Therefore the system can be divided into system, subsystem and component level. The complex hierarchical diagnostic system generates a relatively abstract ordering of steps to realize the goal of diagnostic and then each abstract step is realized with simpler diagnostic plans. A hierarchical scheme looks somewhat like a tree structure, where the steps at the higher level of the tree represent more abstract and complex tasks.

Steam turbine generator sets is made up of mechanical, electrical, hydraulic, heating and related accessorial units, even hundreds of components in the mechanical unit. The mechanical fault includes different level fault such as unbalance, oil whip, pneumatic torque, misalignment, radial rub, twin looseness, bad thrust bearing, gasp vibration, unequal stiffness bear, and rotor crack and etc. Because the vibration is a good image of the machine health for rotating mechanical unit, it is very important to monitor the vibration parameters along the shaft and/or the bear such as amplitude, frequency and orbit online. In order to identify the fault correctly and quickly, it is necessary to monitor vibration signals together with other running parameters such as load, bearing oil temperature, hydrogen pressure, vacuum measure, etc. These symptoms are grouped into 10 categories [13]. The diagnosis of a developing fault is necessary to predict further evolution and to anticipate it by taking appropriate measures. Therefore, this paper focuses on the mechanical faults which are relative to the vibration to express our idea of the model in order to simplify the problem. The feature signals which are related to the vibration are regarded as the symptom to detect the cause of fault. Both time domain and frequency domain approaches could also be used to analyze vibration signals.

The flowchart of the real-time fault diagnosis system is shown as Figure 1. The condition monitor and control system is developed to capture vibration measurements and operational parameters from strategically positioned

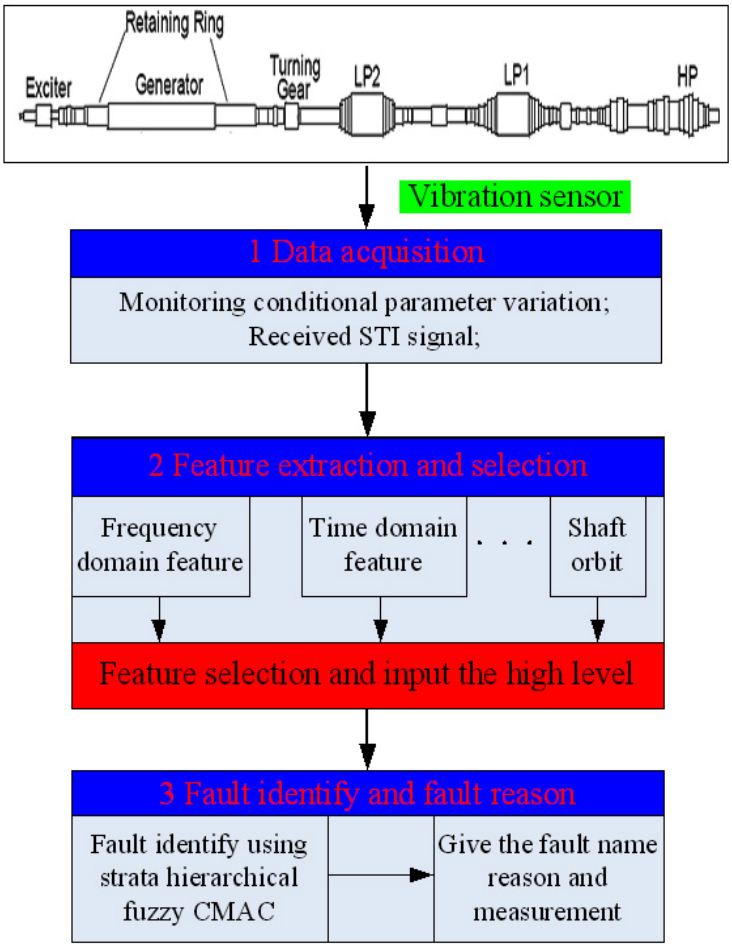

Figure 1. Flowchart of fault diagnosis system

sensors and transducers on the turbine generator online. The system is configured to trigger an alarm when each predefined limit is breached. The limits are set on each channel to monitor the overall vibration magnitude, first-order and/or second-order vibration magnitude, phase and sub-harmonic frequency levels. When the signal data is beyond the predefined threshold, the diagnostic system is triggered immediately. Fault feature are extracted on the basis of the measurements provided by the turbine supervisory instruments (TSI) signals. Then the actual diagnostic task is to map the points in the symptoms space into the set of considered faults by the fuzzy CMAC diagnostic system. The possible fault names in steam turbine generator sets will be given by system identifying. Meanwhile the reason of the fault and preventive or maintenance measurements will be listed. The operators can deal with the fault as soon as possible according these advices. Of course, if the actual fault need to somewhat identify further, the advice would be given based on the system analysis.

3 Hierarchical Fault Diagnostic Structure

The human body is organized in a hierarchical structure as shown in Figure 2. In this structure, the upper levels efficiently control the lower levels. All information of a human body is delivered to the brain by use of neurons. The brain judges this information based on person's experience, and gives instruction to the each part of the body by the distributed neural system.

The hierarchical fault diagnostic structure can be de

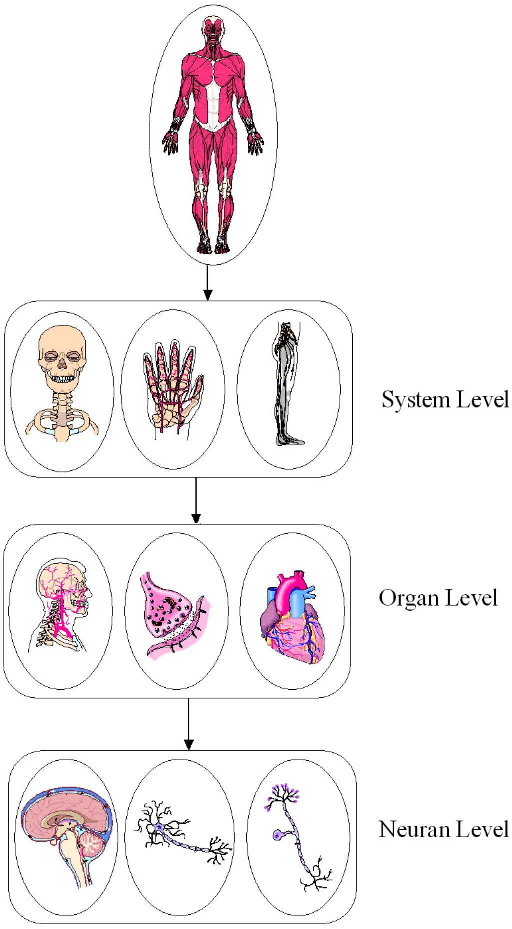

Figure 2. Hierarchical structure in a human body

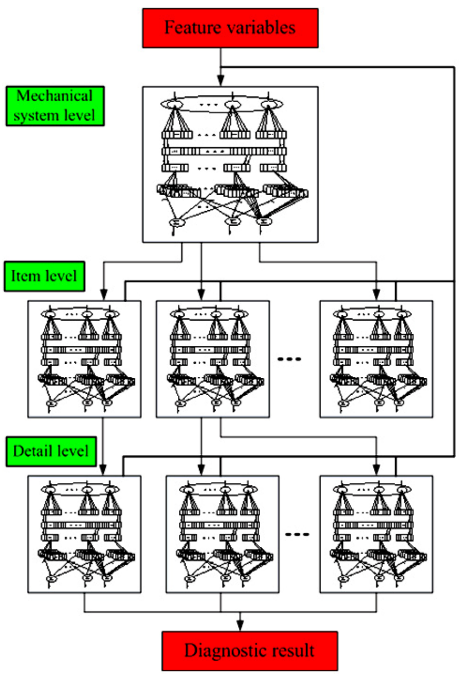

Figure 3. Hierarchical fault diagnostic structure

scribed as shown in Figure 3. Feature variables are extracted from vibration signals and other running parameters firstly. The different features are needed to input for the different level and the different components. The fault diagnostic algorithms in three levels are all the fuzzy CMAC in our model.

An independent engine module in thicker line which manages the feature variables input the diagnostic modules in terms of result of the threshold value trigger in the higher level, and outputs the fault to operator by collecting the diagnostic result of the diagnostic module finally in our model. The diagnostic cells that actually fire as a result of various levels of the feature depend on the threshold levels of the diagnostic cells. Only diagnostic cells with enough excitatory inputs to exceed threshold will fire. This threshold value for diagnostic cells is regulated by the possibility of decision.

The independent engine module simulates the neural anatomy structure in the human body. The brain collects the information by the nervous process and gives instructions by nerve fibers to the every part of body based on the diagnostic results.

The upper level is the mechanical fault diagnosis units, which can identify the fault which item belongs to in primarily. The next level is the item fault level which can be considered several subsystems, for example, the mechanical fault including unbalance, oil whip, pneumatic torque, misalignment, radial rub, twin looseness, bad thrust bearing, gasp vibration, unequal stiffness bear, rotor crack fault and so on. The diagnosis of a developing fault is necessary to predict further evolution and anticipate it by taking appropriate measures. This paper focuses on the mechanical faults which are relative to the vibration to express our idea of model in order to simplify the problem. In fact, people who work with steam turbine generator sets usually perform vibration diagnosis using their field experience and textbook knowledge. The other diagnostic unit will be investigated further in the future.

The lower level is the detail fault in theory. For instance, it can judge whether the rotor crack is damage, high-cycle fatigue, low-cycle fatigue, creep, crack and erosion or not. In this hierarchical system, it can also classified by more levels to identify the fault in detail further. However it is not always good use for this kind of the diagnostic system. The decision of how to partition the diagnosis system depends on how complex is each level, and how many and what types of the feature variables are available at each level, and what methods are to identify the fault in the steam turbine generator sets. When we care for the more minute fault, the more monitoring device must be used, the more signal should be processed, and also the more experiment should be taken to obtain the feature of the fault. Despite of availability of these measurements, such tasks are left to the diagnostic system and the operator, and thus will result in overload in real time especially, even lead to erroneous decisions in the serious cases.

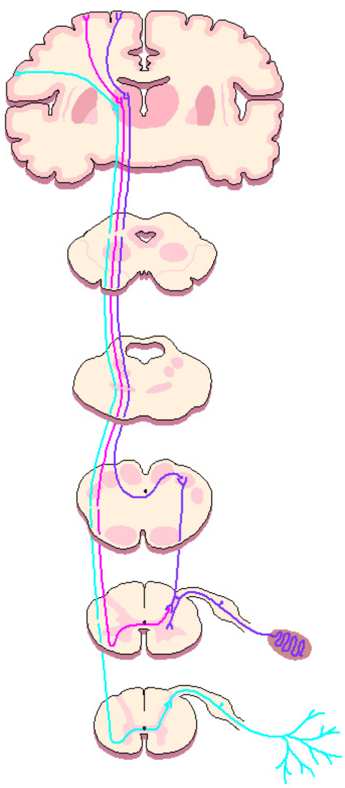

Figure 4. Neural anatomy structure of engine module

In order to identify the fault further, the trend features such as relationships between amplitude of the vibration, the pressure and the load are also required to be given.

4 Mechanism of Fuzzy CMAC Diagnosis

4.1 Introduction of Fuzzy CMAC

Albus presented the CMAC neural network and applied it to the robotic manipulator control in 1975 [14]. The CMAC is a kind of memory, or table kook-up mechanism. From a purely structural standpoint, the CMAC neural network simulates the human being's cerebrum which function visual cortex and need process considerable feature-detection to generate the appropriate command signals [15]. The CMAC neural network is shown as Figure 5 with anatomy.

However there are some disadvantages for the standard CMAC. The large generalization parameter C will increase the memory requirement seriously and decrease the local generalization ability of CMAC, eventually more expensive calculating time [16][17]. When the small memory applied for online diagnosis, the insufficient memory will prevent excessive noise caused by overlap due to hash coding. Besides, if the training patterns are not enough to update all weights, there would be some weights untrained. This will lead to severe decrease the approximation performance in some certain regions [18].

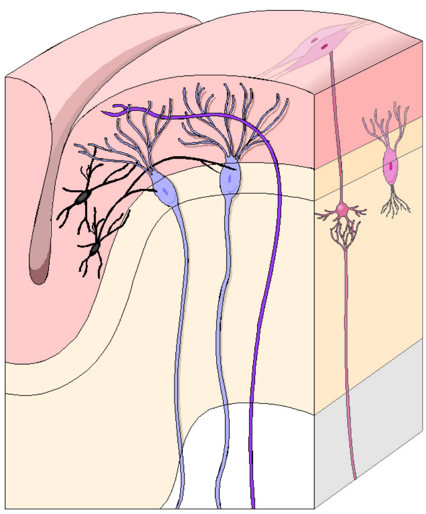

Figure 5. Anatomy structure of CMAC

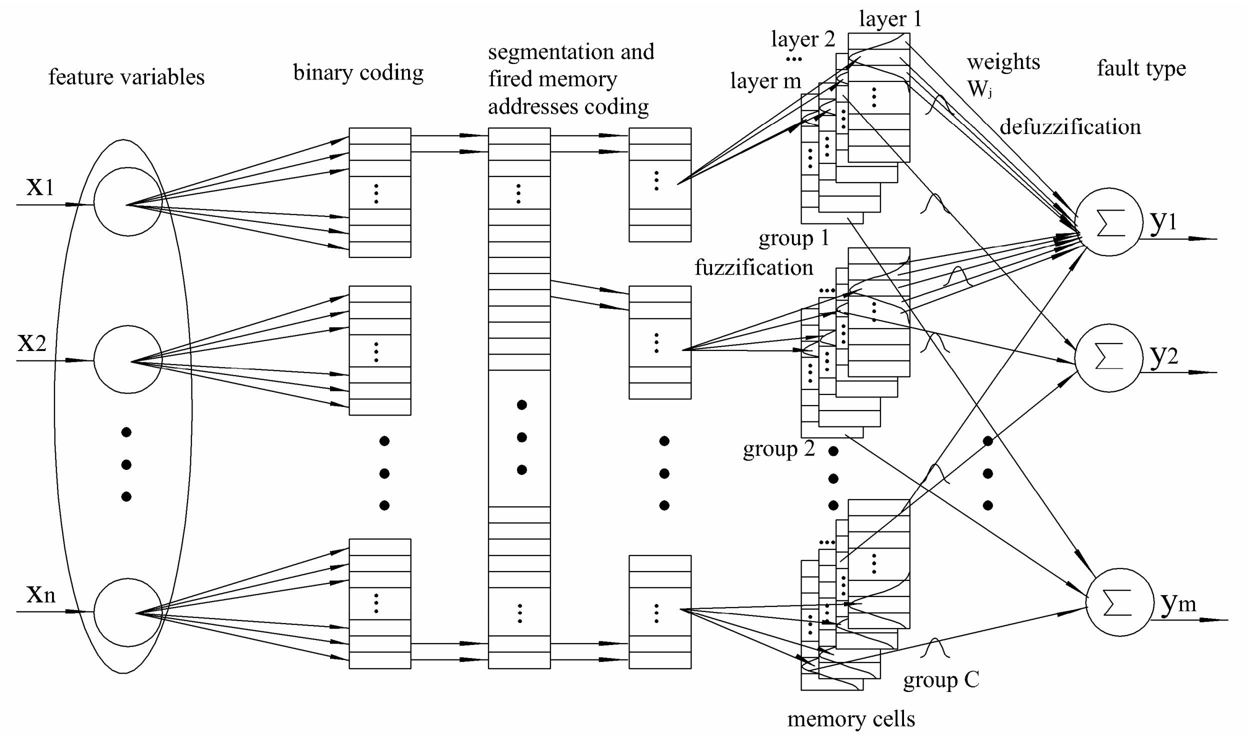

Figure 6. Scheme of the fuzzy CMAC for diagnosis

In order to overcome these deficiencies, Fuzzy CMAC is hybrid system that possesses the merits of both the neural network and the fuzzy rule-based system. In order to meet the real-time and precision demand for the fault diagnosis system in steam turbine generator sets, the detail architecture of a novel fuzzy CMAC shown as Figure 6 is proposed in the paper.

The fuzzy CMAC network can be applied to approximate function $y = f(x)$, in which feature variable $x \in X \subseteq R^n$, and fault type $y \in Y \subseteq R^m$, can be realized by three sequential mapping as following.

$$\Theta : X \to S, \quad (1)$$

$$\Phi : S \to A, \quad (2)$$

$$\Psi : A \to Y \quad (3)$$

In the first mapping Θ, the feature variables will be quantized as binary coding. In the second mapping Φ, CMAC uses a fuzzy distributed storage system whereby the numerical contents of each address are distributed over a number of physical memory locations. The contents of these physical memory locations are referred to as weights. Each membership function (MF) in the contents of memory location is represented by a Gaussian distribution. In the third mapping Ψ, the fault types will be realized by the membership function time weight sum of contents of an address.

4.2 Step of Diagnosis Mode by Using Fuzzy CMAC

Step 1 Input feature signals

The input signals of the fuzzy CMAC in deferent level might include feature variables such as one or combination with the frequency feature, phase feature, shaft orbit feature, even trend feature and so on.

Step 2 Quantize the signals

No matter the testing or training signals, they should be mapped to quantization output firstly. For the analogue variable, the quantization output can be represented as following.

$$q_i = Q\left(x_i, x_{i\min}, x_{i\max}, q_{i\max}\right), \quad i = 1, \cdots n, \quad (4)$$

where, $x_i, x_{i\min}, x_{i\max}$ is the input, expected maximum input, expected minimum input respectively. $q_{i\max}$ is the quantization parameter.

Step 3 Segmentation, fired memory addresses coding

The quantization of the signal $q_i(x)$ will be coded according to binary form. Then we concatenate the quantization signal as a binary string. The combined binary input maps a set of memory location from a large pool of memory locations.

In human cerebellar cortex, the mossy rosettes from a single mossy fiber are widely distributed over several folia with Gaussian distribution [15]. In order to simulate the mechanism of the human cerebellar cortex, several memory addresses near the main memory address will be activated according to the Gaussian distribution.

$$\mu_{ij} w_{ij} = ad(j)_i \qquad j = n-p, n-p+1, \cdots, n+p \,, \tag{5}$$

where $ad(x)$ is the memory address in the j-th column of i-th group. It can be pointed to addresses in the m layer in the same time.

$$\mu_{ij} = \exp\left[-\frac{1}{2}\left(\frac{x_{ij}-c}{\sigma}\right)^2\right]; \qquad j = 1, 2, \cdots k \,, \tag{6}$$

where c and σ represent respectively the center and the width of the j-th column of i-th group for input x, k is the total number of address in each group.

In this structure, the inner layer (Fuzzy CMAC memories) can be partially activated, allowing the network output to be smooth. Also the problem that some weights do not update because of lack of enough training would be overcome.

Step 4 Calculate output and learning rule

Fuzzy CMAC learns correct output fault by modifying the contents weight of the selected memory locations. The actual output of the fuzzy CMAC after mapped can be described as

$$y_i = \sum_{j=1}^{C} \mu_{ij} w_{ij} a_{ij}(x) \qquad i = 1, 2, \cdots, m \quad , \tag{7}$$

where, w_{ij} is the weight of *j-th* storage hypercube. If $a_{ij}(x)$ is addressed, then w_{ij} is 1, else is 0. There are only C storage hypercube has an affection to output

Step 5 Learning algorithm

The weight adjusting can be thought as that the teaching and supervised leaning algorithm is described as

$$w_j^k = w_j^{k-1} + \eta(k)(y_d - \sum_{j=1}^{N_l} w_j^{k-1} \mu_{ij} \alpha_j) / \sum_{j=1}^{N_l} \mu_{ij} \quad , \tag{8}$$

where $\eta(k)$ is training gain.

In every step of iteration, only those network weights that participate in output calculation are adjusted. That is, the weights are determined by a training phase, during which these values are adjusted to minimize the difference between the fuzzy CMAC output and its expected output. So, for Hebbian learning, the cost function

$$\varphi_i(w) = \sum_{i=1}^{m} ((y_d - \sum_{j=1}^{N_l} w_j^{k-1} \mu_{ij} \alpha_j) / \sum_{j=1}^{N_l} \mu_{ij})^2 \tag{9}$$

is minimized.

When $\varphi_i(w) < \varepsilon$, (ε is a small positive constant and an acceptable error), the training process will stop. Because the fuzzy CMAC tends to generalize over small neighborhoods in input-space and can approximate a desired function after a relatively few data points are stored [17], it does converge rather rapidly compared to the other artificial neural networks.

Step 6 Test the fuzzy CMAC

Load the diagnosis data which did not used to train the fuzzy CMAC mode, and test whether diagnostic result using the fuzzy CMAC mode is correct or not. If the tolerance is satisfied with the requirement of diagnosis, then save the mode to the system, else update the weight value of the memory, until it meet the demand of the tolerance.

5 Case Study

In order to validate our model, the training samples are used to test. In fact, one type of fault is often combined with the other fault no matter which is in incipient or happened, they will interact with each other. Even we can not identify the major fault immediately. On the other hand, it is very helpful for operators to find the fault as early as possible, because the incipient fault or the earlier fault will cause the lower loss than that fault which might lead to the machine out of work. The oil membrane oscillation, unbalance and misalignment somewhat belong to this condition.

Training sample is combined with oil membrane oscillation, unbalance and misalignment. The input variables are <0.4f, 0.4-0.5f, 1f, 2f, 3f and >3f, which is shown in Table 1. That is the typical vibration frequency feature, and the other features are neglected here. The $q_{i\max}$ is 1024 and C is specified 10. The weights in these memory cell are trained according to the equation 8 until the tolerance meet the requirement. The results of the training are shown in the Figures 7, 8 and 9. In these figures, the desired value is represented by the circle, and the training value is represented by the star. It can be shown that the result of the fuzzy CMAC output is very close to the original value. The error will decrease quite quickly. Therefore fuzzy CMAC neural network is of high accuracy, quick convergence, and high noise rejection for fault diagnosis in steam turbine generator sets.

Table 1. The diagnosis input and output training sample

	input feature variable						output fault type		
	<0.4f	0.4-0.5f	1f	2f	3f	>3f	Oil membrane oscillation	unbalance	Mis-alignment
1	4.7244	67.6934	17.3260	2.3833	3.1486	4.7244	0.7368	0.2677	0.3747
2	6.2277	69.5962	15.4977	3.8887	1.5498	3.2399	0.7703	0.2204	0.3569
3	4.8642	74.1736	16.9309	1.6125	0.8062	1.6125	0.8574	0.2450	0.3603
4	7.9088	67.2246	17.4139	4.9178	1.7279	0.8070	0.7183	0.2559	0.3814
5	7.9706	60.8730	20.2888	4.3476	2.8971	3.6230	0.6835	0.3021	0.4087
6	10	80	10	0	0	0	1.0	0	0
7	1.5804	4.8857	77.5842	9.4822	3.3053	3.1622	0.2253	0.7138	0.2545
8	3.3843	1.7039	84.7415	6.7718	0.8590	2.5394	0.2763	0.7568	0.1829
9	0.8574	4.2852	76.8717	10.2789	5.9905	1.7163	0.1820	0.6937	0.2715
10	0.8178	2.5151	79.9901	9.1779	4.9994	2.4997	0.2446	0.7186	0.2472
11	1.8393	2.0000	84.2180	7.3233	0.9509	3.6684	0.2359	0.7560	0.2337
12	0	0	90	5	5	0	0	1.0	0
13	2.2962	8.1200	76.6193	5.2533	0.3579	7.3532	0.2553	0.6915	0.2216
14	2.1410	1.4339	29.2606	31.4016	24.9786	10.7842	0.0571	0.2471	0.7608
15	0.6969	1.7148	39.7991	28.9515	21.7086	7.1292	0.1004	0.3024	0.6222
16	0.6637	2.0837	27.7821	33.3385	22.2295	13.9026	0.0779	0.2347	0.7759
17	1.3735	0.6950	30.8176	28.0783	19.1754	19.8602	0.1435	0.2401	0.6437
18	0	0	40	50	10	0	0	0	1.0
19	0.5919	1.1859	28.0984	28.0984	22.1580	19.8673	0.1194	0.2698	0.6678

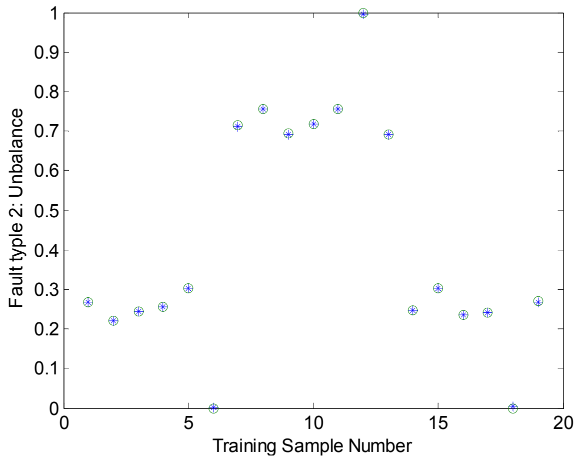

Figure 7. Training result of the fault type 1

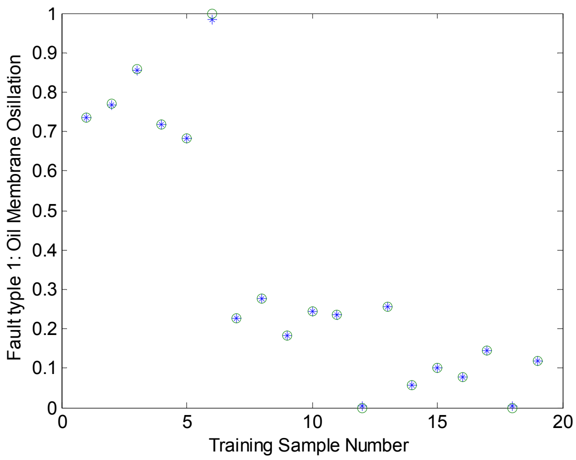

Figure 8. Training result of the fault type 2

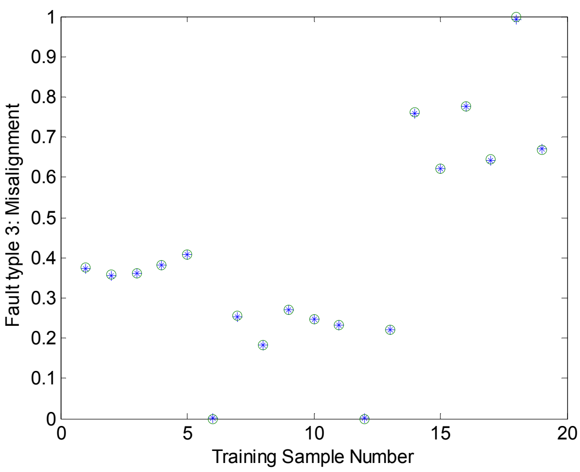

Figure 9. Training result of the fault type 3

In order to judge whether the fuzzy CMAC model can be used to diagnose or not, the trained model should be tested by the experimental data. However, no laboratory setup can accurately simulate the faulty behavior of the turbine generator, since it is too expensive to do for the researcher or the designer of the company. The samples in Reference [19] is tested in our model, the amplitude of frequency is 4.42, 6.6, 224.79, 103.31, 29.01, 46.78 respectively in monitoring condition. Because the other states are not mentioned in it, they are neglected to test. Normalizing them into 1.0653, 1.5907, 54.178, 24.899, 6.9919, and 11.275 and inputting to the trained fuzzy CMAC model, three fault output are 0.2130, 0.5824, and 0.3761 respectively. It is shown that the major fault is the unbalance and the misalignment is in the early stage. This result fits the conclusion of bearing house looseness, unbalance and the misalignment in Reference [19].

6 Discussion

In the viewpoint of practical work, the parameters of fuzzy CMAC could affect the accuracy of fault detection. When the generalization parameter C and address number S are changed, the result of the fuzzy CMAC trained would also be changed. The conclusion can be made easily, which the capability of fuzzy CMAC module is strong as C and S are big. It means that the CMAC can remember much knowledge while the address number is large. When the generalization is big, the output of the fault is smooth. In another words, we can get any value of the fault when we chose the parameters big enough. However it is impossible for the fault diagnosis in terms of limited experimental data. And it is not suitable for steam turbine generator set to diagnose the fault.

It is observed that the preliminary data is very important for the same fault and the training output nearly fits to the original data very well. Therefore we should use the high quality data to train the fuzzy CMAC neural network model. In order to apply to the fault diagnosis of steam turbine generator sets, for the practical purpose, experimental data needs to obtain. Furthermore, no laboratory setup exists that can accurately simulate the faulty behavior of the turbine generator. Therefore, there is a little training data available. However the capability of fault diagnosis will increase with the increase of the causal fault and behavioral knowledge of long-term vibration measurements. Although the fuzzy CMAC diagnostic module might not be very correct in the early stage, it would become more and more precisely to response the fault with the training proceeding or the learning in the application.

7 Conclusions

In this paper, a novel real-time fault diagnostic system is presented. When the signal is triggered, The TSI signals are collected and feature extraction is applied. Then the fault diagnosis system by using strata hierarchical fuzzy CMAC is used to identify the fault or failure in deferent level in the steam turbine generator set. This model is verified by a case of the diagnosis including three faults. It is found that this model is feasible in real-time fault diagnostic system. The results show that this model is of high accuracy, quick convergence, and high noise rejection for the real-time fault diagnosis.

Acknowledgments

This work is supported by Program of Shanghai Subject Chief Scientist (No. 09XD1401900) and Natural Science Foundation of Shanghai (No. 09ZR1413300).

REFERENCES

[1] K. N. Gupta, “Vibration—A tool for machine diagnostics and condition monitoring,” Sadhana, Vol. 22, No. 3, pp. 393-410, 1997.

[2] M. S. Patil, Jose Mathew, and P. K. Rajendra Kumar, “Bearing signature analysis as a medium for fault detection: A review,” Journal of Tribology, Vol. 130, pp. 1-7, 2008.

[3] Martin Todd, Stephen D. J. McArthur, J. R. McDonald, and Sally J. Shaw, “A semiautomatic approach to deriving turbine generator diagnostic knowledge,” IEEE Transactions on Systems, Man, and Cybernetics—Part C: Applications and Reviews, Vol. 37, No. 5, pp. 979-992, 2007.

[4] Jean-Marc David and Jean-Paul Krivine, “DIVA: Recognition of typical situations for turbine generator diagnosis,” Journal of Intelligent and Robotic Systems, Vol. 1, pp. 287-298, 1988.

[5] Yong-Hwan Bae, Seok-Hee Lee, Ho-Chan Kim, Byung-Ryong Lee, Jaejin Jang, and Jay Lee, “A real-time intelligent multiple fault diagnostic system,” International Journal of Advanced Manufacturing Technology, Vol. 29, pp. 590-597, 2006.

[6] H. R. DePold and F. D. Gass, “The application of expert systems and neural networks to gas turbine prognostics and diagnostics,” Journal of Engineering for Gas Turbines and Power, Vol. 121, pp. 607-612, 1999.

[7] A. El-Shafei, T. A. F. Hassan, A. K. Soliman, Y. Zeyada, and N. Rieger, “Neural network and fuzzy logic diagnostics of 1x faults in rotating machinery,” Journal of Engineering for Gas Turbines and Power, Vol. 129, pp. 703-710, 2007.

[8] Ruqiang Yan and Robert X. Gao, “Rotary machine health diagnosis based on empirical mode decomposition,” Journal of Vibration and Acoustics, Vol. 130, pp. 1-12, 2008.

[9] J. J. Jeng and C. Y. Wei, “An on-line condition monitoring and diagnosis system for feed rolls in the plate mill,” Journal of Manufacturing Science and Engineering, Transactions of the ASME, Vol. 124, pp. 52-57, 2002.

[10] Z. S. Chen, Y. M. Yang, Z. Hu, and G. J. Shen, “Detecting and predicting early faults of complex rotating machinery based on cyclostationary time series model,” Journal of Vibration and Acoustics, Transactions of the ASME, Vol. 128, pp. 666-671, 2006.

[11] Xue Wang and Shuzi Yang, “A parallel distributed knowledge-based system for turbine generator fault diagnosis,” Artificial Intelligence in Engineering, Vol. 10, pp. 335-341, 1996.

[12] Benjamin S. Blanchard and Wolter J. Fabrycky, “Systems engineering and analysis,” Prentice-Hall Inc., 1998.

[13] Chun Cheung Siu, Qiang Shen, and Robert Milne, “A fuzzy expert system for turbomachinery diagnosis,” Proceedings of the 1st Online Workshop on Soft Computing, pp. 7-12, 1995.

[14] James S. Albus, “A new approach to manipulator control: The cerebellar model articulation controller (CMAC),” Transaction of ASME, Journal of Dynamic Systems, Measurement, and Control, Vol. 97, pp. 220-227, 1975.

[15] James S. Albus, “A theory of cerebellar function,” Mathematical Biosciences, Vol. 10, No. 1/2, pp. 25-61, 1971.

[16] Daqi Zhu and Min. Kong, “A fuzzy CMAC neural network model based on credit assignment,” International Journal of Information Technology, Vol. 12, No. 6, pp. 1-8, 2006.

[17] James. S. Albus, “Data storage in the cerebellar model articulation controller (CMAC),” Journal of Dynamic Systems, Measurement, and Control, Transaction of ASME, Vol. 97, No. 3, pp. 228-233, 1975.

[18] Hung-Ren Lai and Ching-Chang Wong, “A fuzzy CMAC structure and learning method for function approximation,” IEEE International Fuzzy Systems Conference, Melbourne, Australia, pp. 436-439, 2001.

[19] Zhengjia He and Shusheng An, “A fuzzy identification of machinery condition,” Mechanical Engineering, Vol. 5, pp. 42-44, 1990.

Energy and Power Engineering, 2009, 17-20
doi:10.4236/epe.2009.11003 Published Online August 2009 (http://www.scirp.org/journal/epe)

Corrosion Prevention of the Generator Stator Hollow Copper Conductor and Water Quality Adjustment of Its Internal Cooling Water

Ling PAN [1], Qianqian HAN[1], Xuenong XIE[2], Xuejun XIE[1], Peng XIAO[1]
[1]*School of Power and Mechanical Engineering, Wuhan University, Wuhan* 430072*, China*
[2]*Sinohydro bureau* 8 *Co., LTD*

Abstract: On the basis of expounding the corrosion mechanism of the stator hollow copper conductor in the water-cooling generator, methods of preventing corrosion of the stator hollow copper conductor in the water-cooling generator through adjusting water quality of its cooling water have been proposed. For internal water cooling systems which are airtight, the corrosion of the hollow copper conductor can be prevented through keeping foreign oxygen and carbon dioxide from entering the system, and the amount of oxygen in the internal water can be lowered by blowing high purity nitrogen. For systems not airtight, the corrosion of the hollow copper conductor can be inhibited through lowering the amount of oxygen to some extent by sealing and increasing pH value by processing part of cooling water with bypass small flow sodium-type mix-bed.

Keywords: generator, internal cooling-water, hollow copper conductor, corrosion and protection

1 Corrosion Mechanism of the Generator Stator Hollow Copper Conductor

The corrosion mechanism of the generator stator copper conductor has been studied by large quantities of researches home and abroad. The main reactions considered to take place in the process of copper corrosion are as follows:

1) Corrosion caused by dissolved oxygen:

Anodic reactions:

$$2Cu + H_2O - 2e \rightarrow Cu_2O + 2H^+$$

$$Cu - 2e \rightarrow Cu^{2+}$$

$$Cu - e \rightarrow Cu^+$$

Cathodic reactions:

$$O_2 + 2H_2O + 4e \rightarrow 4OH^-$$

$$Cu + 2OH^- \rightarrow Cu(OH)_2$$

$$Cu(OH)_2 \rightarrow CuO + H_2O$$

Other cathodic reactions included:

$$2Cu^+ + H_2O + 2e \rightarrow Cu_2O + H_2$$

$$Cu^+ + H_2O + e \rightarrow CuO + H_2$$

$$2Cu^+ + 1/2O_2 + 2e \rightarrow Cu_2O$$

$$2Cu^+ + O_2 + 2e \rightarrow 2CuO$$

The result is the corrosion of copper and the formation of an oxidative membrane (the copper oxidative protection membrane) with double-layer structure on the surface of the copper at the meantime in normal case.

2) In acidic environment, the copper oxidative protection membrane will be dissolved. The internal cooling water which contains carbon dioxide belongs to acidic medium as the dissolved carbon dioxide can react as the following reaction.

$$CO_2 + 2H^+ = Cu^{2+} + H_2O$$

$$H_2CO_3 \rightleftharpoons H^+ + HCO_3^-$$

Furthermore, pH value will decrease under the condition of existence of carbon dioxide due to the high purity and poor buffering performance of internal cooling water.

For example, pH value of the pure water will be lower than 6.7 when there is 1mg/L dissociate carbon dioxide.

Therefore, the corrosion is accelerated by carbon dioxide, mainly through lowering pH value of internal cooling water and the following reactions which can destroy the protective membrane on the surface.

$$CuO + 2H^+ = Cu^{2+} + H_2O$$

$$Cu_2O + 2H^+ = 2Cu^+ + H_2O$$

$$Cu(OH)_2 + 2H^+ = Cu^{2+} + 2H_2O$$

2 Methods of Preventing the Corrosion of the Generator Stator Copper Conductor

At present, many scientific workers home and abroad are carrying out a lot of researches on the problem of copper conductor corrosion and protection, trying to seek for a method which is more economical, convenient, safe and reliable to prevent the corrosion of hollow copper conductor.

2.1 Lower the Amount of Dissolved Oxygen and Carbon Dioxide in the Internal Cooling Water

The corrosion rate peaks in common case when the concentration of dissolved oxygen ranges from 0.5mg/L to 2.0mg/L. The concentration of dissolved oxygen in the water contacting with air at the temperature of 25℃ is 1.4~3.2mg/L. The operational temperature of cooling water ranges from 20℃ to 85℃, and the temperature of water flowing through hollow copper conductor is usually above 40℃. The amount of oxygen decreases when the temperature increases, but the decreased extent of the amount of oxygen is not large.

For the purpose of studying the effect dissolved oxygen had on the copper corrosion, the operational environment of internal cooling water was simulated and the relationship between dissolved oxygen amount and corrosion behavior of copper at 50℃ was investigated. The result of experiment carried out to study the relationship between oxygen concentration and copper corrosion at 50℃ in simulated internal cooling water operational environment is shown in Table 1. The test was conducted using pure copper specimen as test material and deionized water as test medium at the temperature of 50±1℃ and the test time was 72h. The concentration of dissolved oxygen was controlled through blowing nitrogen into the water during the test. Pre-test pH value and conductivity is measured at 11℃ before starting to blow nitrogen. It can be learned from Table 1 that the corrosion of copper in deionized water can be inhibited effectively when the concentration of dissolved oxygen is controlled approximately at the level of 10μg/L.

Table 1. Result of test on the relationship between dissolved oxygen concentration and copper corrosion at the temperature of 50℃

	Pre-test		After test			
Dissolved Oxygen Content,μg/L	Conductivity, μs/cm	pH	Conductivity, μs/cm	pH	Cu^{2+} content, μg/L	Surface condition of test specimen
Below 5	0.64	6.2	1.85	7.15	3.9	bright
8～12	0.65	6.2	2.12	7.20	8.9	bright
40～60	0.67	6.2	2.10	7.15	45.1	light dead red
90～110	0.65	6.2	2.43	7.14	103.7	partially black
450～550	0.64	6.2	2.38	7.00	300.8	partially black
950～1050	0.65	6.2	3.05	6.90	269.2	partially black
4800～5200	0.65	6.2	2.30	6.75	190.4	mostly black
11500	0.65	6.2	1.92	6.80	182.2	dark dead red

For a 300MW water-hydrogen-hydrogen cooled unit with airtight internal water cooling systems and an internal cooling water tank whose volume is $2m^3$, the conductivity and pH value of the internal cooling water is monitored continuously at the sample flow ranges from 500 ml/min to 700ml/min. Thus, the amount of daily make-up water, which is the effluent of high-speed mixed bed, is 0.72t. The effluent water quality of high-speed mixed bed is that the conductivity is no more than 0.2μs/cm, and pH value ranges from 7.03 to 7.10, and the concentration of dissolved oxygen is 20~30μg/L, and there is no NH_4^+. As a result, the operation of internal cooling system is in good condition and the corrosion of hollow copper conductor is inhibited significantly, as the internal cooling water has conductivity no more than 0.2μs/cm, pH value ranging from 7.03~7.10, and low copper concentration which is 9.85~16.4μg/L [2].

For a 500MW supercritical pressure unit using condensate whose pH value is 8.6~8.8 approximately as make-up of the internal cooling water, due to the continuous dissolving of carbon dioxide, pH value of the internal cooling water is above 8.2 in common case, and the conductivity of 1.5~3.0μs/cm is relatively high [3]. After blowing high purity nitrogen into the internal cooling water, pH value of the internal cooling water is above 8.0, and the concentration of copper is lowered to less than 10μg/L, and the conductivity can be below 1.0μs/cm.

2.2 pH Adjustment for Preventing Corrosion of Hollow Copper Conductor

Figure 1 is the reduced potential-pH diagram of copper-water system, which is ploted taking Cu、Cu_2O、CuO and Cu_2O_3 as the balanced solid-phases and the value of balanced concentration of Cu^{2+} and other relative ions at the level of 10^{-6}mol/L (i.e.64μg/L) or $10^{-6.2}$mol/L (i.e.40μg/L) as the threshold concentration which can indicate weather the copper is corrupted or not [1][4].

It can be learned from Figure 1 that the balanced potential-pH diagram of copper-water system is divided into three parts by the isoline of solubility of 10^{-6}mol/L or $10^{-6.2}$mol/L for copper and its oxides: corrosion region, no-corrosion region and passivation region. The state of copper, in another word, which region the copper falls into, is jointly determined by the potential of copper-water system and its pH value. As the potential of hollow copper conductor in the internal cooling water system is difficult to measure, the pH interval where copper and its oxides can exist stably is 6.94 to 10.81 or 7.04 to 10.31 when 10^{-6}mol/L (i.e. 64μg/L) or $10^{-6.2}$mol/L (i.e. 40μg/L) is taken as the threshold concentration which indicates the copper is corrupted weather or not.

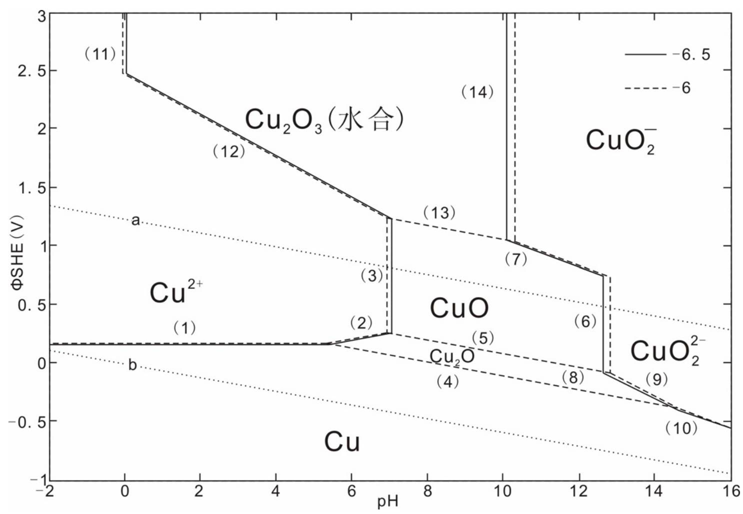

Figure 1. Potential-pH diagram for copper-water system

It can be learned through calculation that the conductivity of newly-prepared deionized water is 2.1μs/cm when its pH value is adjusted to 8.9 using analytically pure ammonia water, and is 2.48μs/cm when its pH value is adjusted to 9 using analytically pure sodium hydroxide solution. In view of the requirement of the conductivity no more than 2μs/cm in the currently standard for internal cooling water quality, pH value of internal cooling water is controlled between 7 and 8.9, and the corrosion of hollow copper conductor can be inhibited significantly. It is true in the practical internal cooling water system. Among the various methods which can be employed to increase pH value, the safest and most reliable one is processing part of cooling water with bypass small flow sodium-type mix-bed. When part of internal cooling water flows through the sodium-type small mix-bed, the cations such as the small amount of Cu^{2+} and Fe^{3+} are converted into Na^{+} and the anions are converted into OH^{-} before mixing with the rest internal cooling water which does not pass through the Sodium-type small mix-bed. Thus, it corresponds to adding approximately pure sodium hydroxide to the internal cooling water. PH value of internal cooling water can be adjusted to be 7~8.9 as long as there is trace amount of impurity ions such as iron and copper existing in the internal cooling water.

For a 300MW water-hydrogen-hydrogen cooled unit using deionized water as make-up water, the internal cooling water is processed by small sodium-type mix-bed, whose ratio of cation resin and anion resin is 2.7:1. Its water quality is as follows: The conductivity is below 0.5 μs/cm, hardness is 0, pH is between 7 and 8, and the concentration of copper is below 10μg/L [5].

3 Conclusions

1) The corrosion of generator stator hollow copper conductor is caused by oxygen and accelerated by carbon dioxide.

2) For internal water cooling systems which are airtight, the corrosion of the hollow copper conductor can be prevented through keeping foreign oxygen and carbon dioxide from entering the system, and the amount of oxygen in the internal water can be lowered by blowing high purity nitrogen.

3) For systems not airtight, the corrosion of the hollow copper conductor can be inhibited through lowering the amount of oxygen to some extent by sealing and increasing pH value by processing part of cooling water with bypass small flow sodium-type mix-bed.

Of course, not only hollow copper conductor can be prevented from corrosion, but also the internal cooling water quality can be adjusted better when the internal water cooling systems are airtight, and pH of the cooling water is increased by processing part of cooling water with bypass small flow sodium-type mix-bed.

REFERENCES

[1] Gong Xunjie, “The corrosion and protection of the thermal equipment,” The Chinese Electrical Power Press, Beijing, 1998.

[2] Zhang Enkui, “The cause of generator’s inner cooling water-quality worsening in Shuangliao power plant and corresponding treatment,” Jilin Electric Power Technology, Vol. 1, pp. 40-41, 2000.

[3] Zhang Jianli and Li Baoguo, “The optimization of the inner cooling-water of the generator’s stator,” North-China Electric Power Technology, Vol. 4, pp. 1-3, 2003.

[4] Xie xuejun, Pan Ling, et al., “Potential-pH chart for copper-water system and controlling pH of internal cooling water of generator to prevent corrosion,” Corrosion Science and Protection Technology, Vol. 19, No. 3, 2007.

[5] He Shaohong, “Studies on tubular copper conductor corrosion of the inner-cooling water system and corresponding protection,” Sichuan Electric Power Technology, Vol. 6, pp. 6-8, 2000.

Energy and Power Engineering, **2009, 21-27**
doi:10.4236/epe.2009.11004 Published Online August 2009 (http://www.scirp.org/journal/epe)

Scientific Research

Fault Detection Based on Hierarchical Cluster Analysis in Wide Area Backup Protection System

Yagang ZHANG, Jinfang ZHANG, Jing MA, Zengping WANG
Key Laboratory of Power System Protection and Dynamic Security Monitoring and Control under Ministry of Education, North China Electric Power University, Baoding, China
Email: yagangzhang@gmail.com

Abstract: In wide area backup protection of electric power systems, the prerequisite of protection device's accurate, fast and reliable performance is its corresponding fault type and fault location can be discriminated quickly and defined exactly. In our study, global information will be introduced into the backup protection system. By analyzing and computing real-time PMU measurements, basing on cluster analysis theory, we are using mainly hierarchical cluster analysis to search after the statistical laws of electrical quantities' marked changes. Then we carry out fast and exact detection of fault components and fault sections, and finally accomplish fault isolation. The facts show that the fault detection of fault component (fault section) can be performed successfully by hierarchical cluster analysis and calculation. The results of hierarchical cluster analysis are accurate and reliable, and the dendrograms of hierarchical cluster analysis are in intuition.

Keywords: wide area backup protection, phasor measurement unit, PMU, wide area measurement system, WAMS, fault detection, cluster analysis

1 Introduction

Electric power system is one of the most complex artificial systems in this world, which safe, steady, economical and reliable operation plays a very important part in guaranteeing socioeconomic development, even in safeguarding social stability. In early 2008, the infrequent disaster of snow and ice that occurred in the south of China had confirmed it again. The complexity of electric power system is determined by its characteristics about constitution, configuration, operation, organization, etc., which has caused many disastrous accidents, such as the large-scale blackout of America-Canada electric power system on August 14, 2003, the large-scale blackout of Chinese Hainan electricity grid on September 26, 2005. In order to resolve this difficult problem, some methods and technologies that can reflect modern science and technology level have been introduced into this domain, such as computer and communication technology, control technology, superconduct and new materials technology and so on. Obviously, no matter what we adopt new analytical method or technical means, we must have a distinct recognition of electric power system itself and its complexity, and increase continuously analysis, operation and control level [1-3].

Relay protection is the first line of guaranteeing large-scale electricity grid's safety. The faults in electric power system are inevitable. If protection devices can operate rightly, quickly and reliably, the deterioration of system status will be checked effectively, then it will play a decisive role to protect electricity grid's safe operation. Otherwise, it will accelerate system crashes, as a result, large-scale and long-time power blackout will continue. After counting seventeen years accident data in electric power system, North American Electric Reliability Council (NERC) has found: 63% accidents in electric power system are concerned with the incorrect operation of relay protection. The large-scale power blackouts occurred in China and other countries of the last thirty years have also indicated: the large-scale power blackout accidents are often raised from the improper cooperation or chain reaction of protection devices. The large-scale blackout of America-Canada electric power system was just because the removal of four connection lines between Akron and Cleveland in northern Ohio by backup protection for overload, and the accident spread rapidly. The backup protection in current electricity grid is only reflecting the information of protection installation position, which will be affected by topological connecting relations and operation modes. In order to guarantee its reliability, we can only carry through configuration and setting according to the most rigorous condition. In order to guarantee its selectivity, we have to sacrifice the rapidity and sensitivity of backup protection [4][5]. In recent years, the appearance of wide area measurement system (WAMS) affords the possibility for introducing system information into backup protection system. WAMS can obtain synchronously electrical measurements in the whole power system, and realize power system dynamic process monitoring and control. It can also decrease the update speed of measurements from seconds to tens of millisecond, and create condition to realize power system dynamic process control, which will help us carry through backup protection design based on global optimal angles of electricity grid, and afford the possibility for resolving dynamic security monitoring, control and protection of complex large-scale electricity grid.

When electric power system operates from normal state to failure or abnormal operates, its electric quantities (current magnitude, voltage magnitude and their angles, etc.) may change significantly. In our researches, global information will be introduced into the backup protection system. After some accidents, utilizing real-time measurements of phasor measurement unit (PMU) [6-10], basing on multivariate statistical analysis theory [11-13], we are using mainly cluster analysis technology [14-19], and seeking after for statistical laws of electrical quantities' marked changes. Then we can carry out fast and exact detection of fault components and fault sections, and hereby ascertain protection components associated with them. Finally we can accomplish fast and exact fault isolation.

The cluster analysis theory is one of multivariate statistical analysis theory, which is a synthetical analysis theory. In recent years, as the development of computer application technology and the demand of scientific research and production, multivariate statistical analysis theory has been applied successfully to many researches of various fields, such as geology, weather, hydrology, iatrology, industry, agriculture, and economy, etc. It has been an efficient theory that can resolve different kinds of complex problems. Basing on statistical theory, we have carried out large numbers of basic researches in nonlinear dynamical systems [20-22]. In this paper, we are using mainly cluster analysis of multivariate statistical analysis theory to resolve fault detection problem in wide area backup protection of electric power systems.

2 Cluster Analysis Theory

Theories of classification come from philosophy, mathematics, statistics, psychology, computer science, linguistics, biology, medicine, and other areas. Cluster analysis can also be named classification, which is concerned with researching the relationships within a group of objects in order to establish whether or not the data can be summarized validly by a small number of clusters of similar objects. That is, cluster analysis encompasses the methods used to:

- Identify the clusters in the original data;
- Determine the number of clusters in the original data;
- Validate the clusters found in the original data.

Cluster analysis has great strength in data analysis and has been applied successfully to the researches of various fields.

Suppose there are n samples, each sample has m indexes (variables), the observation data can be expressed as,

$$x_{ij} \quad (i = 1, \cdots, n, \ \ j = 1, \cdots, m)$$

In these data, the definition of mean is:

$$\overline{x}_j = \frac{1}{n}\sum_{t=1}^{n} x_{tj} \quad (j = 1, 2, \cdots, m)$$

the definition of standard deviation is:

$$S_j = \sqrt{\frac{1}{n-1}\sum_{t=1}^{n}(x_{tj} - \overline{x}_j)^2} \quad (j = 1, 2, \cdots, m).$$

2.1 The Distance and Similar Coefficient Between Samples

The most commonly used measurement that describes the degree of relationship is distance, d_{ij} is usually denoted the distance between samples $X_{(i)}$ and $X_{(j)}$, the general demands are:

(1). $d_{ij} \geq 0$, for arbitrary i, j, and $d_{ij} = 0 \Leftrightarrow X_{(i)} = X_{(j)}$;

(2). $d_{ij} = d_{ji}$, for arbitrary i, j;

(3). $d_{ij} \leq d_{ik} + d_{kj}$, for arbitrary i, j, k (Triangle inequality).

The distance definitions in common use include:

1) Minkovski distance

$$d_{ij}(q) = [\sum_{t=1}^{m}\left|x_{it} - x_{jt}\right|^q]^{\frac{1}{q}} \quad (i, j = 1, 2, \cdots, n).$$

2) Lance distance ($x_{ij} > 0$)

$$d_{ij}(L) = \frac{1}{m}\sum_{t=1}^{m}\frac{\left|x_{it} - x_{jt}\right|}{(x_{it} + x_{jt})}, \quad (i, j = 1, 2, \cdots, n).$$

This is a measure without dimension, and it is insensitive to big singular values.

3) Mahalanobis distance

$$d_{ij}(M) = (X_{(i)} - X_{(j)})' S^{-1}(X_{(i)} - X_{(j)}) \quad (i, j = 1, 2, \cdots, n).$$

Hereinto, S^{-1} is an inverses matrix of samples' covariance matrix.

4) Oblique space distance

In order to overcome the influence of relativity between variables, one can define the distance of oblique space:

$$d_{ij} = [\frac{1}{m^2}\sum_{k=1}^{m}\sum_{l=1}^{m}(x_{ik} - x_{jk})(x_{il} - x_{jl}) r_{kl}]^{\frac{1}{2}} \quad (i, j = 1, 2, \cdots, n).$$

Hereinto, r_{kl} is the correlation coefficient between X_k and X_l.

2.2 The Similar Coefficient and Distance Between Variables

Suppose C_{ij} can be expressed as the similar coefficient between X_i and X_j, the general demands are:

(1). $C_{ij} = \pm 1 \Leftrightarrow X_i = aX_j \quad (a \neq 0,\ \text{constant})$;

(2). $\left|C_{ij}\right| \leq 1$, for arbitrary i, j;

(3). $C_{ij} = C_{ji}$, for arbitrary i, j.

$\left|C_{ij}\right|$ close to one means that X_i and X_j have near relationship, otherwise, C_{ij} close to zero means that they have distant relationship. The similar coefficients in common use are included angle Cosine and correlation coefficient.

1) Included angle Cosine

These n observed values ($x_{1i}, x_{2i}, \cdots, x_{ni}$) of X_i can be regarded as vectors in n-dimensional space, and the angle α_{ij}'s Cosine of X_i and X_j is called similar coefficient of these two variables, namely

$$C_{ij}(1) = Cos[\alpha_{ij}] = \frac{\sum_{t=1}^{n} x_{ti} x_{tj}}{\sqrt{\sum_{t=1}^{n} x_{ti}^2}\sqrt{\sum_{t=1}^{n} x_{tj}^2}}. \quad (i, j = 1, 2, \cdots, m)$$

2) Correlation coefficient

The correlation coefficient is just the included angle Cosine after the data have been standardized. r_{ij} is expressed in common use the correlation coefficient of X_i and X_j, here we define it as $C_{ij}(2)$,

$$C_{ij}(2) = \frac{\sum_{t=1}^{n}(x_{ti} - \overline{x}_i)(x_{tj} - \overline{x}_j)}{\sqrt{\sum_{t=1}^{n}(x_{ti} - \overline{x}_i)^2}\sqrt{\sum_{t=1}^{n}(x_{tj} - \overline{x}_j)^2}}. \quad (i, j = 1, 2, \cdots, m)$$

3 Fault Detection Based on Hierarchical Cluster Analysis

Cluster analysis is commonly applied for statistical analyses of large amounts of experimental data exhibiting some kind of redundancy, which allows for compression of data to amount feasible for further exploration. Most common clustering algorithm choices are hierarchical cluster analysis.

The hierarchical cluster analysis does not require us to specify the desired number of clusters K, instead affording a cluster dendrogram. In practice, the choice can be based on some domain specific and often have subjective components. There are three steps to hierarchical cluster analysis. First, we must identify an appropriate proximity measure, for there are many metric methods, such as Minkovski distance, Lance distance, Mahalanobis distance, Oblique space distance and the similar coefficients, which is the best one? Second, we need to identify the appropriate cluster method for the data, include Between-groups linkage, Within-groups linkage, Nearest neighbor, Furthest neighbor, Centroid, Median and Ward's method, and so on. Finally, an appropriate stopping criterion is needed to identify the number of clusters in the hierarchy. According to the result of classification, how many clusters should we divide? The distance or similarity metric used in cluster is crucial for the success of the cluster method. Euclidean distance and Pearson correlation are among the most frequently used.

Firstly, let us consider IEEE9-Bus system, Figure 1 is its electric diagram. In the structure of electricity grid, Bus-1 appears single-phase to ground fault. By BPA programs, the vector-valued of corresponding variables is only exported one times in each period. Using these actual measurement data of corresponding variables, we can carry through hierarchical cluster analysis of fault component and non-fault component (fault section and non-fault section).

3.1 Fault Detection of IEEE9-Bus System Based on Node Positive Sequence Voltage

After computing IEEE9-Bus system, we can get node po-

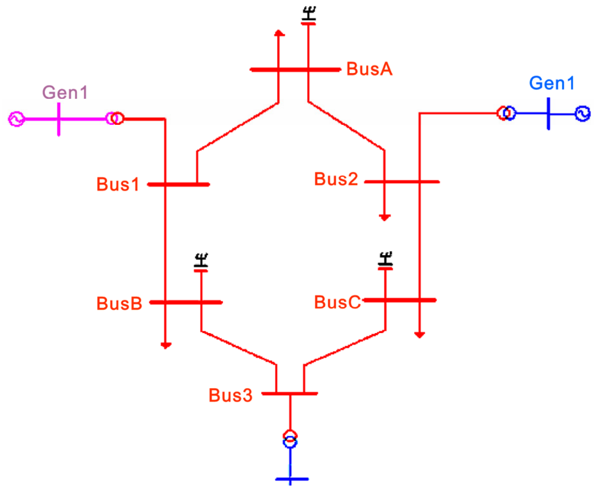

Figure 1. Electric diagram of IEEE 9-Bus system

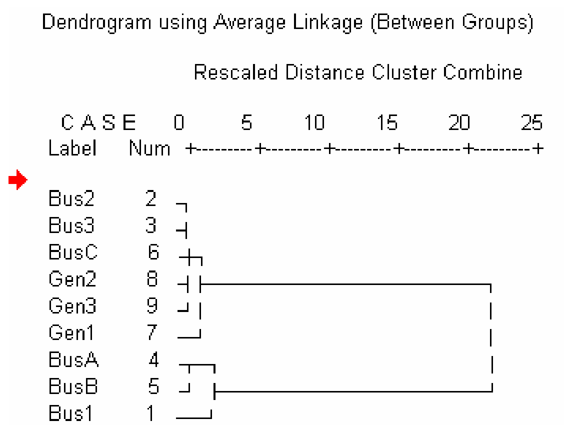

Figure 2. The dendrogram of hierarchical cluster analysis based on node positive sequence voltage

sitive sequence voltages at T_{-1}, T_0 (Fault) and T_1 three times. (The reason that we only choose three times data is because it must satisfy the actual sampling-rate of PMU and the control time of the wide area backup protection system.) Figure 2 is the dendrogram of hierarchical cluster analysis based on node positive sequence voltage.

It can be found easily out from Figure 2 that Bus-1 has remarkable difference with other buses, and the fault characteristic is obvious. Because Bus-A and Bus-B are directly connected with Bus-1, Bus-A, Bus-B and Bus-1 can be regarded as a cluster. In fact Bus-1, Bus-A and Bus-B have constituted accurately the fault section. These results are entirely identical with the fault location set in advance, so we can confirm exactly fault location by the hierarchical cluster analysis based on node positive sequence voltage.

3.2 Fault Detection of IEEE9-Bus System Based on Node Negative Sequence Voltage

By BPA programs, we can also get node negative sequence voltages at T_{-1}, T_0 (Fault) and T_1 three times. Figure 3 is the dendrogram of hierarchical cluster analysis based on node negative sequence voltage.

Figure 3 shows that the difference of Bus-1 and other Buses is more distinct by hierarchical cluster analysis based on node negative sequence voltage. At the same time, Bus-A, Bus-B and Bus-1 can still be regarded as a cluster, of course, they have also constituted accurately the fault section. These results of fault detection based on node negative sequence voltage are identical with the results of fault detection based on node positive sequence voltage, and both of them are fitting completely the fault location set in advance. So, it can also identify effectively fault location that using hierarchical cluster analysis based on node negative sequence voltage.

Now let us further consider IEEE39-Bus system, Figure 4 is its electric diagram. In the structure of electricity grid, Bus-18 appears three-phase short-circuit to ground fault. By BPA programs, the vector-valued of corresponding variables are only exported one time in each period. Using these actual measurement data of corresponding variables, we can carry through hierarchical

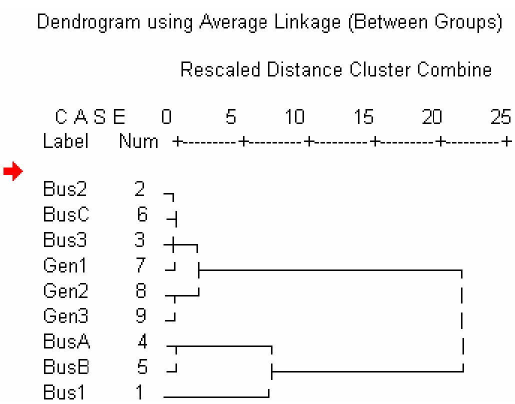

Figure 3. The dendrogram of hierarchical cluster analysis based on node negative sequence voltage

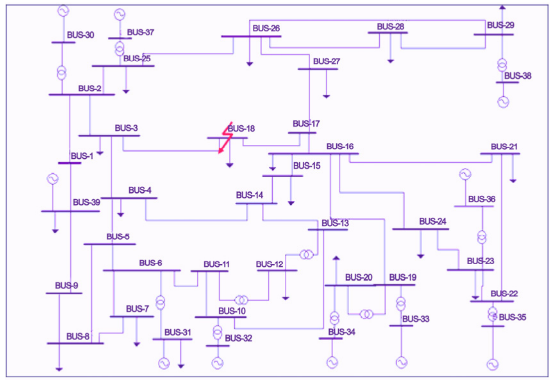

Figure 4. Electric diagram of IEEE 39-Bus system

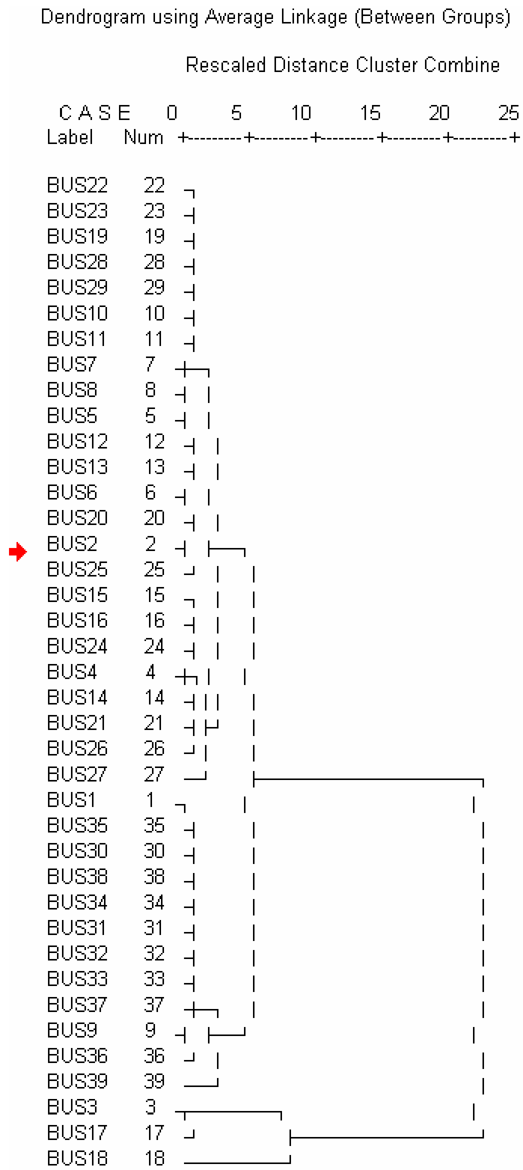

Figure 5. The dendrogram of hierarchical cluster analysis based on node positive sequence voltage

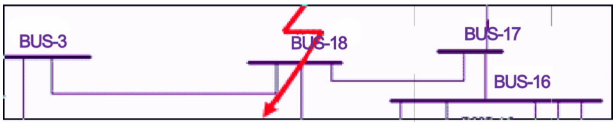

Figure 6. Branch set around BUS-18 fault node

cluster analysis of fault component and non-fault component (fault section and non-fault section).

3.3 Fault Detection of IEEE39-Bus System Based on Node Positive Sequence Voltage

Likewise, we calculate the node positive sequence voltage at T_{-1} , T_0 (Fault) and T_1 three times. Figure 5 is the dendrogram of hierarchical cluster analysis based on node positive sequence voltage.

In the hierarchical cluster analysis based on node positive sequence voltage, the fault characteristic of Bus-18 is very obvious. Bus-18, Bus-3 and Bus-17 can be regarded as a cluster. For Bus-3 and Bus-17 are directly connected with Bus-18, the fault of Bus-18 will undoubtedly affect its adjacent nodes, as the case stands, Bus-18, Bus-3 and Bus-17 have also constituted accurately the fault section. Figure 6 is the branch set around Bus-18 fault node. So, in accordance with three-phase short-circuit to ground fault, based on node positive sequence voltage, the fault location can be detected exactly by the hierarchical cluster analysis.

These instances have fully proven that fault detection of fault component (fault section) can be performed by hierarchical cluster analysis and calculation. The results of hierarchical cluster analysis are accurate and reliable, and the dendrograms of hierarchical cluster analysis are in intuition.

4 Conclusions and Discussion

In wide area backup protection of electric power systems, the prerequisite of protection device's accurate, fast and reliable performance is its corresponding fault type and fault location can be discriminated quickly and defined exactly. In our researches, global information has been introduced into the backup protection system, basing on cluster analysis theory, we are using mainly hierarchical cluster analysis technology, and seeking after for statistical laws of electrical quantities' marked changes by analyzing and computing real-time PMU measurements, thereby we carry out fast and exact detection of fault components and fault sections, and finally accomplish fault isolation.

Multivariate statistical analysis theory is an efficient theory that can resolve different kinds of complex problems. It has been applied successfully to many researches of various fields, and can analyze statistical law contained within subject, even multi-object and multi-index are associated together. In this paper, we are using mainly hierarchical cluster analysis of multivariate statistical analysis theory to resolve fault detection problem in wide area backup protection of electric power systems, and have got some ideal results. In the study of electric power systems, multivariate statistical analysis theory must also have a good prospect of application.

Acknowledgements

This research was supported partly by Key Program of National Natural Science Foundation of China (50837002) and the Science Foundation for the Doctors of NCEPU.

REFERENCES

[1] J. X. Yuan, "Wide area protection and emergency control to prevent large scale blackout," China Electric Power Press, Beijing, 2007.

[2] L. Ye, "Study on sustainable development strategy of electric power in China in 2020," Electric Power, Vol. 36, No. 10, 1-72003.

[3] Y. S. Xue, "Interactions between power market stability and power system stability," Automation of Electric Power Systems, Vol. 26, No. 21–22, pp. 1-6, 1-4, 2002.

[4] Q. X. Yang, "A review of the application of WAMS information in electric power system protective relaying," Modern Electric Power, Vol. 23, No. 3, pp. 1, 2006.

[5] J. Yi and X. X. Zhou, "A survey on power system wide-area protection and control," Power System Technology, Vol. 30, No. 8, pp. 7-13, 2006.

[6] A. G. Phadke and J. S. Thorp, "Synchronized phasor measurements and their applications," Springer-Verlag, New York, 2008.

[7] T. S. Bi, X. H. Qin, and Q. X. Yang, "A novel hybrid state estimator for including synchronized phasor measurements," Electric Power Systems Research, Vol. 78, No. 8, pp. 1343-1352, 2008.

[8] C. Wang, C. X. Dou, X. B. Li, and Q. Q. Jia, "A WAMS/PMU-based fault location technique," Electric Power Systems Research, Vol. 77, No. 8, pp. 936-945, 2007.

[9] C. Rakpenthai, S. Premrudeepreechacharn, S. Uatrongjit, and N. R. Watson, "Measurement placement for power system state estimation using decomposition technique," Electric Power Systems Research, Vol. 75, No. 1, pp. 41-49, 2005.

[10] J. N. Peng, Y. Z. Sun, and H. F. Wang, "Optimal PMU placement for full network observability using Tabu search algorithm," International Journal of Electrical Power & Energy Systems, Vol. 28, No. 4, pp. 223-231, 2006.

[11] X. Q. He, "Morden statistical analysis methods and applications," China Renmin University Press, Beijing, 2007.

[12] X. L. Yu and X. S. Ren, "Multivariate statistical analysis," China Statistic Press, Beijing, 1998.

[13] Y. T. Zhang and K. T. Fang, "Introduction to multivariate statistical analysis," Science Press, Beijing, 1982.

[14] A. Z. Arifin and A. Asano, "Image segmentation by histogram thresholding using hierarchical cluster analysis," Pattern Recognition Letters, Vol. 27, No. 13, pp. 1515-1521, 2006.

[15] X. Otazu and O. Pujol, "Wavelet based approach to cluster analysis: Application on low dimensional data sets," Pattern Recognition Letters, Vol. 27, NO. 14, pp.1590-1605, 2006.

[16] H. S. Park and D. K. Baik, "A study for control of client value using cluster analysis," Journal of Network and Computer Applications, Vol. 29, No. 4, pp. 262-276, 2006.

[17] V. Tola, F. Lillo, M. Gallegati, and R. N. Mantegna, "Cluster analysis for portfolio optimization," Journal of Economic Dynamics and Control, Vol. 32, No. 1, pp. 235-258, 2008.

[18] W. X. Zhao, P. K. Hopke, and K. A. Prather, "Comparison of two cluster analysis methods using single particle mass spectra," Atmospheric Environment, Vol. 42, No. 5, pp. 881-892, 2008.

[19] M. Templ, P. Filzmoser, and C. Reimann, "Cluster analysis applied to regional geochemical data: Problems and possibilities," Applied Geochemistry, Vol. 23, No. 8, pp. 2198-2213, 2008.

[20] Y. G. Zhang, P. Zhang, and H. F. Shi, "Statistic character in nonlinear systems," Proceedings of the Sixth International Conference on Machine Learning and Cybernetics, Hong Kong, Vol. 5, pp. 2598-2602, 2007.

[21] Y. G. Zhang, C. J. Wang, and Z. Zhou, "Inherent randomicity in 4-symbolic dynamics," Chaos, Solitons and Fractals, Vol. 28, No. 1, pp. 236-243, 2006.

[22] Y. G. Zhang and C. J. Wang, "Multiformity of inherent randomicity and visitation density in *n*-symbolic dynamics," Chaos, Solitons and Fractals, Vol. 33, No. 2, pp. 685-694, 2007.

Energy and Power Engineering, **2009, 28-37**
doi:10.4236/epe.2009.11005 Published Online August 2009 (http://www.scirp.org/journal/epe)

Effects of Lower Heat Value Fuel on the Operations of Micro-Gas Turbine

Aiguo LIU, Yiwu WENG
Key Laboratory of Machinery and Power Engineering of Education Ministry, Shanghai Jiao Tong University, Shanghai, China
Email: *liuaiguo*119*@gmail.com*

Abstract: The characteristics of fuel from biomass, coal and some waste materials are lower heat value and different compositions. The lower heat value fuel (LHVF) can be used on power engine such as boiler, gas engine and gas turbine. Some laboratory and pilot work have been done, but the work done on micro-gas turbine is still limited. The characteristics of LHVF can cause the operations change of micro-gas turbine designed for nature gas. Some possible adjustment and modification methods were mentioned for the use of LHVF on micro-gas turbine. One kind of representative LHVF was chosen and the operations of micro-gas turbine were analyzed. The temperature field and the non-uniformity scale of temperature distribution of combustor were calculated using FLUENT. The feasibility of different adjustment and modification methods were analyzed according to the efficiency, output power and the non-uniformity scale of temperature distribution.

Keywords: lower heat value fuel, micro-gas turbine, operations

1 Introduction

The distribution of LHVF from biomass, coal and waste materials is wide and the energy reserves are huge [1]. Effective use of the LHVF is becoming an attractive project, and much work is being done in this field. The characteristics of LHVF are lower heat value and different combustible compositions compared with nature gas. Heat values of the fuel gases depend on the process, but are typically one-tenth to one-half that of natural gas [2].

It will be different for the use of LHVF compared with traditional fuel according to its characteristics, so some different methods have ever been mentioned for the use of low heat value fuel such as catalytic combustion [3-5]. Efficient conversion of LHVF to electrical power can be accomplished by gas turbines, preferably in combined cycle mode, where thermal efficiencies can be greater than 65%. Simple open cycle, high pressure ratio machines can achieve efficiencies greater than 40% and form the basis for Integrated Gasification Combined Cycles [6]. Usually the combustion chamber of gas turbine was designed for higher heat value fuel, and some problems will appear when using LHVF as fuel. Catalytic combustion chamber can take the place of traditional one for the LHVF, but some defects will appear such as higher pressure and loss, slow reaction rate and so on. So the traditional combustion chamber is still important for the use of LHVF.

Primary issue for the gas turbine combustor when using LHVF is its large volumetric flows. The operations of micro-gas turbine will be changed and even stop work. The gas turbine should be adjusted and even modified to make the micro-gas turbine work smoothly. In this paper the effects of LHVF on the micro-gas turbine are firstly discussed, and then some possible methods of adjustment and modification are mentioned. The effects of mentioned methods to the operations of micro-gas turbine were presented and discussed. The feasibility was also discussed. At last the temperature field of combustion chamber was presented. The maximum temperature, average temperature, and non-uniformity coefficient at the outlet of combustor were calculated for the judgment of the feasibility.

2 Model Description

2.1 LHVF Model

The combustible components and heat value of LHVF are different since they are from different way such as biomass gasification, blast furnace tar and the coal mine ventilation air [1][7]. The compositions of 3 representative kinds of LHVF were shown in Table 1. The main combustible components from biomass gasification and blast furnace tar are hydrogen and carbon monoxide and in the coal mine ventilation is methane. But the effects of LHVF on the operations of micro-gas turbine are the same, so we choose a representative low heat value fuel from biomass gasification as an example to analyze. The LHVF includes different combustible components and the fuel is deal as composite variables. The thermodynamic property of gas is calculated according to the calculation manner of mixed fuel with incombustible component [8].

2.2 Micro-Gas Turbine Model

All of the calculations are based on the modeling of the micro-gas turbine C30 from CAPSTONE using the software of Matlab/Simulink [9]. The gas turbine is a single-shaft micro-gas turbine equipped with centrifugal compressor, radial turbine, combustion chamber and recuperator. The design compressor pressure ratio is 3.2 and the turbine inlet temperature (TIT) is 1 173K. The design mass flow of 0.31 kg s^{-1} is assumed to produce roughly 30 kW power with an efficiency of 26% at ISO conditions. This single shaft gas turbine is capable of running at different shaft speed which generates higher flexibility.

The modeling of micro-gas turbine is possible by utilizing real steady state engine performance data [10]. In gas turbine cycles, the changed relationship between mass flow and pressure will cause a change in the operation point and efficiency. The features of a compressor can be described as functions of pressure ratio π_C, reduced flow $G\sqrt{T}/P$, reduced speed $n/\sqrt{T}$ and efficiency η_C. Performance maps are introduced for determination of the pressure and efficiency as a function of mass flow and shaft speed for the description of compressor. Figure 1 shows the performance map of compressor. It is assumed that off-design thermodynamic and flow processes are characterized by a continuous progression along the steady-state performance curves.

The turbine model can be processed using a similar method.

In the combustion chamber, the fuels is burned away which increases the temperature of the gas. The following reactions are considered in calculating the exit gas temperature of the combustor:

$$CO + 1/2O_2 = CO_2 + Q_{CO} \quad \textbf{(1)}$$

Table 1. Components in different low heat value fuel

Composition / %	Biomass gas	Blast furnace tar	Coal mine ventilation air
CO_2	13.0	18	0
O_2	1.65	0	20.79
CO	21.4	26	0
H_2	12.2	4	0
CH_4	1.87	2	1
N_2	49.88	60	78.21

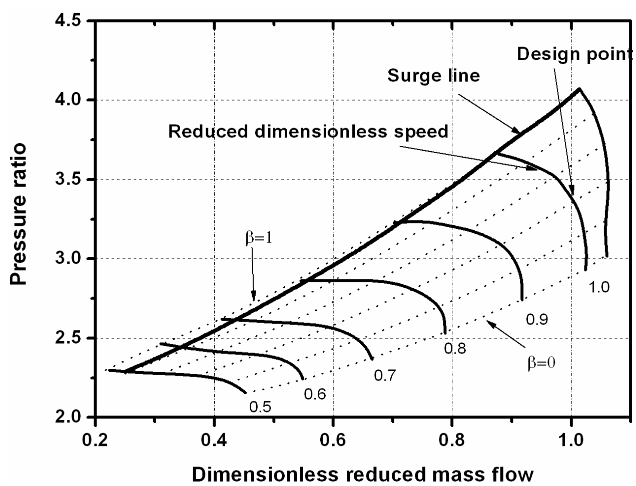

Figure 1. Equivalence circulates curve of compressor

$$H_2 + 1/2O_2 = H_2O + Q_{H_2} \quad (2)$$

$$CH_4 + 2O_2 = CO_2 + 2H_2O + Q_{CH_4} \quad (3)$$

Assuming that the process is adiabatic, the enthalpy of the reactants with combustion efficiency taken into account would be equal to the enthalpy of the products. Knowing the temperature of the reactants, the product temperature T_2 can be calculated by iteration as the properties of each product gas are temperature- dependent:

$$(\Delta h + Q_{CO} + Q_{H_2} + Q_{CH_4}) \cdot \varepsilon_{comb} = \sum_i n_i \int_{T_{std}}^{T_2} c_{pm} dT \quad (4)$$

where the Δh is the enthalpy change of reactions from the original status to the standard status, the combustion efficiency ε_{comb} was set conservatively at 98%, though it can be as high as 99.5%. i represents each gas composition of the product.

The schematic figure of the recuperator is shown in Figure 2 Setting $p2$、$h2$、$p4$、$h4$ as the state variables， we can get the following equations based on the mass and energy balance [11][12].

$$\frac{dp_2}{dt} = \frac{(m_2h_2 - m_1h_1 - q_h)}{V_{ht}(1 - c_{p2}/R_2)} \quad (5)$$

$$\frac{dh_2}{dt} = \frac{(m_1h_1 - m_2h_2 + q_h) + (h_2 - h_2R_2/c_{p2})(m_2 - m_1)}{V_{ht}(\rho_2 - R_2\rho_2/c_{p2})} \quad (6)$$

$$\frac{dp_4}{dt} = \frac{(m_4h_4 - m_3h_3 + q_c)}{V_{cl}(1 - c_{p4}/R_4)} \quad (7)$$

$$\frac{dh_4}{dt} = \frac{(m_3h_3 - m_4h_4 - q_h) + (h_4 - h_4R_4/c_{p4})(m_4 - m_3)}{V_{cl}(\rho_4 - R_4\rho_4/c_{p4})} \quad (8)$$

where $q_{h,}$, q_c are the heat transfer between fluid (hot and cold) and the wall of the recuperator.

$$q_h = \alpha_h A_h (T_{12} - T_m) \quad (9)$$

$$q_c = \alpha_c A_c (T_m - T_{34}) \quad (10)$$

And the $T_{12} = \frac{T_1 + T_2}{2}$, $T_{34} = \frac{T_3 + T_4}{2}$ are the average value of inlet and outlet temperature respectively.

T_m is the average wall temperature between the hot and cold side gas.

$$\frac{dT_m}{dt} = \frac{1}{C_{pm}M_m}(q_h - q_c) \quad (11)$$

The power output from the gas turbine is obtained by using the following equation:

$$W_{GT} = \eta_{gen}(\eta_T W_t - W_c) - W_{aux} \quad (12)$$

where η_{gen} is the generator efficiency; η_T is the turbine mechanical efficiency; W_t ,W_c *and* W_{aux} are the turbine power, compressor power and auxiliary power respectively.

2.3 CFD Model of Combustion Chamber

The temperature field in the combustor will be changed; especially the temperature field of combustor outlet will have direct effect on the safety of turbine. The main analysis method of temperature field in combustor is CFD. Firstly the model was built by the software of PRO/E and the plot of gridding is completed by Gambit using non-structure gridding, the number of gridding is 223271. The plot of gridding is shown in Figure 3. And

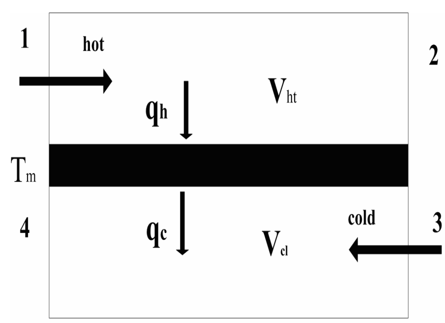

Figure 2. Schematic figure of heat transfer in the recuperator

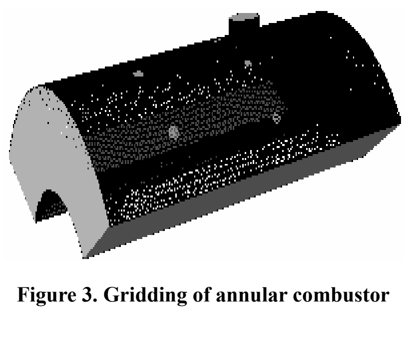

Figure 3. Gridding of annular combustor

then the model was solved by the software of FLUENT.

2.3.1 Flux Control Equation

The flux control equation is N-S equation, the turbulence in combustor using $\kappa-\varepsilon$ double equation model. The 3D flux N-S equation in pole coordinate is as follows:

$$\frac{1}{r}[\frac{\partial}{\partial x}(r\rho u\varphi)+\frac{\partial}{\partial r}(r\rho v\varphi)+\frac{\partial}{\partial \theta}(\rho w\varphi)]= \frac{1}{r}[\frac{\partial}{\partial x}(\gamma\Gamma_\varphi\frac{\partial\varphi}{\partial x})+\frac{\partial}{\partial r}(\gamma\Gamma_\varphi\frac{1}{r}\frac{\partial\varphi}{\partial r})+\frac{\partial}{\partial\theta}(\Gamma_\varphi\frac{1}{r}\frac{\partial\varphi}{\partial\theta})]+S_\varphi \quad (13)$$

2.3.2 Combustion Model

The actual combustion process is the interaction of turbulence and chemistry reaction, the chemistry reaction velocity is strong nonlinear and strong stiff. Usual chemistry reaction mechanism includes tens of composition and hundreds of base reaction and the difference of reaction time is large. So the quantity of calculation and storage is very large in the solution of actual problem. The different chemistry dynamics solution methods have been used aims at the different combustion phenomena in FLUENT. The model used in this calculation is the Species Transport model. This model is usually used in the premixed combustion, part premixed combustion and diffusion combustion. The chemistry reaction is usually simplified as single-step reaction. The solution of the composition transport equation and getting the time-averaged mass fraction of each composition is as follows:

$$\frac{\partial}{\partial t}(\rho Y_i)+\nabla(\rho\bar{v}Y_i)=-\nabla\bar{J}_i+R_i+S_i \quad (14)$$

The reaction source item of composition j is the production rate of composition j in all the reactions:

$$R_i=\sum_k R_{jk} \quad (15)$$

In the formula, the reaction velocity of composition j in reaction k can be solved with the Arrhenius formula.

3 Results and Discussion

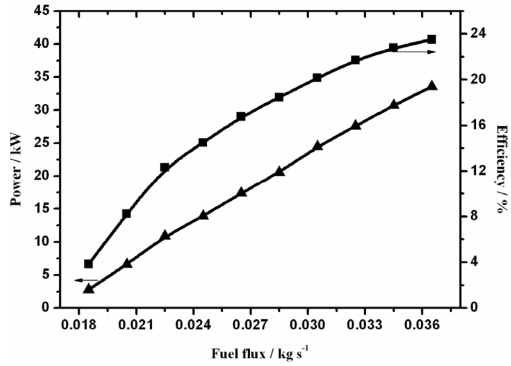

Figure 4. Relation of output power and efficiency to fuel flux

3.1 Effects of LHVF on the Micro-Gas Turbine

The energy provided by LHVF is less than the traditional fuel when the same fuel/air ratio was used. The fuel flux should be increased to improve the turbine inlet temperature. The relation of output power and efficiency with the fuel flux was shown in Figure 4 with the assumption of constant air flow.

The turbine inlet temperature (TIT) will increase with the increase of fuel flux which causes the increase of output power and efficiency. The TIT will not be the same with design value when the output power is the same with design value, so two special conditions have been presented according to the calculation. The first one was the output power of micro-gas turbine attained the design value (case2), the second one was the turbine inlet temperature attained the design value (case3). The calculation results were shown in Figure 5 and were compared with the design value (case1).

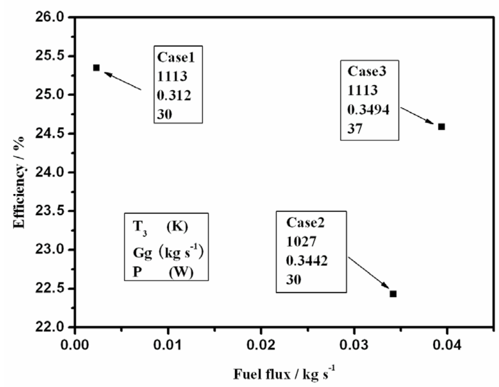

Figure 5. 3 different conditions

From the calculation results in Figure 5 we can see the mass flow of fuel will be more than 14 times for case 2 and 16 times for case 3 compared with case1. The efficiency of case 2 and case 3 are both lower than case1and the output power is higher in case 3. The decrease of efficiency is influenced by both the increase of the fuel flux entering combustor without being preheated and the decrease of turbine efficiency. About the increase of output power in case 3 is due to the increase of gas passing through turbine.

The mass flow of low heat value fuel will be more 10 times than the design value. There is flux difference between compressor and turbine, so the compressor and turbine can not match together. Some work should be done on the micro-gas turbine to make the compressor and turbine match again.

3.2 Adjustment and Modification of Micro-Gas Turbine

Some experience has been gained and adopted in heavy gas turbine for LHVF [13-16]. The heavy gas turbine can be adjusted in large scale to fit the operations of LHVF. For example, the flow ability of turbine can be increased 10%, the compression ratio can be increased 12% and the output power can be increase 20% for the 9F model heavy gas turbine from GE [17]. At the same time there exist variable-area nozzles which can be adjusted to decrease the flux of compressor. The adjustment methods used in heavy gas turbine do not all fit to the micro-gas turbine because the operations of micro-gas turbine are different from heavy gas turbine [18]. Some possible adjustment and modification methods were mentioned in this chapter and the feasibility was discussed.

3.2.1 Adjustment of Micro-Gas Turbine

1) Pressure ratio and TIT

The adjustment of operation parameters was viewed as the simplest method to match the compressor and turbine according to the experience of heavy gas turbine. The pressure ratio of compressor should be increased as high as possible because which can not only increase the flow ability of turbine but also decrease the flow ability of compressor. But the compression ratio can not be increased very high, so the turbine inlet temperature should be decreased at the same time for the purpose of matching. The adjustment process should be: firstly the compression ratio was increased as high as possible and then decreasing the TIT until the matching was achieved. The operation parameters were shown as case4 in Table 2 for the adjustment of pressure ratio and TIT. From the results it was found that the efficiency and output power both decreased and the compressor has been near the surge boundary. So this adjustment method is inapplicable to the micro-gas turbine in the view of efficiency and output power.

Table 2. Four operation cases of micro-gas turbine in different condition

		Case1	Case4	Case5	Case6
Compressor	Rotation speed	N	N	0.95N	0.9N
	Compression ratio	3.2	3.257	3.09	2.634
	Outlet flux/ kg/s	0.31	0.288	0.2782	0.2688
	Outlet temperature / K	444	446.8	439.6	418
	Power /kW	47.1	44.42	40.8	33.33
	Outlet pressure/ kPa	319.2976	324.98	308.3	262.8
	Efficiency	0.818	0.82	0.8176	0.8107
Combustion chamber	Fuel flux / kg /s	0.002368	0.02527	0.03224	0.03188
	Inlet temperature / K	839	662.7	807.9	886.2
	Outlet pressure / kPa	309.7	316.7	300.6	255.6
	Outlet temperature / K	1113	888.3	1072	1144
Turbine	Outlet temperature / K	912	718	877.5	964.1
	Outlet flux / kg/s	0.312368	0.3164	0.3135	0.3037
	Power /kW	77.1	62.61	70.72	63.35
	Efficiency	0.8164	0.8127	0.8072	0.8148
Micro-gas turbine	Output power / kW	30	17.69	30	30
	Efficiency / %	25.35	17.89	23.73	24.07

2) Rotation speed

The matching between compressor and turbine can also be realized by adjusting the compressor itself to reduce the compressor air flux. There are several ways to adjust the compressor [19]:

①Outlet throttle;

②Inlet throttle;

③Variable rotation speed.

Whichever method will result in the increase of power consumed by compressor, and the variable rotation speed adjustment is the best way in the view of power consumption.

The variable rotation speed adjustment was chosen and the relationship of efficiency and output power with compression ratio was shown in Figure 6 and Figure 7 when the rotation speed is 0.95N and 0.9N (N is the design rotation speed value) respectively. The operation parameters are listed in Table 3 as case5 and case6 while keeping the output power as design value.

The power generated by turbine will decrease when the rotation speed decreases, but the power consumed by compressor also decreases at the same time. So the output of micro-gas turbine also can achieve the design value, but the efficiency will decrease due to the decrease of turbine and compressor efficiency. When the rotation speed is 0.9N the turbine inlet temperature was higher than the design value for the design output power which can result exceeding temperature.

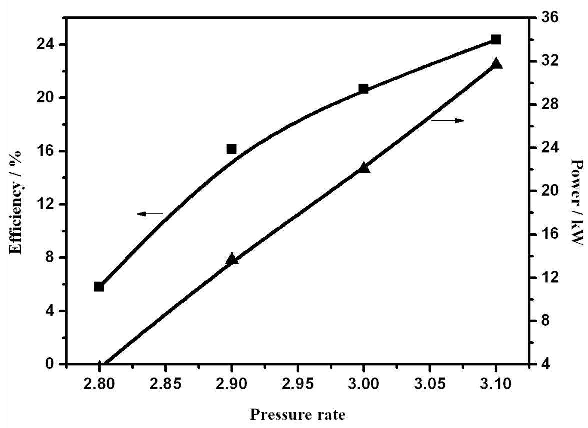

Figure 6. Efficiency and power at 0.95N

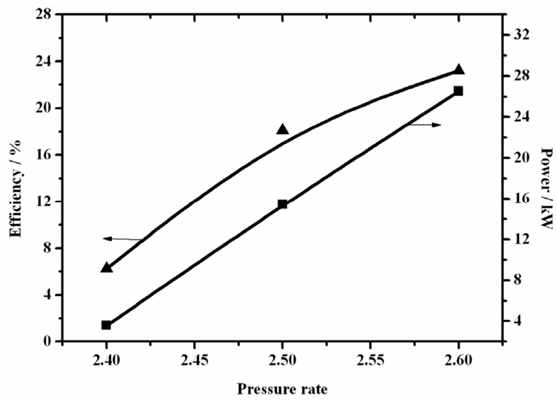

Figure 7. Efficiency and power at 0.9N

The matching between compressor and turbine can be achieved by the adjustment of the operation parameters of micro-gas turbine. But the adjustment is not good enough as it will cause the lower efficiency, exceeding temperature and even the danger of compressor surge.

3.2.2 Modification of Compressor and Turbine

In general the micro-gas turbine does not adopt the technology of variable-area nozzle or stationary blade [20], the vane of compressor is very thin and the modification of variable-area nozzle or stationary blade will be very difficult. But the advantages will be great in the view of the operations if the compressor and turbine can be modified.

Some theoretical calculations have been done on the supposing that the modification of compressor and turbine can be realized. The calculation started from the operation point in case4. Firstly was the modification of compressor. Starting from the operation point in case4 and then decreasing the flux of air while keeping the compression ratio unchanged. The turbine inlet temperature will increase due to the increase of fuel flux. The inlet temperature of turbine attained the design value and the output of micro-gas turbine was 35.02kW when the mass flow of air is 0.965 design value. For the purpose of protecting turbine the turbine inlet temperature should be kept constant after this point. This time the turbine inlet temperature was kept unchanged and the decrease of the compressor flux would result the decrease of power from turbine and micro-gas turbine until the output power reached the design value. The relation of efficiency and output power of micro-gas turbine with the decrease of mass flow of compressor was shown in Figure 8.

The operation can also be improved if the flux ability of turbine can be increased with modification. Changing the setting angle or height of stationary blade can increase the flux area of turbine and improve the operations. The calculation point also started from the operation point in case4. The turbine inlet temperature would increase with the increase of turbine flux ability which caused the increase of output power and efficiency until the turbine inlet temperature attained the design value. After this point the increase of flux ability of turbine will cause the decrease of the turbine inlet pressure and the compression ratio of compressor. The power and efficiency still increased slowly because the mass flow of gas keeps increasing at the highest temperature. The relation of power and efficiency with the increase of flux ability of turbine was shown in Figure 9.

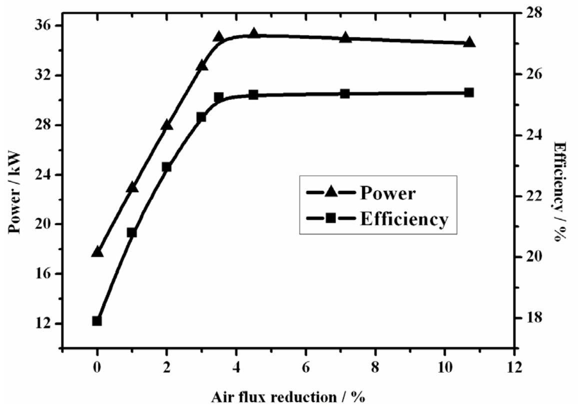

Figure 8. Effect of compressor flux decrease on efficiency and power

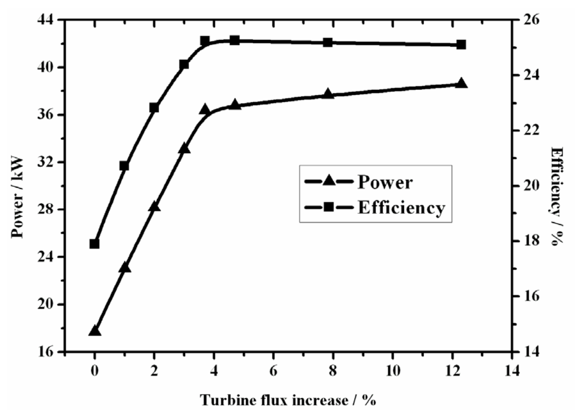

Figure 9. Effect of turbine flux increase on efficiency and power

The operations of micro-gas turbine were satisfactory with the modification of compressor and turbine. But the modification of compressor or turbine can cause the output of micro-gas turbine beyond the design value which maybe has effect on the structure of micro-gas turbine.

3.3 Temperature Field of Combustion Chamber

The matching problem can be solved by the methods mentioned above. But the temperature field in combustor will changed as the changed inlet conditions. The temperature fields in four different conditions were calculated which included the design condition, speed adjustment and the modification of compressor and turbine.

The main parameters for temperature field were maximum temperature, average temperature and non-uniformity coefficient which have effects on the safety of turbine. Figure 10(a) is the temperature distribution characteristic of combustor outlet and axis direction at design condition and it was also the example compared by the other conditions. The maximum temperature, minimum temperature, average temperature and non-uniformity coefficient were shown in Table 3. The non-uniformity coefficient A_t should be lower than 10% for the safety of turbine.

The temperature field and non-uniformity coefficient were shown in Figure 10(b) and Table 3 when the rotation speed was 0.9N and output power was design value. In the axis direction the high-temperature area become larger and at the combustion chamber outlet the maximum temperature and non-uniformity coefficient exceeded the safety margin. So the speed adjustment method was not feasible in the view of turbine safety.

The computation results shown in Figure 10(c) and 10(d) were the conditions when modifying the compres-

Table 3. Combustion chamber temperature characteristics

NO.	T_{max}	T_{min}	T_{ave}	At%
a	1179	1080	1119.2	5.4
b	1357	915	1092.3	24.3
c	1148	976	1063.2	8
d	1170	898	1072	9.2

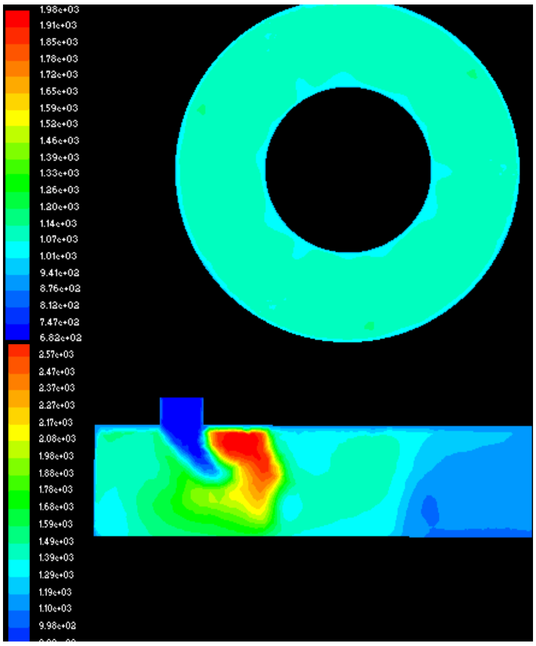

(a)

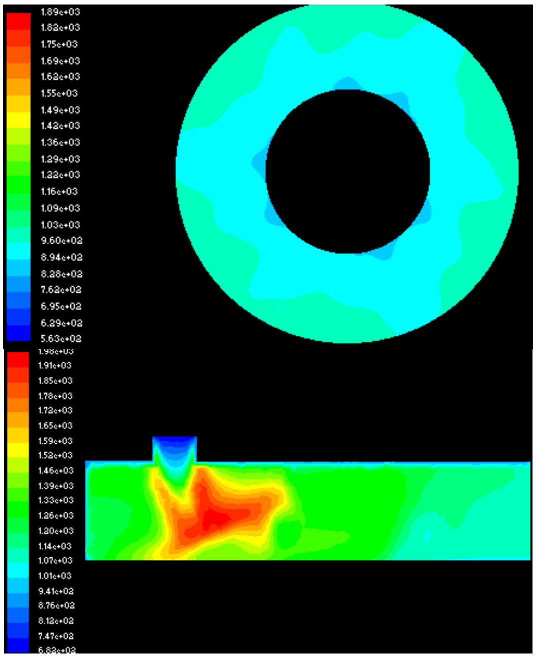

(b)

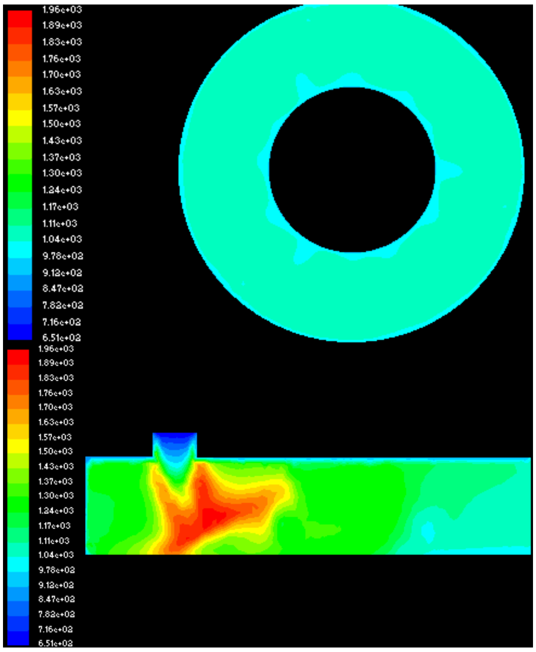

(c)

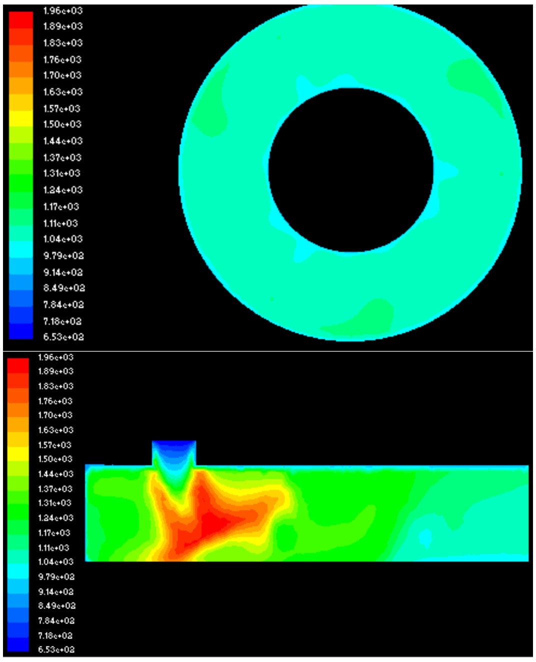

(d)

Figure 10. Outlet and axial temperature field

sor and turbine respectively. In the axis direction the high-temperature area was larger compared with a. The maximum temperature and non-uniformity coefficient at the turbine outlet can meet the safety need. In the view of temperature field the modification of compressor and turbine was feasible.

4 Conclusions

The problems caused by LHVF and some possible adjustment and modification methods have been presented and discussed in this paper. The operations and feasibilities using these methods on micro-gas turbine have been discussed according to the efficiency, output power and temperature field in combustion chamber.

1) Adjustment of operation parameters. The efficiency and output power will decrease when the operation parameters such as compression ratio, turbine inlet temperature are adjusted. So the adjustment of compression ratio and turbine inlet temperature is not feasible in the view of output, efficiency and safety. There are also some problems when adjusting the compressor speed. The matching problem can be solved by the speed adjustment but some additional problems will appear because the micro-gas turbine is coaxial. At the same time the temperature field distribution is uneven at the combustion chamber outlet which can cause the damage of turbine vane. So the adjustment of micro-gas turbine is not feasible to solve the problems caused by LHVF as heavy gas turbine.

2) The modification of compressor and turbine can solve the matching problem and the efficiency is high enough. The maximum temperature and the non-uniformity coefficient of combustion chamber are both in the limitation. So the modification to the compressor and turbine is a good method.

In this paper we only discuss the problem of matching and temperature field, but another problem is ignition and combustion stability. The fuel velocity will be increased which can cause the problem of ignition and combustion stability in combustion chamber. Some further studies about the fuel nozzle and combustion chamber should be made as heavy gas turbine.

Nomenclature

T_0	atmosphere temperature (k)
P_0	atmosphere pressure (Mpa)
T_{ex}	gas turbine exhaust temperature (k)
T_3	turbine inlet temperature (k)
G_g	turbine gas flux (kg/s)
P	gas turbine output (w)
N	micro-gas turbine design speed (96000r/m)
Eff	efficiency (%)
ϕ	the general variable, it can represent the velocity of u、v、w , turbulent kinetic energy, Turbulence Dissipation Rates, enthalpy, turbulence stress term and Duo-mixture fraction；
Γ_ϕ	turbulence transportation coefficient，
s	Source term
T_{max}	combustion chamber outlet max temperature (K)
T_{min}	combustion chamber outlet min temperature (K)
T_{ave}	combustion chamber outlet average temperature (K)
A_t	combustion chamber non-uniformity coefficient

Acknowledgements

We would like to acknowledge the National Science Foundation of China who provided the funding for this work. This work was partially supported by Shanghai government.

REFERENCES

[1] Shi Su and Jenny Agnew, "Catalytic combustion of coal mine ventilation air methane," Fuel, Vol. 85, pp. 1201-1210, 2006.

[2] G. Kelsall and M Cannon, "Combustion of low heating value gas in a gas turbine," Power Production from Biomass, Espoo, Finland, Vol. 2, March 1995.

[3] L. L. Smith, H. Karim, M. J. Castaldi, S. Etemad, and W. C. Pfefferle, "Rich-catalytic lean-burn combustion for fuel-flexible operation with ultra low emissions," Catalysis Today, Vol. 117, No. 4, pp. 438-446, 2006.

[4] Magnus Berg, E. Magnus Johansson, and Sven G. Järås, "Catalytic combustion of low heating value gas mixtures: Comparison between laboratory and pilot scale tests," Catalysis Today, Vol. 59, No. 1-2, pp. 117-130, 2000.

[5] Susie Wood and Andrew T. Harris, "Porous burners for lean-burn applications," Progress in Energy and Combustion Science, Vol. 34, No. 5, pp. 667-684, 2008.

[6] J. J. Witton, E. Noordally, and J. M. Przybylski, "Clean catalytic

combustion of low heat value fuels from gasification processes," Chemical Engineering Journal, Vol. 91, pp. 115-121, 2003.

[7] Magnus Berg, E. Magnus Johansson, and Sven G. Jaras, "Catalytic combustion of low heating value gas mixtures: Comparison between laboratory and pilot scale tests," Catalysis Today, Vol. 59, pp. 117-130, 2000.

[8] Piero Colonna and Paolo Silva, "Dense gas thermodynamic properties of single and multicomponent fluids for fluid dynamics simulations," Journal of Fluids Engineering, Vol. 125, No.3, pp. 414-427, 2003.

[9] Technology Reference, Capstone Model C30 Performance.

[10] H. S. Zhang, Y. W. Liu, M. Su, and S. L. Weng, "Simulation study on the speed regulation of gas turbine," Computer Simulation, Vol. 1, pp. 79-81, 2002.

[11] Zhang Huisheng, Weng Shilie, and Su Ming, "Dynamic modeling and simulation of distributed parameter heat exchanger," Processing of ME TUBRO EXPO, Nevada, GT2005-68293, 2005.

[12] Huisheng ZHANG, Shilie WENG, and Ming SU, "Evaluation of topping and bottoming cycle hybrid power plants with mcfc-micro turbine," ASME Paper GT2004-53397, 2004.

[13] Iskender G and Etienne Lebas, "Alternative fuels for industrial gas turbines (AFTUR)," Applied Thermal Engineering, Vol. 24, pp. 1655-1663, 2004.

[14] Belkacem Adouane, Peter Hoppesteyn, Wiebren de Jong, and Marco van der Wel, "Gas turbine combustor for biomass derived LCV gas, a first approach towards fuel-NOx modelling and experimental validation," Applied Thermal Engineering, Vol. 22, pp. 959-970, 2002.

[15] Greg Kelsall and Christian Troger, "Prediction and control of combustion instabilities in industrial gas turbines," Applied Thermal Engineering, Vol. 24, No. 2, pp. 1571-1582, 2004.

[16] KRISTER STAÊ HL and MAGNUS NEERGAARD, "IGCC power plant for biomass utilisation," Biomass and Bioenergy, Vaè Rnamo, Sweden, Vol. 15, No. 3, pp. 205-211, 1998.

[17] CHARLES E. NEILSON, "LM2500 gas turbine modifications for biomass fuel operation," Biomass and Bioenergy, Vol. 15, No. 3, pp. 269-273, 1998.

[18] Fabio Bozza, Maria Cristina Cameretti, and Raffaele Tuccillo. "Adapting the micro-gas turbine operation to variable thermal and electrical requirements," Transaction of the ASME, Vol. 127, pp. 514-524, 2005.

[19] Xi'an Jiaotong University Department of turbine compressor, "Centrifugal Compressor Principle," Machinery Industry Press, Beijing.

[20] Li Yansheng, "Centripetal turbine and centrifugal compressor," Machinery Industry Press.

Energy and Power Engineering, **2009, 38-43**
doi:10.4236/epe.2009.11006 Published Online August 2009 (http://www.scirp.org/journal/epe)

Study on Bifurcation and Chaos in Boost Converter Based on Energy Balance Model

Quanmin NIU, Zhizhong JU
Department of Information Countermeasure, Air Force Radar Academy, AFRA, Wuhan, China
Email: *nqm1@tom.com*

Abstract: Based on boost converter operating in discontinuous mode, this paper proposes an energy balance model (EBM) for analyzing bifurcation and chaos phenomena of capacitor energy and output voltage when the converter parameter is varying. It is found that the capacitor energy and output voltage dynamic behaviors exhibit the typical period-doubling route to chaos by increasing the feedback gain constant *K* of proportional controller. The accurate position of the first bifurcation point and the iterative diagram of the capacitor energy with every *K* can be derived from EBM. Finally, the underlying causes for bifurcations and chaos of a general class of nonlinear systems such as power converters are analyzed from the energy balance viewpoint. Comparing with the discrete iterative model, EBM is simple and high accuracy. This model can be easily developed on the nonlinear study of the other converters.

Keywords: power converter, nonlinear, bifurcation, chaos, energy balance model

1 Introduction

The bifurcation and chaos phenomena appeared in power system have becoming a focus subject at present. It is found that basic DC/DC converters exhibit bifurcation and chaos phenomena as well as parallel-connected DC/DC converters and PFC system. There are no unified methods in researching nonlinear power system. In the appeared literatures, the averaged model and the sampling data model are usually adopted in nonlinear analysis for DC/DC converters [1][2]. But the averaged model neglects the dynamic characteristic of the system at high frequency, and only can be used for analyzing the dynamic behavior at low frequency. This model has limitations as follows. Firstly, the dependence on initial condition for system dynamic behavior is neglected in small signal analysis and it can't predict dynamic behavior when the converters work in the saturated mode. Secondly, this model can't predict the instability of system under the fast-scale condition [3]. According to the periodic working characteristic of power system, the sampling data modeling method build the relationship between state variable at present sampling time instant and state variable at next sampling time instant. Based on this idea, four models named stroboscopic map model, synchronous switching map model, asynchronous switching map model and general two-by-two switching map model are given in [2] according to the different sampling time instant. These models are used to analyze nonlinear phenomena such as bifurcation and chaos. But some shortcomings exist in these models. For example, it is difficult to get accurate analytic models as the duty ratio of control pulses is the nonlinear function of state variables. If we neglect nonlinear effect on system transfer matrix, big errors and much amount of calculation will bring about. In order to improve the accuracy of simulation results, this paper proposes an energy balance model (EBM) for boost converter. According to energy balance principle, EBM was established and the dynamic behavior of the capacitor energy state was investigated. From the bifurcation diagrams of capacitor energy state and output voltage, EBM presented in this paper is more accurate than the stroboscopic map model presented in [4]. Furthermore,

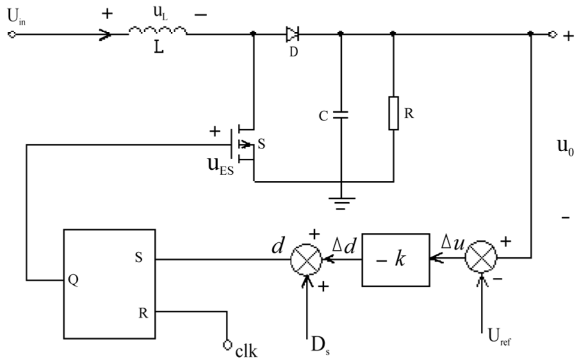

Figure 1. Schematic circuit diagram of closed-loop boost converter

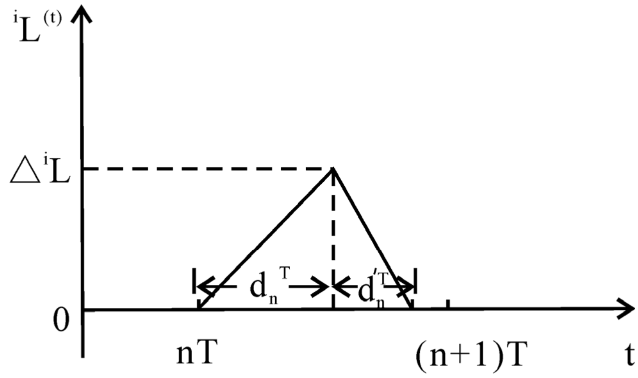

Figure 2. Inductor current waveform

energy bifurcation mechanism for power converters can be found from EBM.

2 Building Energy Balance Model

The circuit diagram of the closed-loop boost converter is shown in Figure 1. Suppose that boost converter works in DCM. The feedback gain constant of voltage amplifier is k and error signal Δu is amplified through the voltage amplifier. The amplified error voltage compares with saw-tooth wave signal and produces variable duty cycle control pulse. The variable duty cycle denotes Δd in Figure 1. The output voltage is regulated by changing Δd when input voltage and output load is fluctuating.

In one switching period $[nT,(n+1)T]$, the converter satisfies energy balance condition

$$\Delta E_{in} = \Delta E_R + \Delta E_C + \Delta E_L , \tag{1}$$

where ΔE_{in} 、 ΔE_R 、 ΔE_L 、 ΔE_c denote the energy supplied by input power, the energy consumed on resistance load, the storage energy in inductor and the storage energy in capacitor respectively in one switching period. In DCM converter, the inductor current always starts from zero, i.e., $\Delta E_L = 0$, so the energy balance formula is

$$\Delta E_{in} = \Delta E_R + \Delta E_c . \tag{2}$$

The current flowing out from input power equals to the current flowing into inductor in a switching period as shown in Figure 2.

According to Figure 2, we can write

$$\Delta i_L = \frac{U_{in}}{L} d_n T = \frac{U_{ref} - U_{in}}{L} d'_n T . \tag{3}$$

So, we obtain

$$d'_n = \frac{U_{in}}{U_{ref} - U_{in}} d_n . \tag{4}$$

ΔE_{in} can be written as

$$\begin{aligned}\Delta E_{in} &= U_{in} \int_{nT}^{(n+1)T} i_L(t)dt \approx \frac{1}{2} \Delta i_L (d_n + d'_n) T U_{in} \\ &= \frac{U_{in}{}^2 T^2}{2L} \frac{U_{ref}}{U_{ref} - U_{in}} d_n{}^2 \end{aligned} . \tag{5}$$

The energy consumed by load is

$$\begin{aligned}\Delta E_R &= \frac{1}{R} \int_{nT}^{(n+1)T} u_c{}^2(t)dt \approx \frac{T}{2} [\frac{u_{c,nT}{}^2}{R} + \frac{u_{c,(n+1)T}{}^2}{R}] \\ &= \frac{T}{RC} [E_{c,nT} + E_{c,(n+1)T}] \end{aligned} . \tag{6}$$

The storage energy in capacitor in one switching period is

$$\Delta E_c = E_{c,(n+1)T} - E_{c,nT} . \tag{7}$$

Substitute (6), (7) into (2), we obtain

$$E_{c,(n+1)T} = K_S \cdot E_{c,nT} + \frac{1}{1 + T/RC} \Delta E_{in} . \tag{8}$$

Substitute (5) into (8), we can build EBM of boost converter

$$E_{c,(n+1)T} = K_S E_{c,nT} + A d_n{}^2 , \tag{9}$$

where $K_S = \dfrac{1-T/RC}{1+T/RC}$, $A = \dfrac{1}{1+T/RC}\dfrac{U_{in}{}^2T^2}{2L}\dfrac{U_{ref}}{U_{ref}-U_{in}}$.

As shown in Figure 1, the duty cycle d_n in the nth period is

$$d_n = D_S - K(u_n - U_{ref}), \tag{10}$$

where D_s is steady duty cycle, u_n is sampling value of output voltage at the nth period.

After the converter enters into steady state, the closed-loop system should satisfy

$$E_{c,(n+1)T} = E_{c,nT} = \frac{1}{2}CU_{ref}{}^2 = E_{ref}. \tag{11}$$

From (9) and (11), the steady duty cycle expression is

$$D_S = \sqrt{\frac{1-K_S}{A}E_{ref}}. \tag{12}$$

For actual converter, d_n should satisfy the following expression

$$d_n = \begin{cases} 0; D_S - K(u_n - U_{ref}) < 0 \\ D_S - K(u_n - U_{ref}); 0 < D_S - K(u_n - U_{ref}) < 1 \\ 1; D_S - K(u_n - U_{ref}) > 1 \end{cases}. \tag{13}$$

3 Results and Discussions

3.1 Diagrams of Storage Energy in Capacitor

Based on (9) and (13),we can depict the sequence diagram of capacitor energy for boost converter operated in period 2 as shown in Figure 3. The circuit parameters is

$$t = 333.3\mu s, U_{in} = 16V, U_{ref} = 25V, L = 208\mu H, C = 222\mu F, R = 12.5\Omega$$

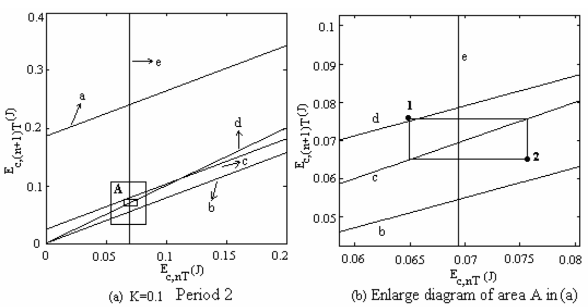

Figure 3. Energy locus of capacitor in period 2

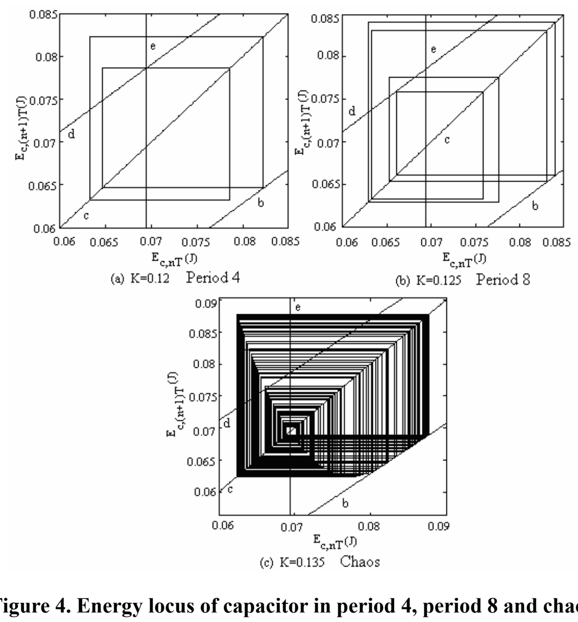

Figure 4. Energy locus of capacitor in period 4, period 8 and chaos

The storage energy in other period oscillation is shown in Figure 4. The lines appeared in Figure 3 and Figure 4 defined as follows.

Substitute $d_n = 1$ into (9) ，we can write

$$E_{c,(n+1)T} = K_S E_{c,nT} + A \tag{14}$$

Therefore, line a is depicted from the above expression.

Likewise, substitute $d_n = 0$ into (9), we obtain

$$E_{c,(n+1)T} = K_S E_{c,nT} \tag{15}$$

The line b is depicted from (15).

Line a and line b are two parallel lines and show storage energy state in capacitor under two utmost conditions. For actual converter, duty cycle is limited and the energy locus is also limited between a and b If the energy locus touch with line b ,it shows that the duty cycle of corresponding control pulse is zero, i.e., power switch has being turned-off.

When storage energy in capacitor is in equilibrium, the equation is expressed as the following

$$E_{c,(n+1)T} = E_{c,nT}. \tag{16}$$

Line c is depicted from (16).

In CCM and critical mode, $d_n + d'_n = 1$, and in DCM, $d_n + d'_n < 1$.

From (4), we obtain the duty cycle of converter operating in critical mode.

$$d_{nc} = \frac{U_{ref} - U_{in}}{U_{ref}} \tag{17}$$

So, the storage energy in capacitor can be depicted as line d. The corresponding equation can be written as

$$E_{c,(n+1)T} = K_S E_{c,nT} + A(\frac{U_{ref} - U_{in}}{U_{ref}})^2 . \tag{18}$$

It is obvious that the converter will enter into CCM while energy locus lies above line d, and DCM while energy locus lies below line d.

Line e denotes reference energy, the equation is

$$E_{ref} = \frac{1}{2} C U_{ref}{}^2 . \tag{19}$$

Figure 3(b) is the enlarge diagram of energy locus in period 2. As shown in Figure 3(b), energy state transforms between dot 1 and dot 2 while dot 1 lies in the left upper part of line d and dot 2 lies in the right lower part of line d. This means that inductor current on dot 1 works in CCM, and inductor current on dot 2 works in DCM. Because there is no intersection between energy locus and line b, it indicates that there are no skipped cycles in period 2 oscillation.

For the other periodic oscillation behavior, the operation characteristics of converter are comprehended by the energy locus diagrams as shown in Figure 4. For example, the operation characteristics in period 4 are described as follows. Inductor current is continuous in the first switching period; and discontinuous in the second switching period accompanying with skipped cycles. Furthermore, inductor current returns to be continuous in the third switching period; and discontinuous without skipped cycles in the fourth switching period. Such switching sequences make output voltage transform among four values. The same conclusion will be obtained by analyzing other energy locus in Figure 4(a) and Figure 4(b). However, from Figure 4(c) we can find that energy locus is much complex and has many intersections with line b. Meanwhile, many energy states lie on the top of line d. It shows that the corresponding control pulses sequences is very complex. The output of converter has entered into chaos. .

In general, we can acquire much operation information of converter from the diagram of capacitor energy locus. The energy locus of capacitor moves around the reference energy (line e). Therefore, the corresponding output voltage u_0 is fluctuating at U_{ref}. The energy states on the top of line d shows that converter operates in CCM and the energy states at the bottom of line d shows that converter operates in DCM. The points where energy locus intersects with line b indicate that converter operates with skipped cycles.

3.2 Bifurcation Diagrams

As shown in Figure 5, the bifurcation diagram of the capacitor energy is derived from (9) and (13) when the feedback gain constant k of error voltage amplifier is varying. It is obvious that the capacitor energy exhibit the route from period-doubling to chaos by increasing k.

Assume that the converter is in steady state. $0 < d_n < 1$.

Substituting $d_n = D_s - K(u_n - U_{ref})$ into (9) and using the following expressions

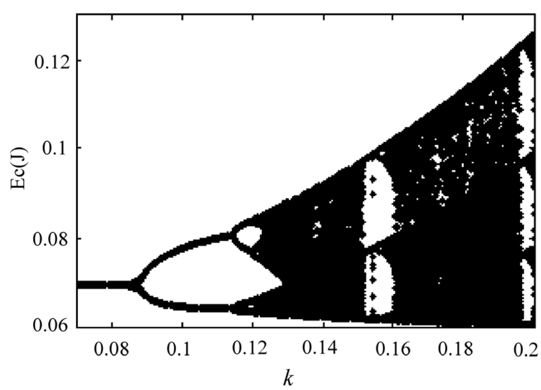

Figure 5. Bifurcation diagram of capacitor storage energy

$$u_n = \sqrt{\frac{2E_{c,nT}}{C}}, \quad \textbf{(20)}$$

$$U_{ref} = \sqrt{\frac{2E_{ref}}{C}}. \quad \textbf{(21)}$$

We can write

$$E_{c,(n+1)T} = K_S E_{c,nT} + A[D_S - K(\sqrt{\frac{2E_{c,nT}}{C}} - \sqrt{\frac{2E_{ref}}{C}})]^2. \quad \textbf{(22)}$$

It is obvious that (22) can be expanded with Taylor's series at the equilibrium point $E_{c,nTQ} = E_{ref}$. If high-level items of Taylor's series are neglected, the equation can be written as

$$\Delta E_{c,(n+1)T} = \lambda \cdot \Delta E_{c.nT} \quad \textbf{(23)}$$

where $\lambda = \frac{\partial E_{c,(n+1)T}}{\partial E_{c,nT}}\Big|_{E_{c,nTQ}=E_{ref}} = K_S - \frac{2AD_S K}{\sqrt{2CE_{ref}}}$.

In the range of small signals, λ can determine system stability. When $-1 < \lambda < 1$, system will be steady. The position of the first bifurcation point can be obtained at $\lambda = -1$.

$$K_c = (1+K_S)\frac{\sqrt{2CE_{ref}}}{2AD_S} = 0.09865 \quad \textbf{(24)}$$

Bifurcation diagrams of output voltage simulated by three models are shown as Figure 6. The diagram of Figure 6(a) is depicted by iterative 500 times of linear equation with every *K*. Figure 6(b) is derived from stroboscopic map model [4]. Figure 6(c) is the bifurcation diagram derived from EBM. Comparing three diagrams, the routes from bifurcation to chaos are similar. But the accurate positions of the first bifurcation point and output voltage are different. As shown in Figure 4, the bifurcation diagram in Figure 4(c) is closer to bifurcation diagram in Figure 4(a). Therefore, EBM has high accuracy in analyzing bifurcation and chaos phenomena.

Based on the above analysis, EBM still belongs to classification of stroboscopic map model although each modeling method is different. The disadvantage of EBM

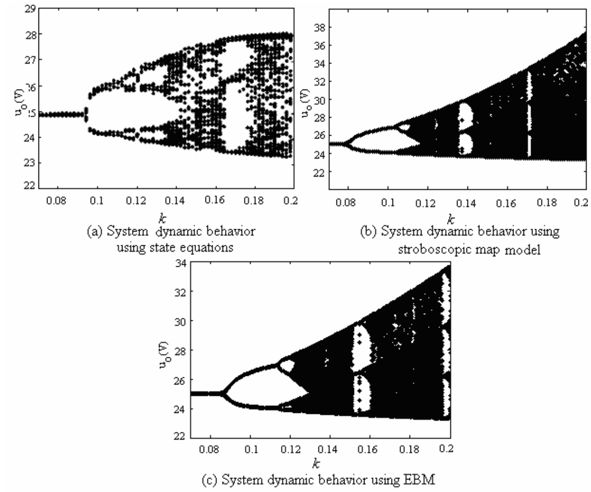

Figure 6. Bifurcation diagrams of output voltage simulated by three models

is that it can not analyze multiple pulses phenomena in one switching cycle. However, multiple pulses phenomena can be eliminated by a trigger which is added to PWM modulator (see Figure 1). Therefore, EBM is a unified model in analyzing nonlinear phenomena of converter.

4 The Reason for Bifurcation and Chaos in Converters Based on Energy Balance Viewpoint

The mechanisms of bifurcation and chaos are so complex that there is not an unified criterion to identify them. The types of bifurcations are various, e.g., period-doubling bifurcation, saddle-node bifurcation, fork bifurcation, Hopf bifurcation and border collision bifurcation [5]. In particular, border collision bifurcation usually appears in piecewise smooth system. For normal bifurcation, the mechanism of bifurcation accords with bifurcation theory, i.e., bifurcation happens when eigenvalues of Jacobin matrix of switching map model traverse unit circle. Furthermore, bifurcation styles can be distinguished from traverse direction. However, border collision bifurcation can not be verified by eigenvalues. Border collision bifurcation will happen if some points on periodic orbits collide with the boundary. Many research results show that saturation of duty cycle in power converters results in border collision bifurcation.

The general method for studying mechanisms of bifurcation is to seek breakthrough in state space. As shown in Figure 5, energy state of capacitor also exhibits bifurcation and chaos. Therefore, this paper firstly presents the mechanisms of bifurcation and chaos from energy balance viewpoint. From (9), we conclude that the present energy state is defined by former energy state and duty cycle. When duty cycle keeps steady, capacitor energy can keep balance in every switching period. But this is not the case. When capacitor energy can not keep balance in every switching period, switching time will increase to two switching cycles, four switching cycles, et al. Therefore, period 2 and period 4 bifurcations will happen. In general, imbalance of capacitor energy in one switching cycle results in bifurcation and chaos.

5 Conclusions

EBM still belongs to stroboscopic map model. But it has more accurate than stroboscopic map model. Comparing to iterative map model, the physical significance of EBM is more distinct. From energy locus diagrams, we can achieve abundant information about converters. Because energy balance theorem is universal rules in the world, EBM can be generalized to study the others nonlinear power converter as a unified model.

REFERENCES

[1] Middlebrook R D and Cuk S, “A general unified approach to modeling switching-converter power stage,” IEEE Power Electron. Spec. Conf. Rec., pp. 18-34, 1976

[2] Mario di Bernardo and Francesco Vasca, “Discrete-time for the analysis of bifurcations and chaos in DC/DC converters,” IEEE Transactions on Circuit System Ⅰ, Vol. 47, No. 2, pp. 130-143, 2000.

[3] Ma Xikui, Li Ming, Dai Dong, ZhaoHao, et al., “Reviews of research on complex behavior of power electronic circuits and systems,” Transactions of China Electrotechnical Society, Vol. 21, No. 12, pp. 1-11, 2006.

[4] C. K. Tse, “Flip bifurcation and chaos in the three-state boost switching regulators,” IEEE Transactions on Circuit System Ⅰ, Vol. No. 1, pp. 16-23, 1994.

[5] C. K. Tse, Y. M. Lai, and H. H. C. Iu, “Hopf bifurcation and chaos in a free-running current-controlled Cuk switching regulator,” IEEE Transactions on Circuit System Ⅰ, Vol. 47, No. 4, pp. 448-457, 2000.

[6] Guohui Yuan, Soumitro Banerjee, Edward Ott, et al., “Border-collision bifurcations in the buck converter,” IEEE Transactions on Circuit System Ⅰ, Vol. 45, No. 7, pp. 707-716, 1998.

[7] H. H. C. Iu and C. K. Tse, “Bifurcation behavior in parallel-connected buck converters,” IEEE Transactions on Circuit System Ⅰ, Vol. 48, No. 2, pp. 233-240, 2001.

[8] Zhang Bo, Li Ping, and Qi Qun, “Method for analyzing and modeling bifurcation and chaos in DC/DC converters,” Peoceedings of CSEE, Vol. 22, No. 11, pp. 81-86, 2002.

[9] Liu Weizeng, Zhang Hao, and Ma Xikui, “Analysis of intermittent bifurcations and chaos phenomena in boost PFC converters bystroboscopic map,” Proceedings of CSEE, Vol. 25, No. 1, pp. 43-48, 2005.

[10] Qu Ying and Zhang Bo, “The precise mathematical discrete model of buck converter in DCM and its analysis for bifurcation stability,” Acta Electronica Sinica, Vol. 30, No. 8, pp. 1253-1256, 2002

[11] Ma Xikui, Liu Weizeng, and Zhang Hao, “Analysis of fast-scale bifurcations and chaos phenomena in boost PFC converter,” Proceedings of CSEE, Vol. 25, No. 5, pp. 61-67, 2005.

Energy and Power Engineering, **2009, 44-49**
doi:10.4236/epe.2009.11007 Published Online August 2009 (http://www.scirp.org/journal/epe)

Study of the Law about Water-Cut Variation for the Fractured Metamorphic Reservoir of Buried Hill with Bottom Water

——A Case study at Budate Reservoir in Beir Depression, Hailar Basin

Shenggao QIN [1], Yanling SUN [2], Zhenqi JIA [1], Dagang YANG [1]
[1] *Key Laboratory of Enhanced Oil and Gas Recovery of Education Ministry, Daqing Petroleum Institute, Daqing, China*
[2] *Information Center of No.1 Oil Recovery Company, Daqing Oilfield Co. Ltd., Daqing, China*

Abstract: Aiming at the complex flowing environment including the buried hill of Metamorphite, the active bottom water and the fracture at Budate Reservoir within Beir Depression of the Hailar Basin, combining the laboratory studies and based on analysis of its drive mechanism, field wells' parameters were used to analyze the effects of different conditions of the fractured metamorphic reservoir with bottom water on its law of water-cut variation and the waterflooding efficiency. The results show that for the Budate buried hill reservoir with bottom water, the gravity should be taken into consideration to determine reasonable perforation ratio and production pressure difference. And because of the acid sensitivity of the buried hill reservoir, application of proper clay stabilizer will enhance the field oil recovery to a satisfactory extent.

Keywords: metamorphic reservoir, bottom water, buried hill reservoir, water-cut

1 Introduction

Currently majority of the discovered buried hill reservoirs home and abroad belong to the type of carbonate reservoir [1][2], in which there are complex types of pore canals always including solution crevice, fracture and so on. Thereby the fluid flowing inside shows the unique features. Many scholars home and abroad have made progressive advance in this area with the reservoir engineering method, numerical simulation and others [3-5]. However, Budate Reservoir in the Beir depression of the Hailar Basin is the buried hill reservoir with bottom water, where it is very complicated of the fluid flowing laws that have not been reported academically. So it is a new topic to perform the study of the law of fluid flowing in this kind of reservoir and the fruits acquired will have positive reference value for the same kind of reservoirs.

2 Reservoir Features of Budate Buried Hill

Budate Reservoir lies in the bottom of the Hailar sedimentary basin. It developed from the Trias and was composed mainly of the carbon siltpelite, a slightly metamorphite and the unequigranular feldspar rock-fragment sandstone. Due to the dissection of many faults, each faulted-block is a buried hill reservoir with its independent oil-water interface.

Budate Reservoir has geological reserve about 1811×10^4t, but very poor physical properties such as the average effective porosity of 5.3%, the average gas permeability of $0.14\times10^{-3}\mu m^2$ and water-sensitivity coefficient of 0.64 which shows a bit strong water sensitivity. The fractures developed plus the pores make the formation a fracture-pore reservoir.

3 Drive Mechanism of the Buried Hill Reservoir

3.1 Principle of Bottom Water Coning

Because of the active energy of bottom water, when an oil well produces at a certain rate after perforation of an oil well, a pressure drop funnel would form at the bottom

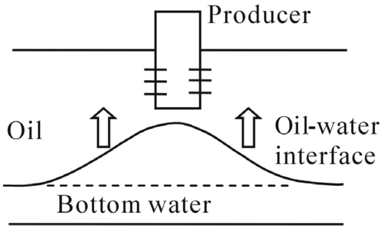

Figure 1. Schematic of the water core

of the well (see in Figure 1). The original horizontal oil-water interface before production transforms to the shape of a core under the well by the oil-water potential gradient. If the well produces at a certain stable rate the formed water core would stay at an certain altitude; if the production rate increases the core altitude grows until the bottom water flows into the oil well which would produce water.

By the difference of the core's advance speed there are two types of bottom water drive: lifting and coning. Lifting denotes that in the process of bottom water displacement, the front edge of the displacing water (oil-water interface) move upwards slowly, smoothly in a big area; while coning indicates the displacing bottom water rushes into oil wells along local zones of high permeability. So lifting is favorable for oil displacement by bottom water with good oil displacement efficiency, long anhydrous production period and high ultimate field recovery; while coning which happens always near wellbores, would results in quick water breakthrough, short anhydrous production period and low ultimate field recovery. The flooding pattern of bottom water is dependent on two types of factors. One type corresponds to factors such as the geological features of the reservoir, the relationship between oil layers and water layers, interlayers' development and distribution, physical properties of the subsurface oil and water and so on, and the other corresponds to man-made development program, perforation positions and ratio, production rate and so on.

Hence, it is a key technological problem to control the bottom water coning in the development process of this kind of reservoirs. For the field, to control coning of the bottom water to extend the anhydrous production period a reasonable production rate should be adopted; for a single well the output should not overcome a special number which is called critical yield. Finally the detailed regulatory measures for the yield, production pressure difference and the perforation ratio should be used to control the bottom water coning. And to control the yield should be realized by the variables as perforation ratio and production pressure difference, which are the major measures to control bottom water coning to displace the overall reservoir upwards in the type of lifting.

Because the displacement energy source underlies the oil reservoir, at the oil-water interface below, the bottom water should firstly overcome the gravity itself then to displace crude oil bottom-up. In this process the action of gravity should be taken into consideration.

3.2 Mathematical Model of the Water-Cut Variation

In the development program of bottom water reservoir, perforation is always done at the top of the reservoir to avoid early water breakthrough. In contrast with the total reservoir thickness, the fluid flowing in the porous media could be presumed as the combination of the horizontal flowing at the top layers perforated and the vertical flowing in the sub-layers [7][8]. Hen the equation about the water-cut variation could be derived as following:

$$f_w = \frac{Q_w}{Q_o + Q_w} = \frac{\dfrac{K_{rw}}{\mu_w}}{\dfrac{K_{rw}}{\mu_w} + \beta^{'} \dfrac{K_{ro}}{\mu_o}} \tag{1}$$

$$\beta^{'} = 1 + \frac{\left(\gamma_w - \gamma_o\right)H}{\dfrac{25\Delta p}{\ln \dfrac{R_e}{R_w} - 0.5} - \left(\gamma_w - \alpha^{'}\right)H} \tag{2}$$

4 Analysis of Law on Water-Cut Variation at Budate Buried Hill Reservoir

Now take well D112-227, D108-229 and B28-1 as examples for Budate Reservoir to appraise the laws of water variation with different parameters that are listed at Table 1.

Table 1. Parameters from three wells of Budate Reservoir

Well	μ_w(mPa.s)	μ_o(mPa.s)	γ_w	γ_o	h(m)	H(m)	x	Re(m)	Rw(m)	α
D112-227	0.65	4.68	1	0.7761	176	155	0.1193	300	0.1	0.97
D108-229	0.65	4.32	1	0.745	110.4	95.6	0.1341	300	0.1	0.97
B28-1	0.65	4.32	1	0.745	64	8.4	0.8688	300	0.1	0.97

4.1 Effects of Reservoir Thickness, Perforation Ratio and Production Pressure Difference on Water-Cut Curves

Considering strong water sensitivity of the Beir Depression, in the lab three groups of relative permeability curves were measured as in Figure 2, one displacing fluid is water, the others are two kinds of clay stabilizer solutions(CS-05 and CS-07).

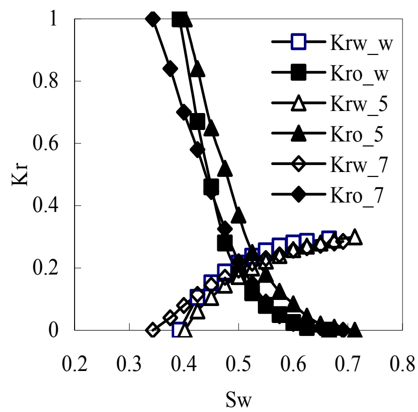

Figure 2. Relative permeability curves measured by different displacing agent

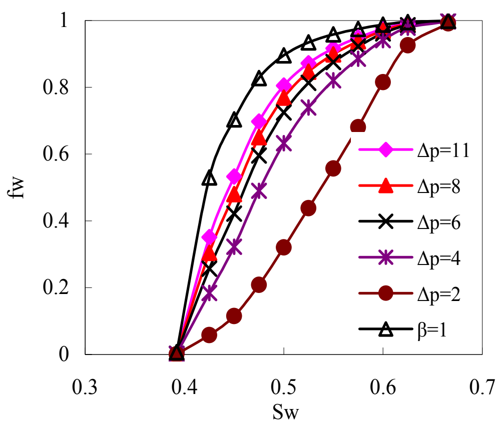

Figure 3. Water-cut curves versus production pressure difference (D112-227)

The Water-cut Variation curves under several production pressure differences are shown in Figure 3 for well D112-227. We could recognize that at the Block-faulted reservoir of buried hill with bottom water, the gravity would have great influence on the law of Water-cut Variation as:

1) If gravity unconsidered (β=1), the calculated water-cut will increase more quickly than that in the case of gravity considered along with the change of water saturation. That's if gravity considered, during early period of low water saturation, the curves are steeper with slower rate of oil production and less oil recovery; during the later period of high water saturation, more oil can be produced and the residual oil retained by water displacement should be developed by the tertiary oil recovery technologies.

2) If gravity considered, the water-cut increases along the rise of water saturation slowly. This phenomenon could be explained that the gravity of the bottom water itself that are displacing oil upwards decreases the water breakthrough or fingering, so as to slow the rising velocity of water-cut.

3) If gravity considered, the sizes of production pressure differences have obvious influence on the law of Water-cut Variation. The less production pressure difference, the slower rising velocity of water-cut along with the increase of water saturation, so is its reduced extent. This phenomenon could be explained that the action of gravity becomes less along with the increase of production pressure differences and at a certain big value of production pressure differences the action of gravity could be neglected.

For well D108-229 the Water-cut Variation curves under several production pressure differences are shown in Figure 4 which shows same law as discussed above.

For well B28-1 the Water-cut Variation curves under several production pressure differences are shown in Figure 3. From table 1 while other parameters are nearly the same, the perforation ratios for well D112-227, D108-229 and B28-1 are x=0.1193, x=0.1341 and x=0.8688, respectively. Such conclusions could be drawn as:

1) Along with the increase of perforation ratio, the effect of gravity on reducing the rising velocity of water-cut becomes less. This case will be the nearly the same as that while gravity unconsidered.

2) Along with the increase of perforation ratio, the effect of production pressure difference on the increase of water-cut becomes less, even disappears.

When the oil layers are completely perforated, that's x=1, the fluid in the whole reservoir flows in the radial direction. Then the bottom water will drive the oil at the least efficiency and its energy will make the oil well drought.

Such laws discussed above are in accordance with the actual development cases for block-faulted reservoir with bottom water.

4.2 Effect of the Clay Stabilizers

The water sensitivity index of the core samples from Budate Reservoir fall into the range of 0.60～0.67 (a bit strong water sensitivity). Besides the oil and water relative permeability curve measured, in the lab other two relative permeability curves were also measured with clay stabilizer CS-5 and CS-7 (see in Table 2). Then the effects of clay stabilizers on relative permeability curves and on the law of Water-cut Variation are analyzed to provide reference for the optimization of clay stabilizers at Budate Reservoir.

Based on the parameters from well D108-229 (see in Table 1), three curves of Water-cut Variation of water, CS-5 and CS-7 are shown in Figure 5 for gravity unconsidered and in Figure 6 for gravity considered in Figure 7.

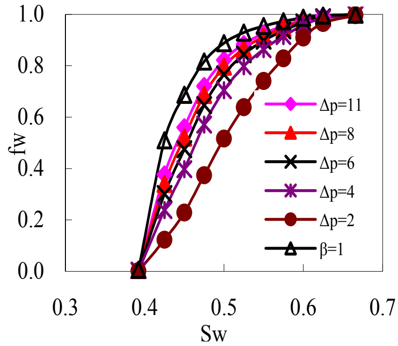

Figure 4. Water-cut curves versus production pressure differences (D108-229)

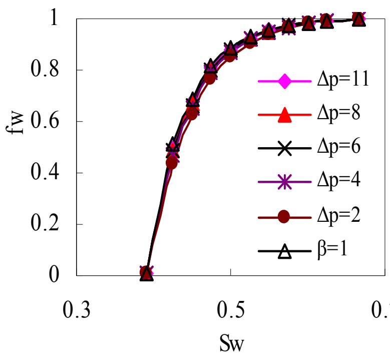

Figure 5. Water-cut curves versus production pressure differences (B28-1)

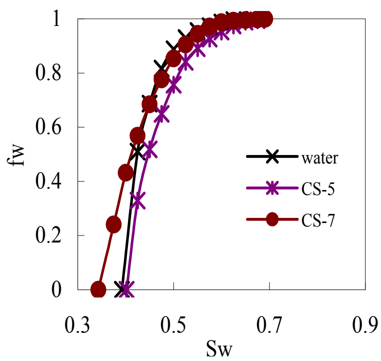

Figure 6. Water-cut curves versus different clay stabilizers (gravity unconsidered)

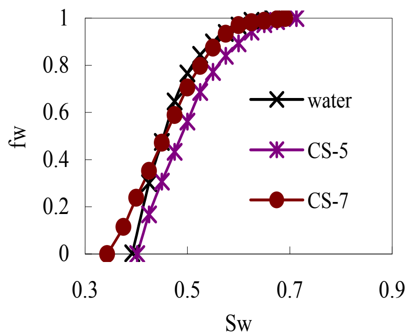

Figure 7. Water-cut curves versus different clay stabilizers (gravity considered)

Table 2. Feature values of relative permeability curves measured at lab

Core No.	K_g ($10^{-3}\mu m^2$)	ϕ (%)	S_{wi} (%)	S_{or} (%)	Krw at Sor (%)	Anhydrous Recovery (%)	Ultimate Recovery (%)	Range of oil-water phases (%)	S_w at point of two curves's intersection (%)	Clay stabilizer
C166-1	119.21	23.19	39.21	33.43	29.30	18.31	45.01	27.36	49.20	水
C166-2	114.01	22.92	40.17	28.72	30.00	25.71	52.00	31.11	53.80	5
C166-4	186.56	23.05	34.30	30.88	28.50	32.47	53.00	34.82	50.75	7

Conclusions could be drawn as:

1) Using clay stabilizers can reduce the rising velocity of water-cut at the stage of low water saturation, that's oilfield can recovery more oil at the stage of low water saturation than that in the case of water flooding.

2) Using clay stabilizer CS-5 makes the point of water breakthrough later than that the case of water flooding.

3) Using clay stabilizer CS-7 makes the rising velocity of water-cut smooth and makes the oil recovery at the low water saturation the biggest number but with earlier point of water breakthrough.

4) Using clay stabilizers makes the flowing range of two phases wider. The anhydrous oil recovery efficiency and the ultimate number both obviously larger than that of the case of water flooding.

5 Conclusions

1) Gravity has great influence on the law of Water-cut Variation for the Block-faulted reservoir of buried hill with bottom water: if gravity considered, the water-cut increases along with the rise of water saturation slowly at the stage of low water saturation. The less production pressure difference, the slower rising velocity of water-cut along with the increase of water saturation, so is its reduced extent. At a certain big value of production pressure differences the action of gravity could be neglected.

2) Both the perforation ratio and the production pressure difference have great influence on the law of Water-cut Variation for the Block-faulted reservoir of buried hill with bottom water. Along with the increase of perforation ratio, the effect of gravity on reducing the rising velocity of water-cut becomes less. This water-cut curve will be the nearly the same as that while gravity unconsidered. Along with the increase of perforation ratio, the effect of production pressure difference on the increase of water-cut becomes less, even disappears.

3) Clay stabilizers can reduce the rising velocity of water-cut at the stage of low water saturation and make the anhydrous oil recovery efficiency and the ultimate number both obviously larger than that of the case of water flooding.

6 Nomenclature

K_{rw} — relative permeability water, dimensionless;
K_{ro} — relative permeability oil, dimensionless;
μ_w — water viscosity, mPa•s;
μ_o — oil viscosity, mPa•s, mPa•s;
γ_w — relative density of water, dimensionless;
γ_o — relative density of oil, dimensionless;
H — thickness to avoid water in a oil well, m;
α' — Reservoir pressure coefficient, dimensionless;
R_e — well spacing, m;
R_w — wellbore radius, m;
S_w — water saturation;
K_g — gas permeability, $10^{-3}\mu m^2$;
φ — porosity, dimensionless;
S_{wi} — irreducible water saturation, dimensionless;
S_{or} — residual oil saturation, dimensionless.

REFERENCES

[1] BO Song-zhang, "Development of carbonate buried hill reservoir," Petroleum Industry Press, Beijing, Vol. 5, pp.2-8, 1996.

[2] S. Ullah, Tse Yone Shen, S. A. Mobarak, et al., "Development feasibility study: Dongshengpu buried hill reservoir," SPE 17577, Vol. 11, pp. 273-284, 1988.

[3] M. G. Starcher, J. R. Murphy, P. D. Alexander, et al., "Video camera log used for water isolation in the main body 'B' pool, Elk hills field, Kern Co., California-water and oil identification," SPE29654, Vol. 3, pp. 384-394, 1995.

[4] K. A. Edwards, B. Anderson, and B. Reavie, "Horizontal injectors rejuvenate mature miscible flood-south swan hills field," SPE77302, Vol. 2, pp.174-182, 2002.

[5] CHEN Shao-sheng, XU Kun, Han Yun, et al., "Study on characteristics and development law of fractured basement reservoirs: A case study of fractured basement reservoirs in Damintun depression of Liaohe basin," SPE80541, Vol. 4, pp. 1-9, 2003.

[6] ZHANG Ji-guang, WANG Jin-kui, QIN Long-pu, et al., "Characteristics of metamorphic buried hill reservoir in Sude'erte of Beir fault depression in Hailar basin," ACTA PETROLEI SINIC, Vol. 28, No. 4, pp. 21-30, 2007.

[7] LU Ai-min andYAO Jun, "Change of water cut and oil production in fractured reservoir with bottom water," Special Oil and Gas Reservoir, Vol. 13, No. 5, pp. 56-61, 2006.

[8] LU Ai-min and YAO Jun, "Rational perforating level and well spacing for fractured carbonate reservoirs with bottom water," Vol. 35, No. 1, pp. 97-100, 2008.

Energy and Power Engineering, **2009, 50-53**
doi:10.4236/epe.2009.11008 Published Online August 2009 (http://www.scirp.org/journal/epe)

Scientific Research

The Research of Anti-Swelling and Low Damage Killing Fluid System

Qinggong DANG, Hui JIA, Shuang SUN, Meng LI, Zhenqi JIA
College of Petroleum Engineering, Daqing Petroleum Institute, Daqing, China
Email: dangqg@sina.com

Abstract: In this paper, we introduced reservoir characteristics in Block Xiao-he-long and evaluate the performance of the existing killing fluid system. According to the production requirements, a anti-swelling and low damaging system of chemical agents suitable for this block was optimized, including anti-swelling agent, water lock inhibitor, fluid-loss agent additives, plus a corrosion inhibitor HS-1 developed by in the lab. The system is composed by base liquid (0.7%X + 2.0%KCl +0.05%SY-1+ 0.05%HS-1+2.0% DST-1 dissolved in water) and weighting material (NaCl) with its density adjustable range between 1.0g/ml and 1.2g/ml. Its anti-swelling ratio achieves 53.80%, and the reservoir permeability recovery ratio reaches more than 95.0%.

Keywords: killing fluid, fomula, reservoir protect, low permeability

1 Reservoir Characteristics

Information shows that gas is produced mainly in sections of Quantou1 (Q1) and Quantou3 (Q3) at Block Xiao-he-long. The formations are composed of mudstone, sandy mudstone, siltstone and gravel rough rock with higher clay content, generally, more than 95.0%. In addition, the layer also contains a certain amount of Fe-Al minerals and carbonate minerals. Sections of Q1 and Q3 are high in salinity, of which the average number is 17098.4mg/l, maximum number up to 23216.5mg/l, minimum value by 122.43.3mg/l. The formation water is a kind of kalescent fluid of $NaHCO_3$, of which the Ph values are between 7.0 and 8.5 with the average value by 7.6. Studies show that this block has poor reservoir properties. The injected fluid such as water, acid or alkaline liquid would give rise to the sensitivity reaction easily to cause serious damage to the reservoir.

The average pressure coefficients of Sections of Q1 and Q3 fall between 0.995 and 1.05 while the average temperature gradients are between 4.21 and 4.75℃ per 100m. So they are systems with normal pressure and temperature. Based on the requirements of well control management, killing fluid density should be equal to the value of pressure coefficient plus 0.07-0.15. Therefore, the killing fluid density can meet the production requirements of Block Xiao-he-long when the density are between 1.065 and 1.20g/ml.

2 Existing Killing Fluid Performance

Here we evaluated the conventional performance of three killing f©luids (Density, Viscosity, Ph value, fluid loss volume and stability performance) which are used at the Block Xiao-he-long. The results are presented in Table 1.

Table 1. Results of evaluation existing killing fluid performance

Killing fluid code	Density (g/cm^3)	Viscosity (mPa·s)	Ph	Fluid-loss volume(ml)	Stability performance	Reservoir damage ratio %	
						Q1	Q3
1#	1.23	75.0	11	serious	well	88.51	96.97
2#	1.01	37.5	7	＞50	well	92.86	97.95
3#	1.19	14.5	8	＞50	well	76.62	83.16

We can see from Table 1 that the existing killing fluids have good index as stability performance, density and viscosity to meet the operational requirements. But the fluid-loss volumes are too big as the fluid damage rate of the three killing fluids are more than 75% and the value of 2# is as high as 97.95%. It no longer satisfies the requirements of the oil and gas reservoir protection.

3 Development of the Killing Fluid System of Anti-Swelling with Low Damage

Based on the reservoir characteristics of Block Xiao-he-long, a number of anti-swelling agents, water lock inhibitors, corrosion inhibitors and fluid-loss agents and several additives are studied and optimized.

3.1 Research of Anti-Swelling System

In this section, we used dilatometer NP-1 to study the anti-swelling effect of KCl and small cation X, and to determine the anti-swelling system suitable for Block Xiao-he-long. The results are presented in Table 2.

Experimental results show that anti-swelling effect increases with the increment of KCl and X. When the amounts of X and KCl reach 0.7% and 2.0%, respectively, there will be a good anti-swelling effect with the anti-swelling ratio by 53.80%.

3.2 Screening Water Lock Inhibitor

In order to avoid the water lock effect, a few of water lock inhibitor need to be added to the killing fluid. SY-1 and SY-2 have excellent ability to inhibit the water lock effect. Effects of the base liquid with 0.7%A and 2.0%KCl on the ratio of reservoir damage are shown in Table 3.

Table 2. The experimental results of anti-swelling system

anti-swelling agents and the dosages	X (0.5%) KCl (1.2%)	X (0.7%) KCl (1.2%)	X (0.5%) KCl (2.0%)	X (0.7%) KCl (2.0%)
Swelling extent (mm) 24h	1.31	1.24	1.18	1.11
Ratio (%)	5.82	5.51	5.24	4.93
Anti-swelling ratio (%)	45.45	48.36	50.89	53.80

Table 3. The effect of water lock inhibiter on reservoir damage ratio

Water lock inhibiter	Amount (%)	Reservoir damage ratio (%)
SY-1	0.05	9.70
SY-2	0.05	20.49

Table 4. Experimental results of the HS-1 anti-corrosion ability

Amount of HS-1 (%)	Temperature (℃)	Corrosion rate (mm/d)
0.00	80.0	1.089
0.05	80.0	0.051

Table 3 shows that the water lock inhibitor added to the killing fluid can reduce the reservoir damage ratio. SY-1, which is better than SY-2, could reduced damage ratio to 9.70%. Therefore, we choose SY-1 for this system to control water lock.

3.3 Corrosion Inhibitor HS-1

In order to slow down the corrosion rate of the tubing and casing, we developed the corrosion inhibitor HS-1 for this killing fluid system. Table 4 is the experimental results of the HS-1 anti-corrosion ability.

Experimental results shown that a certain amount of HS-1 to the killing fluid can reduce the corrosion rate in comparison with the pre-accession. Thus we know that

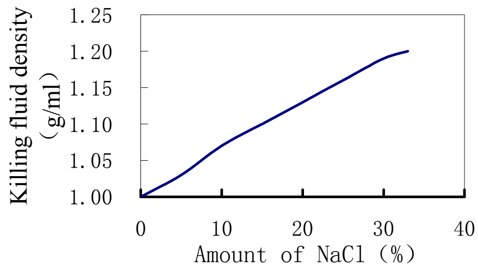

Figure 1. Relationship between the amount of NaCl and killing fluid density

HS-1 has good corrosion inhibition ability.

3.4 Density Adjustment

Block Xiao-he-long was buried shallow and has low formation pressure, so NaCl is used to adjust the density of the killing fluid to meet the requirements of killing well. Figure 1 shows the relationship between the correlation of the killing fluid density versus the amount of NaCl.

3.5 Screening Fluid-Loss Agent

We screen a variety of fluid-loss agent to reduce the fluid-loss volume. Finally, we selected SPN-1 and SPN-2 as the fluid-loss agent. And then, we studied the effects of mixed system and the individual agent. The results are presented in Table 6.

DST-1 (SPN-1: SPN-2 = 3:2) and DST-2 (SPN-1: SPN-2 = 1:1) were mixture of SPN-1 and SPN-2. Table 6 shown that system with both SPN-1 and SPN-2 is better than single one agent while DST-1 is the best with the least of fluid-loss volume of 5.0ml/min (API).

Both SPN-1 and SPN-2 can form polymeric membrane on rock surface to reduce the killing fluid fluid-loss volume. On the rock surface the mixture of SPN-1 and SPN-2 will form micellar of different size and shape which complement each other to form a more dense-permeable membrane to reduce the killing fluid loss. Therefore, DST-1 is chosen as the system fluid-loss agent.

Table 6. Results of screening fluid-loss agent

Fluid-loss agent	Amount (%)	Viscosity (mPa·s)	Density (g/cm^3)	Fluid-loss Volume (ml/API)
SPN-1	2.0	4.62	1.10	7.9
SPN-2	2.0	8.25	1.12	12.5
DST-1	2.0	5.80	1.10	5.0
DST-2	2.0	6.53	1.09	6.7

3.6 Summary

In sum of the above studies, we have obtained the anti-swelling and low damage killing fluid system suit able for Block Xiao-he-long. It is composed by base liquid (0.7%X+2.0%KCl+0.05%SY-1+0.05%HS-1+2.0% DST-1 dissolved in water) and weighting material (NaCl).

4 Evaluation of Anti-Swelling and Low Damage Killing Fluid

According to the formula in *F*, three configurations of different killing fluids are made as 4#, 5# and 6# which are evaluated in experiments. The results are shown in Table 7.

Table 7 shows that the anti-swelling and low damage killing fluid have good index as the stability performance, low viscosity, Ph value by 7.0. It will not give rise to acid and alkali damage. The fluid-loss volume is about

Table 7. Results of evaluation the performance of anti-swelling and low damage killing fluid

Killing fluid code	Density (g/cm^3)	Viscosity (mPa·s)	Ph	Fluid-loss volume (ml)	Stability performance	Reservoir damage ratio %	
						Q1	Q3
4#	1.02	5.76	7.0	4.5	Well	3.98	3.70
5#	1.11	5.78	7.0	5.5	Well	4.33	4.25
6#	1.20	5.80	7.0	7.0	Well	4.89	4.68

7.0 ml/30min. Its damage to the reservoir is low, and the reservoir permeability recovery is more than 95.0%.

5 Conclusions

1) A killing fluid system of anti-swelling and low damage is developed with its anti-swelling ratio up to 53.80%;

2) The anti-swelling and low damage killing fluid system have low fluid-loss volume by 7.0ml/30min (API) no matter how much killing fluid density. It can recovery the reservoir permeability value more than 95.0%;

3) A series of additives and their dosages are optimized for this anti-swelling and low damage killing fluid system. The system is composed by base liquid (0.7%X + 2.0%KCl +0.05%SY-1+ 0.05%HS-1+2.0% DST-1 dissolved in water) and weighting material (NaCl). It is better than existing killing fluids and can satisfy the requirements of oil and gas layer protection in Block Xiao-he-long.

REFERENCES

[1] SY/T5358-2002, "Formation damage evaluation by flow test," S.

[2] Fan Shizhong, "Oil and gas layer protection and evaluation," Petroleum Industry Press, Beijing, pp. 92-126, 1988.

[3] Xu Tongtai, Zhao min, and Xiong Youming, "Protection oil and gas layer technology," Oil Press, Beijing, pp. 49-55, 2003.

[4] Li Kexiang, "Oil and gas layer drilling and killing well technology," Petroleum Industry Press, pp. 796-815, Beijing, 1993.

Energy and Power Engineering, 2009, 54-64
doi:10.4236/epe.2009.11009 Published Online August 2009 (http://www.scirp.org/journal/epe)

Scientific Research

Optimal Scheduling Strategy for Energy Consumption Minimization of Hydro-Thermal Power Systems

Jiekang WU
School of Electrical Engineering, Guangxi University, Nanning, China
Email: *wujiekang@163.com*

Abstract: A comparison analysis based method for computing the water consumption volume needed for electric energy production of optimal scheduling in hydro-thermal power systems is presented in this paper. The electric energy produced by hydroelectric plants and coal-fired plants is divided into 4 components: potential energy, kinetic energy, water-deep pressure energy and reservoir energy. A new and important concept, reservoir energy, is proposed, based on which is divided into a number of water bodies, for example 3 water bodies, and a reservoir is analyzed in a new way. This paper presents an optimal scheduling solution of electric energy production of hydro-thermal power systems based on multi-factors analytic method, in which some important factors, such as load demand, reservoir in-flow, water consumption volume increment rate of hydroelectric plants or converted from coal-fired plants, and so on are given to model the objective function and the constraints. A study example with three simulation cases is carried out to illustrate flexibility, adaptability, applicability of the proposed method.

Keywords: hydro-thermal power systems, optimal electric energy production, water consumption volume

1 Introduction

Water is one of the important renewable energy sources and coal is a non-renewable energy source. For optimal scheduling of hydro-thermal power systems, it is the first thing that water must have much more priority to be used for electric energy production than coal so as to supply the demand load. It is an important study task how to minimize the sum of water consumption volume of the hydroelectric plant and water consumption volume converted from the coal-consumed volume of coal-fired plants in hydro-thermal power system dispatch.

In modeling electric energy production of hydroelectric plants, some pioneer did many significant works. For the portfolio management of a scandinavian power supplier, a linear stochastic model with hydraulic power plants under uncertain inflow and market price conditions is introduced [1]. In [2], price uncertainty by scenarios and a model for maximizing risk-adjusted profit within an asset-liability framework is represented. A new multi-loop-cascaded governor, with which the performance specifications and stability margins are improved significantly even in the presence of some uncertainties, is proposed to use for hydro turbine control [3] and some other stochastic programming models are proposed to represent the energy systems [4]. However, with the achievements in recent liberalization of the electricity market, the discussion about improving the assumptions and considering further aspects of actual system operations is far from ending.

Some works have done for the optimal scheduling solution of hydro-thermal power systems. There are many computational methods for the solution of some difficult optimization problem such as dynamic programming [5][6], network flow [7-9], standard mixed integer programming methods [10-12], and modern heuristic algorithms [13][14]. Although dynamic programming is flexible and can handle the constraints better in a straightforward way, the "curse of dimensionality" still remains, and the main drawback of using dynamic programming for a realistic systems with multiple reservoirs and cascaded hydro plants still exists [14]. Network flow would be the natural way to model hydro systems. Its main drawback, however, is its inability to deal with discontinuous operating regions and discrete operating states [15]. Mixed integer programming is only suitable for small systems due to size limitations. Modern heuristic algorithms do not require such conditions that the objective function has to be differentiable and continuous, so these methods are considered as effective tools for non- linear optimization problems such as short-term scheduling of hydro systems. Particle swarm optimization (PSO) is one of the modern heuristic algorithms. PSO has attracted great attention due to its features of easy implementation, robustness to control parameters and computation efficiency compared with other existing heuristic algorithms, and has been successfully applied to hydroelectric optimization scheduling problems [16-20]. Some stochastic approaches are also used for the solution of the cascaded hydro plants problem [21-22].

This paper presents a novel analysis method for modeling hydro-energy conversion and computing water consumption volume of optimal electric energy production in large-scale hydro-thermal power systems, taking some energy components, such as potential energy, kinetic energy, water-deep pressure energy and reservoir energy into consideration, and also taking some influence factors, such as load demand, reservoir in-flow, water consumption volume increment rate, and so on, into account.

2 Hydro-Energy Conversion

In a large-scale reservoir, if there is a hydro-mechanical-electric coupling system, with a shaft leading the reservoir water through penstock to a hydro turbine, the potential, kinetic and water-deep energy in water is harnessed by the HME coupling system and create electricity from it. For each HME system, the amount of electric energy transformed form hydro energy in reservoir depends on the forces applied on the water body in intake and tailrace of the pressure tunnel. In intake of the pressure tunnel, basing on the traditional analysis method, there is gravitational force corresponding to the potential energy, kinetic force corresponding to kinetic energy and pressure force corresponding to water-deep pressure energy.

In this paper, besides three traditional forces there are another three reservoir forces applied to the water body in intake if a reservoir is divided into three water bodies when modeling the hydroelectric energy of large-scale reservoir. These three reservoir forces applies to the water bode in intake of a pressure tunnel and do work in respective part, which is called 'reservoir energy' in this paper, as shown in Figure 1.

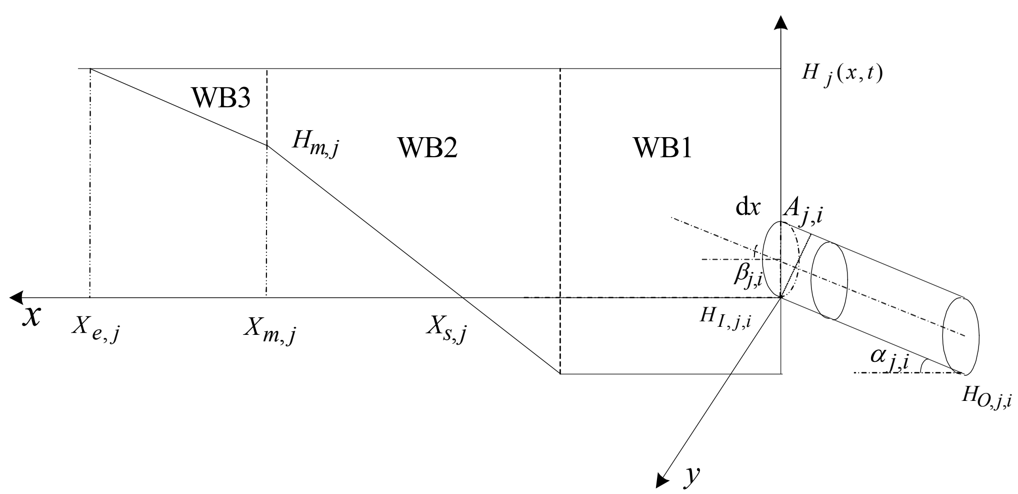

Figure 1. Divided water bodies of a large-scale reservoir

Because of difference in kinetic energy, potential energy, energy converted from water-deep pressure energy, the energy converted from self-weight, reservoir energy, there is a part of energy transformed into electric energy. For a unit i in plant j, the electric energy converted by a HME system in unit time(for example one second) may be expressed in a form of kilo-watt may be formulated in MWs:

$$E_{H,j,i}(H_j, Q_{G,j,i}) = f_1 + f_2 + f_3 + f_4 + f_5 + f_6 \quad \textbf{(1)}$$

where

$$f_1 = 9.81[(H_j(x,t) - H_{I,j,i}) - p_{O,j,i})]Q_{G,j,i} \quad \textbf{(2)}$$

$$f_2 = 9.81 * \frac{1}{2g}[v_{I,j,i}^2 - v_{O,j,i}^2]Q_{G,j,i} \quad \textbf{(3)}$$

$$f_3 = 9.81[H_{I,j,i} - H_{O,j,i}(t)]Q_{G,j,i} \quad \textbf{(4)}$$

$$f_4 = \frac{9.81 X_{s,j} Y_j [H_j(x,t) - H_{I,j,i}]}{Y_j [H_j(x,t) - H_{I,j,i}]} \cdot$$

$$\sin\beta_{s,j}\cos(\alpha_{I,j,i} - \beta_{s,j})\cos^2\gamma_{s,j,i} \cdot Q_{G,j,i} \quad \textbf{(5)}$$

$$f_5 = \frac{9.81 Y_j (X_{m,j} - X_{s,j})(2H_j(x,t) - H_{m,j} - H_{I,j,i})}{2Y_j[H_j(x,t) - H_{I,j,i}]} \cdot$$

$$\sin\beta_{m,j}\cos(\alpha_{I,j,i} - \beta_{m,j})\cos^2\gamma_{m,j,i} \cdot Q_{G,j,i} \quad \textbf{(6)}$$

$$f_6 = \frac{9.81 Y_j (X_{e,j} - X_{m,j})(H_j(x,t) - H_{m,j})}{3Y_j[H_j(x,t) - H_{I,j,i}]} \cdot$$

$$\sin\beta_{e,j}\cos(\alpha_{I,j,i} - \beta_{e,j})\cos^2\gamma_{e,j,i} \cdot Q_{G,j,i} \quad \textbf{(7)}$$

where f_1 is energy converted from water-deep pressure energy, f_2 is energy converted from kinetic energy, f_3 is energy converted from potential energy, f_4 - f_6 is energy converted from reservoir energy. $Q_{G,j,i}$ is generation flow of generator i in plant j, $\alpha_{j,i}$ is the angle of the pressure tunnel for each generating unit, $H_j(x,t)$ is water-storage level elevation in reservoir j at time t, $H_{I,j,i}$ is a position elevation of the intake of the pressure tunnel relative to sea level, $\beta_{s,j}$, $\beta_{m,j}$ and $\beta_{e,j}$ is angle between x direction and the line passing through the gravity center of water body WB1, WB2, WB3 and axial origin respectively, $D_{j,i}$ and $A_{j,i}$ is diameter and sectional area of the pressure tunnel in the intake respectively, j denotes plant index, $X_{s,j}$, $X_{m,j}$ and $X_{e,j}$ is starting point of water body WB1, WB2 and WB3 in x direction, Y_j is width of the dam, $\gamma_{s,j,i}$, $\gamma_{m,j,i}$ and $\gamma_{e,j,i}$ is angle of the water body WB1, WB2 and WB3 between the center line of x direction and the pressure tunnel of unit i in reservoir j respectively, $T_{\max,j,i}$ is maximal utilization hours for the rated capacity of hydroelectric generating unit i in hydroelectric plant j, $N_{R,j}$ is year number of a scheduling period.

The electric power $P_{H,j,i}$ of a generator is formulated:

$$P_{H,j,i} = \frac{E_{H,j,i}}{T} \quad \textbf{(8)}$$

where T is scheduling period of the hydroelectric plants.

For a unit time(one second), $P_{H,j,i} = E_{H,j,i}$.

3 Energy Consumption of Electric Power Production

3.1 Water Consumption Volume Increment Rate

For a hydropower-driven generator, the variation of electric energy is obtained by differentiating Equation (1) with respect to $Q_{G,j,i}$:

$$\Delta E_{H,j,i} = [\partial f_1 + \partial f_2 + \partial f_3 + \partial f_4 + \partial f_5 + \partial f_6] \cdot \Delta Q_{G,j,i}$$

$$= \frac{\partial f_1 + \partial f_2 + \partial f_3 + \partial f_4 + \partial f_5 + \partial f_6}{T} \cdot \Delta W_{H,j,i} \quad \textbf{(23)}$$

where

$$\Delta f_1 = 9.81[(H_j(x,t) - H_{I,j,i}) - p_{O,j,i})] \quad \textbf{(24)}$$

$$\Delta f_2 = 9.81 * \frac{1}{2g}[v_{I,j,i}^2 - v_{O,j,i}^2] \quad \textbf{(25)}$$

$$\Delta f_3 = 9.81[H_{I,j,i} - H_{O,j,i}(t)] \quad \textbf{(26)}$$

$$\Delta f_4 = \frac{9.81 X_{s,j} Y_j [H_j(x,t) - H_{I,j,i}]}{Y_j [H_j(x,t) - H_{I,j,i}]} \cdot$$

$$\sin \beta_{s,j} \cos(\alpha_{I,j,i} - \beta_{s,j}) \cos^2 \gamma_{s,j,i} \qquad \textbf{(27)}$$

$$\Delta f_5 = \frac{9.81 Y_j (X_{m,j} - X_{s,j})(2H_j(x,t) - H_{m,j} - H_{I,j,i})}{2Y_j [H_j(x,t) - H_{I,j,i}]} \cdot$$

$$\sin \beta_{m,j} \cos(\alpha_{I,j,i} - \beta_{m,j}) \cos^2 \gamma_{m,j,i} \qquad \textbf{(28)}$$

$$\Delta f_6 = \frac{9.81 Y_j (X_{e,j} - X_{m,j})(H_j(x,t) - H_{m,j})}{3Y_j [H_j(x,t) - H_{I,j,i}]} \cdot$$

$$\sin \beta_{e,j} \cos(\alpha_{I,j,i} - \beta_{e,j}) \cos^2 \gamma_{e,j,i} \qquad \textbf{(29)}$$

Water consumption volume increment rate is defined to be a ratio of the variation of the water consumption volume and the variation of electric power output of a hydropower-driven generator:

$$\lambda_{H,j,i} = \frac{\Delta W_{H,j,i}}{\Delta E_{H,j,i}} = \frac{T}{\partial f_1 + \partial f_2 + \partial f_3 + \partial f_4 + \partial f_5 + \partial f_6}$$

$$= \frac{T \Delta Q_{G,j,i}}{(\partial f_1 + \partial f_2 + \partial f_3 + \partial f_4 + \partial f_5 + \partial f_6) \Delta Q_{G,j,i}}$$

$$= \frac{T \Delta Q_{G,j,i}}{\Delta E_{H,j,i}} \qquad \textbf{(30)}$$

3.2 Coal Consumption Volume Increment Rate

For a thermal power-driven generator, the coal consumption volume is formulated as a quadratic function of electric power, as shown in the following form:

$$F_{T,k,l} = a_{T,k,l} E_{T,k,l}^2 + b_{T,k,l} E_{T,k,l} + c_{T,k,l} \qquad \textbf{(31)}$$

where $F_{T,k,l}$ and $E_{T,k,l}$ is respectively coal consumption volume and electric power of a thermal power-driven generator; $a_{T,k,l}$, $b_{T,k,l}$, $c_{T,k,l}$ is respectively coefficient of coal consumption volume of a thermal power-driven generator.

The variation of coal consumption volume is obtained by differentiating Equation (25) with respect to $E_{T,j,i}$:

$$\Delta F_{T,k,l} = (2a_{T,k,l} E_{T,k,l} + b_{T,k,l}) \Delta E_{T,k,l} \qquad \textbf{(32)}$$

Coal consumption volume increment rate is defined to be a ratio of the variation of the coal consumption volume and the variation of electric power output of a thermal power-driven generator:

$$\lambda_{T,k,l} = \frac{\Delta F_{T,k,l}}{\Delta E_{T,k,l}} = 2a_{T,k,l} E_{T,k,l} + b_{T,k,l} \qquad \textbf{(33)}$$

4 Optimal Scheduling Models for Hydro-Thermal Systems

Water is one of renewable energy, which is an energy source that can be replenished in a short period of time, and is mainly used for electric energy production. Coal is non-renewable energy, which is an energy source that may be used up and cannot be recreated in a short period of time. In order to make as possible as best use of renewable resource, water must be placed on more prior consideration for electric energy production than coal. For this purpose, the objective of scheduling optimization of hydro-thermal power systems must minimize the water consumption volume consumed in electric energy production, including the water consumption volume consumed in hydro-electric plants and the water consumption volume exchanged from coal consumption volume consumed in coal-fired electric plants:

$$\min \sum_{t=1}^{T} [\sum_{j=1}^{N_H} \sum_{i=1}^{N_{HG}} W_{H,j,i} + \sum_{k=1}^{N_T} \sum_{l=1}^{N_{TG}} \gamma_{T,k,l} F_{T,k,l}] \qquad \textbf{(34)}$$

where N_H and N_{HG} is respectively number of hydroelectric plants and hydro-driven generators in plant j, N_T and N_{TG} is respectively number of coal-fired electric plants and coal-fired generators, $\gamma_{T,k,l}$ is a coefficient exchanging coal consumption volume consumed in coal-fired electric plants into water consumption volume, and it is formulated:

$$\gamma_{T,k,l} = \frac{\lambda_{H,adv}}{\Delta F_{T,k,l} / \Delta E_{T,k,l}} \qquad (35)$$

where $\lambda_{H,adv}$ is average water consumption volume increment rate of all hydro-driven generators:

$$\lambda_{H,adv} = \frac{\sum_{j=1}^{N_H}\sum_{i=1}^{N_{HG}} \lambda_{H,j,i}}{N_H N_{HG}} \quad \textbf{(36)}$$

The constraint conditions include:

1) Equality constraint for electric power of hydro-thermal power systems: at any time t, the sum of the electric power produced by hydro-driven generators and coal-fired generators must be hold to be equal to load-demanded power:

$$\sum_{j=1}^{N_H}\sum_{i=1}^{N_{HG}} P_{H,j,i}(t) + \sum_{k=1}^{N_T}\sum_{l=1}^{N_{TG}} P_{T,k,l}(t) - P_L(t) = 0 \quad \textbf{(37)}$$

where $P_L(t)$ is load-demanded power at any time t.

2) Equality constraint for electric energy of hydro-thermal power systems: in the scheduling period T, the sum of the electric energy produced by hydro-driven generators and coal-fired generators must be hold to be equal to load-demanded energy:

$$\sum_{j=1}^{N_H}\sum_{i=1}^{N_{HG}} E_{H,j,i}(T) + \sum_{k=1}^{N_T}\sum_{l=1}^{N_{TG}} E_{T,k,l}(T) - E_L(T) = 0 \quad \textbf{(38)}$$

where $E_L(T)$ is load-demanded energy in the scheduling period T.

3) Inequality constraint for active and reactive power of hydro-driven generators:

$$\underline{P}_{H,j,i} \le P_{H,j,i} \le \overline{P}_{H,j,i} \quad \textbf{(39)}$$

$$\underline{Q}_{H,j,i} \le Q_{H,j,i} \le \overline{Q}_{H,j,i} \quad \textbf{(40)}$$

where $\underline{P}_{H,j,i}$, $\underline{Q}_{H,j,i}$ and $\overline{P}_{H,j,i}$, $\overline{Q}_{H,j,i}$ is respectively the lower and upper limited value of active and reactive power of hydro-driven generator i in plant j.

5) Inequality constraint for active and reactive power of coal-fired generators:

$$\underline{P}_{T,k,l} \le P_{T,k,l} \le \overline{P}_{T,k,l} \quad \textbf{(41)}$$

$$\underline{Q}_{T,k,l} \le Q_{T,k,l} \le \overline{Q}_{T,k,l} \quad \textbf{(42)}$$

where $\underline{P}_{T,k,l}$, $\underline{Q}_{T,k,l}$ and $\overline{P}_{T,k,l}$, $\overline{Q}_{T,k,l}$ is respectively the lower and upper limited value of active and reactive power of coal-fired generator l in plant k.

6) Inequality constraint for generation flow:

$$\underline{Q}_{G,j,i} \le Q_{G,j,i} \le \overline{Q}_{G,j,i} \quad \textbf{(43)}$$

where $\underline{Q}_{G,j,i}$ and $\overline{Q}_{G,j,i}$ is respectively the lower and upper limited value of generation flow of hydro-driven generator i in plant j.

7) Inequality constraint for coal consumption volume:

$$F_{down,k} \le \sum_{l=1}^{N_{TG}} F_{T,k,l} \le F_{up,k} \quad \textbf{(44)}$$

where $F_{up,k}$ and $F_{down,k}$ is maximal limit and minimal limit of coal consumption volume of coal-fired electric plant k in the scheduling period T.

8) Inequality constraint for water consumption volume:

$$W_{down,j} \le \sum_{i=1}^{N_{HG}} W_{H,j,i} \le W_{up,j} \quad \textbf{(45)}$$

where $W_{up,j}$ and $W_{down,j}$ is maximal limit and minimal limit of water consumption volume of hydro-electric plant j in the scheduling period T.

9) Inequality constraint for water consumption volume and coal consumption volume: for a whole, the coal consumption volume exchanged using water consumption volume of all hydro-driven generators is required to be greater than that consumed by all coal-fired generators:

$$\sum_{t=1}^{T}\sum_{j=1}^{N_H}\sum_{i=1}^{N_{HG}} \gamma_{C,j,i} W_{H,j,i} > \sum_{t=1}^{T}\sum_{k=1}^{N_T}\sum_{l=1}^{N_{TG}} F_{T,k,l} \quad \textbf{(46)}$$

where $\gamma_{C,j,i}$ is a coefficient exchanging water consumption volume consumed in hydro-electric plants into coal consumption volume, and it is formulated:

$$\gamma_{C,j,i} = \frac{\lambda_{T,adv}}{\Delta W_{H,j,i} / \Delta E_{H,j,i}} \quad \textbf{(47)}$$

where $\lambda_{T,adv}$ is average coal consumption volume increment rate of all coal-fired generators:

$$\lambda_{T,adv} = \frac{\sum_{k=1}^{N_T}\sum_{l=1}^{N_{TG}}\lambda_{T,k,l}}{N_T N_{TG}} \quad \textbf{(48)}$$

At the same time, the water consumption volume exchanged from coal consumption volume of all coal-fired generators is required to be smaller than that consumed by all hydro-driven generators:

$$\sum_{t=1}^{T}\sum_{j=1}^{N_H}\sum_{i=1}^{N_{HG}} W_{H,j,i} > \sum_{t=1}^{T}\sum_{k=1}^{N_T}\sum_{l=1}^{N_{TG}} \gamma_{W,k,l} F_{T,k,l} \quad \textbf{(49)}$$

10) Equality constraint related to saved-water level: during high-water period, normal-water period, low water period, and flood period, saved-water level is required to be retained at a fixed value:

$$H_j(t) = \begin{cases} H_{LP,j} & \text{for LP} \\ H_{HP,j} & \text{for HP} \\ H_{NP,j} & \text{for NP} \\ H_{FP,j} & \text{for FP} \end{cases} \quad \textbf{(50)}$$

where $H_{LP,j}$, $H_{HP,j}$, $H_{NP,j}$ and $H_{FP,j}$ is a required saved-water level at time t in reservoir j for high-water period, normal-water period, low water period, and flood period respectively.

11) Equality constraint for variation of saved-water level: in the scheduling period T, the variation of saved-water level in reservoir j is required to be equal to zero:

$$\sum_{t=1}^{T}\sum_{j=1}^{N_H} \Delta H_j(t) = 0 \quad \textbf{(51)}$$

12) Inequality constraint for water energy total: at time t, the water energy total of cascaded hydroelectric plants is required to be no smaller than a designed value:

$$N_{R,j}(3600 * T_{\max,j,i}) \sum_{j=1}^{N_H}\sum_{i=1}^{N_{HG}} E_{H,j,i}(H_j, Q_{G,j,i}) \geq E_A \quad \textbf{(52)}$$

where E_A is designed value of the water energy total of cascaded hydroelectric plants:

$$E_A = N_{R,j}(3600 * T_{\max,j,i}) \sum_{j=1}^{N_H}\sum_{i=1}^{N_{HG}} E_{H,j,i}(H_{D,j}, Q_{GN,j,i}) \quad \textbf{(53)}$$

where $H_{D,j}$ and $Q_{GN,j,i}$ is respectively the designed saved-water level and normal generation flow of hydro-driven generator i in plant j.

13) Inequality constraint for minimal saved-water level:

$$H_j(x,t) - H_{I,j,i} \geq p_{O,j,i} \quad \textbf{(54)}$$

5 Study Examples and Analysis

In this paper, Guangxi electric power system including Hongshuihe hydroelectric stations in Hongshuihe river is taken for a studying example. The data for Hongshuihe hydroelectric plants and coal-fired electric plants in Guangxi electric power system is shown in Table 1 and Table 2 respectively. In the following section, three cases are given to illustrate the component and factor analytic method for optimal electric energy production of thermal power systems in one hour.

According to the objective to minimize the sum of the water-consumed volume used for electric energy production in 8 cascaded hydroelectric plants and the water-consumed volume converted from coal-consumed volume by 12 coal-fired plants, the plant with smaller water-consumed volume or coal-water-consumed volume is the first one to be scheduled to generate. As shown in Table 1 and 2, the plants with greater rated install capacity have smaller water-consumed volume or coal to water volume in per unit electric energy output, while the plants with smaller rated install capacity have greater water-consumed volume or coal to water volume in per unit electric energy output.

In high in-flow period, the reservoir inflow in each cascaded hydroelectric plant is assumed to be high. In this case, the water flow and water volume for electric energy production in each cascaded reservoir is available. Because of much more available water flow for electric energy production and smaller water-consumed volume

Table 1. The data for Hongshuihe hydroelectric plants

Item	Unit	Tian sheng qiao No.1	Tian sheng qiao No.2	Ping ban	Long tan	Yan tan	Da hua	Bai long tan	Le tan
Plant No.		H1	H2	H3	H4	H5	H6	H7	H8
Reservoir Regulation		over-years	daily	daily	over-years	seasonal	runoff	runoff	runoff
Regulation capacity	Gm^3	5.796	0.0184	0.0268	11.15	2.34	0.043	0.047	0.46
Electric energy produced in one year	G·kWh	5.62	8.20	1.60	15.6	5.66	2.06	0.95	2.99
Rated Installe capacity	MW	4*300	6*200	3*135	7*600	4*302.5	4*114	6×32	4*150
Generation flow	m^3/s	301.3	139.8	440. 29	556	580	606	377.5	863.9
Water head	m	110.7	176.0	34.0	125	60.8	22.0	9.7	19.5
Saved-water height	m	49	8	2.5	45	4	4	1	2
Average flow	m^3/s	612	615	634	1610	1740	1990	2020	2050
Saved-water Level	m	780	645	440	375	223	157	126	112
$H_{m,j}$	m	750	641	438.5	345	221	155	125.5	111
$H_{I,j}$	m	731	637	437.5	330	219	153	125	110
$H_{O,j}$	m	620.3	461	403.5	205	158.2	131	115.3	90.5
$X_{s,j}$	m	6000	1000	1300	8000	8500	1300	500	1600
$X_{m,j}$	m	16000	3000	8300	16000	18000	5500	6000	8000
$X_{e,j}$	m	520000	17500	109600	1465800	6610000	34600	72600	190000
Average in-Flow	m^3/s	612	615	634	1610	1740	1900	1910	2050
Lowest in-Flow	m^3/s	306	307	317	805	870	950	1010	102
High in-Flow	m^3/s	2203	2214	2882	4150	4550	4840	5272	5380
Normal in-Flow	m^3/s	1024	1030	1068	2520	2860	3100	3340	3510
Pipe Dia.	m	8	9	9	10	10	10	7.5	11
Pipe Angle	degree	50°	50°	50°	50°	50°	50°	50°	50°
Bar length	m	1104	470	395.5	735.5	525	1160	274	630
Bar height	m	178	58．5	62.2	192216.5	110	78．5	28	63
Height of bar top	m	791	658.7	449.2	382	233	174.5	135	130
Water volume consumed in per unit electric energy output	m^3/kWh	3.6161	2.5147	11.7393	3.3364	6.9034	19.1357	42.4738	20.7343

Table 2. The data for coal-fired plants

Plant No.	T1	T2	T3	T4	T5	T6	T7	T8	T9	T10	T11	T12
Installed capacity/MW	2*600	2*600	2*600	2*600	2*300	2*125	2*360	2*330	2*220	2*135	2*300	2*135
a_T /g/kWh^2	92.6156	39.3645	190.0658	179.0296	761.3214	981.0396	271.1672	47.7373	59.599	672.6546	751.5795	763.6358
b_T /g/kWh	-111140	-47238.41	-228080.2	-214836.6	-456794.3	-245266	-195243.7	-31508.7	-26226.2	-181620	-450950	-206198
c_T /g($\times 10^8$)	1.756	1.445	2.1068	2.0245	1.4991	0.51579	1.309	0.94728	0.66685	0.52489	1.4903	0.54147
W_{Tn}	4.2125	3.8592	4.2124	4.0863	4.8203	16.9678	4.7258	4.8202	16.9696	17.4374	4.8200	17.4376

W_{Tn} : Coal to water volume consumed in per unit electric energy output

Table 3. The electric power dispatch of hydro-thermal power systems and electric power of single machine for different load level in high in-flow hour

Load	MW	4238.76	6162.34	8288.27	10249.36	13369.92	16270.73	17936.46
MW of hydro plant	MW	4238.76	6162.34	6599.37	6599.37	6599.37	8214.20	9326.46
MW of coal-fired plant	MW	0.00	0.00	1688.90	3649.99	6770.55	8056.53	8610.00
MW of H1 plant	MW	4*0.00	4*190.70	4*299.96	4*299.96	4*299.96	4*299.96	4*299.96
MW of H2 plant	MW	6*200.00	6*200.00	6*200.00	6*200.00	6*200.00	6*200.00	6*200.00
MW of H3 plant	MW	3*0.00	3*0.00	3*0.00	3*0.00	3*0.00	3*135.00	3*135.00
MW of H4 plant	MW	7*434.11	7*599.93	7*599.93	7*599.93	7*599.93	7*599.93	7*599.93
MW of H5 plant	MW	4*0.00	4*0.00	4*0.00	4*0.00	4*0.00	4*302.46	4*302.46
MW of H6 plant	MW	4*0.00	4*0.00	4*0.00	4*0.00	4*0.00	4*0.00	4*114.00
MW of H7 plant	MW	6*0.00	6*0.00	6*0.00	6*0.00	6*0.00	6*0.00	6*9.38
MW of H8 plant	MW	4*0.00	4*0.00	4*0.00	4*0.00	4*0.00	4*0.00	4*149.99
MW of T1 plant	MW	2*0.00	2*0.00	2*0.00	2*312.30	2*600.00	2*600.00	2*600.00
MW of T2 plant	MW	2*0.00	2*0.00	2*600.00	2*600.00	2*600.00	2*600.00	2*600.00
MW of T3 plant	MW	2*0.00	2*0.00	2*0.00	2*312.70	2*600.00	2*600.00	2*600.00
MW of T4 plant	MW	2*0.00	2*0.00	2*244.45	2*600.00	2*600.00	2*600.00	2*600.00
MW of T5 plant	MW	2*0.00	2*0.00	2*0.00	2*0.00	2*133.60	2*300.00	2*300.00
MW of T6 plant	MW	2*0.00	2*0.00	2*0.00	2*0.00	2*0.00	2*125.00	2*125.00
MW of T7 plant	MW	2*0.00	2*0.00	2*0.00	2*0.00	2*360.00	2*360.00	2*360.00
MW of T8 plant	MW	2*0.00	2*0.00	2*0.00	2*0.00	2*191.67	2*330.00	2*330.00
MW of T9 plant	MW	2*0.00	2*0.00	2*0.00	2*0.00	2*0.00	2*212.78	2*220.00
MW of T10 plant	MW	2*0.00	2*0.00	2*0.00	2*0.00	2*0.00	2*0.49	2*135.00
MW of T11 plant	MW	2*0.00	2*0.00	2*0.00	2*0.00	2*300.00	2*300.00	2*300.00
MW of T12 plant	MW	2*0.00	2*0.00	2*0.00	2*0.00	2*0.00	2*0.00	2*135.00

Table 4. The electric energy production of hydro-thermal power systems and energy component of hydro plants for different load level in high in-flow hour

Load	MW	6162.34	10249.36	13369.92	16270.73	17936.46
Electric energy produced in T	kWh	6162340.00	10249360.00	13369920.00	16270730.00	17936460.00
E_T /percentage	kWh	6162340.00/100.00	6599366.45/64.39	6599366.45/49.36	8214200.36/50.48	9326460.00/52.00
E_G /percentage	kWh	0.00/0.00	3649993.55/35.61	6770553.55/50.64	8056529.64/49.52	8610000.00/48.00
Share of f_1 in E_G /percentage	kWh	176170.75/2.8588	185478.51/2.8106	185478.51/2.8106	240112.90/2.9231	365469.36/3.9186
Share of f_2 in E_G /percentage	kWh	21763.80/0.3532	24708.59/0.3744	24708.59/0.3744	45305.26/0.5515	82046.25/0.8797
Share of f_3 in E_G /percentage	kWh	5265952.61/85.453	5609409.21/84.999	5609409.21/84.999	7141210.74/86.937	8078269.18/86.616
Share of $f_4 + f_5 + f_6$ in E_G /percentage	kWh	698452.84/11.3342	779770.13/11.8158	779770.13/11.8158	787571.45/9.5879	800675.21/8.5850

in per unit electric energy output, the hydroelectric plants have much more superiority to be scheduled for electric energy production than coal-fired plants when the load is smaller. For example, when the load is 4238.76MW, the hydroelectric plant H2 is first in full power output, and plant H4 is for the remainder of the load; when the load is 6162.34MW, H2 and H4 is first in full power output, and H1 is for the remainder of the load, as shown in Table 3. With increases in the load, the coal-fired plants with smaller coal-water consumption volume are also gradually put into schedule for electric energy production till the load arrives at the sum of the rated install capacity of all hydroelectric and coal-fired plants, as shown in Table 3.

Table 4 shows the electric energy production of hydro-thermal power systems and energy component of hydro plants for different load level in high in-flow hour. When the load is small, higher percentage of electric energy production is shared by hydroelectric plants than coal-fired plants, while lower percentage is shared by hydroelectric plants than coal-fired plants, as shown in Table 4. With increase in load, the percentage shared by hydroelectric plants increases, while the percentage shared by coal-fired plants decreases, as shown in Figure 2 and Figure 3. It is also seen that for a load of about 7000MW of load, hydroelectric plants take 100% and coal-fired plants takes 0.

With increase in load, the percentage shared by hydroelectric plants increases, while the percentage shared by coal-fired plants decreases, as shown in Figure 2 and Figure 3. It is also seen that for small than about 7000MW of load, hydroelectric plants take 100% and coal-fired plants takes 0.

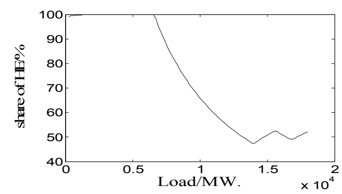

Figure 2. Sharing percentage of electric energy produced by hydro plants (HE: Electric energy produced by hydro plants)

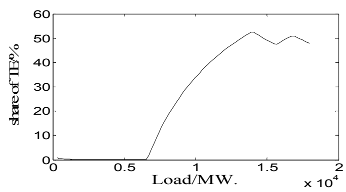

Figure 3. Sharing percentage of electric energy produced by coal-fired plants(TE: Electric energy produced by hydro plants)

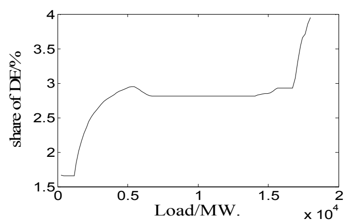

Figure 4. Sharing percentage of electric energy converted from water-deep pressure energy (DE: Electric energy converted from water-deep pressure energy)

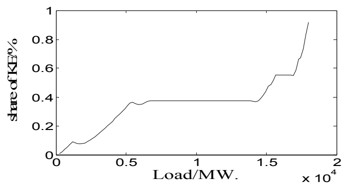

Figure 5. Sharing percentage of electric energy converted from kinetic energy (KE: Electric energy converted from kinetic energy)

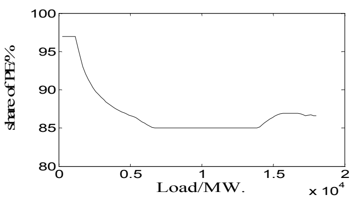

Figure 6. Sharing percentage of electric energy converted from potential energy (PE: Electric energy converted from potential energy)

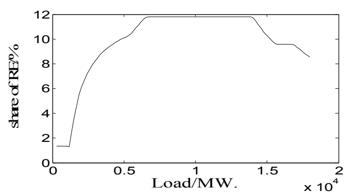

Figure 7. Sharing percentage of electric energy converted from reservoir energy (RE: Electric energy converted from reservoir energy)

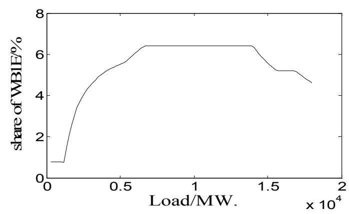

Figure 8. Sharing percentage of electric energy converted from reservoir energy in WB1 (WB1E: Electric energy converted from reservoir energy in WB1)

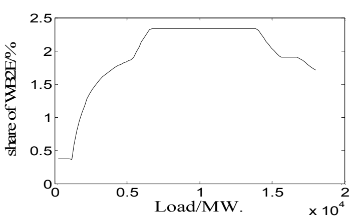

Figure 9. Sharing percentage of electric energy converted from reservoir energy in W

With increase in load, water-deep pressure energy and kinetic energy increases, as shown in Figure 4 and Figure 5, and potential energy decreases, as shown in Figure 6, while reservoir energy increases first, and

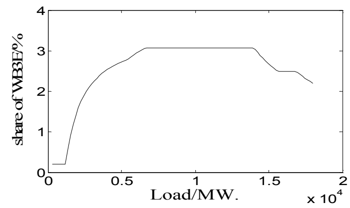

Figure 10. Sharing percentage of electric energy converted from reservoir energy in WB3

then decreases, as shown in Figure 7. It is also seen that these percentage retains constant from 7000MW to 14000MW.

With increase in load, the percentage of electric energy converted from reservoir energy of reservoir water body WB1, WB2 and WB3 included in the total electric energy produced by hydroelectric plants all increases, but retains constant from 7000MW to 14000MW, as shown in Figure 8-Figure 10.

6 Conclusions

1) Optimal scheduling for electric energy production of hydro-thermal power systems depends on such factors as load demand, the water-consumed volume increment rate, the in-flow of reservoir, and so on. The plant with low water-consumed volume increment rate is first scheduled for electric energy production, and the plant with the highest water-consumed volume increment rate is finally scheduled for production.

2) In different flow hour, the sharing percentage of the electric energy produced by hydroelectric and coal-fired plants is dependent on some factors, such as the demand load, the coming flow of reservoir, and so on. In high in-flow hour, the percentage shared by hydroelectric plants may be high for small load demand and is low for great load, while the percentage shared by coal-fired plants may be low for small load demand and is high for great load. In low in-flow hour, the percentage shared by hydroelectric plants may be low for any load demand, while the percentage shared by coal-fired plants may be high for any load demand.

Acknowledgements

The author greatly acknowledges the financial support of the National High Technology Research and Development Program of China (863 Program) (2007AA04Z 197), National Natural Science Foundation of China (50767001), Nature Science Foundation of Guangxi (0640028), Program for 100 Young and Middle-aged Disciplinary Leaders in Guangxi Higher Education Institutions (RC20060808002), Science and Technology Project of Guangxi Education Administration (200808 MS150) and Guangxi Innovation Plan in Graduate Education.

REFERENCES

[1] Fleten S. E., Wallace S. W., and Ziemba W. T., "Portfolio management in a deregulated hydropower based electricity market," In Proceedings of the 3rd International Conference on Hydropower Development, pp. 197-204, 1997.

[2] Fleten S. E., Wallace S. W., and Ziemba W. T., "Hedging electricity portfolios via stochastic programming," IMA volumes on Mathematics and Its Applications, Vol. 128, pp. 71-93, 2002.

[3] Ilyas Eker, "The design of robust multi-loop-cascaded hydro governors," Engineering Computer, Vol. 20, No. 2, pp. 45-53, 2004.

[4] Wallace S. W. and Fleten S. E., "Stochastic programming models in energy," The series Handbooks in Operations Research and Management Science, Vol. 10, pp. 637-677, 2003.

[5] Guan X., Svoboda A., and Li C. A., "Scheduling hydro power systems with restricted operating zones and discharge ramping constraints," IEEE Transactions on Power System, Vol.14, No.1, pp. 126-131, 1999.

[6] Yang J. S., and Chen N, "Short term hydrothermal coordination using multipass dynamic programming," IEEE Transactions on Power System, Vol. 4, No. 3, pp. 1050-1056, 1989.

[7] Li C., Jap P., and Streiffert D, "Implementation of network flow programming to the hydrothermal coordination in an energy management system," IEEE Transactions on Power System, Vol. 8, No. 3, pp. 1045-1053, 1993.

[8] Rosenthal R. E., "A nonlinear network flow algorithm for maximization of benefits in a hydroelectric power system," Operation Research, Vol. 29, No. 4, pp. 763-786, 1981.

[9] Chang G. W., Aganagic M., Waight J. G., et al., "Experiences with mixed integer linear programming based approaches on short-term hydro scheduling," IEEE Transactions on Power Systems, Vol. 16, No. 4, pp. 743-749, 2001.

[10] Conejo A. J., Arroyo J. M., Contreras J., et al., "Self-scheduling of a hydro producer in a pool-based electricity market," IEEE Transactions on Power System, Vol. 17, No. 4, pp. 1265-1272, 2002.

[11] Chang G., Mohamed Aganagic W, Waight James G, et al., "Experiences with mixed integer linear programming based approaches on short-term hydro scheduling," IEEE Transactions on Power System, Vol. 16, No. 4, pp. 743-749, 2001.

[12] Nilsson O. and Sjelvgren D., "Mixed integer programming applied to short-term planning of a hydro-thermal system," IEEE Transactions on Power System, Vol. 11, No. 1, pp. 281-286, 1996.

[13] Sinha N., Chakrabarti R., and Chattopadhyay P. K., "Fast evolutionary programming techniques for short-term hydrothermal scheduling," Electric Power Systems Research, Vol. 66, pp. 97-103, 2003.

[14] Zoumas C. E., Bakirtzis A. G., Theocharis J. B., et al., "A genetic algorithm solution approach to the hydrothermal coordination problem," IEEE Transactions on Power System, Vol. 19, No. 2, pp. 1356-1364, 2004.

[15] Guan X., Ni E., and Li R., "An optimization-based algorithm for scheduling hydrothermal power systems with cascaded reservoirs and discrete hydro constraints," IEEE Transactions on Power System, Vol. 12, No. 4, pp. 1775-1780, 1997.

[16] Jiang C. W. and Etorre B., "A self-adaptive chaotic particle swarm algorithm for short term hydroelectric system scheduling in deregulated environment," Energy Conversion and Management, Vol. 46, No. 17, pp. 2689-2696, 2005.

[17] Yu B. H., Yuan X. H., and Wang J. W., "Short-term hydro-thermal scheduling using particle swarm optimization method," Energy Conversion and Management, Vol. 48, No. 7, pp. 1902-1908, 2007.

[18] Umayal S. P. and Kamaraj N., "Stochastic multi objective short term hydrothermal scheduling using particle swarm optimization," In Indicon Annual IEEE, pp. 497−501, 2005.

[19] Esmin A. A. A., Lambert-Torres G., and Zambroni de Souza A. C., "A hybrid particle swarm optimization applied to loss power minimization," IEEE Transactions on Power System, Vol. 20, No. 2, pp. 855-859, 2005.

[20] Abido M. A., "Optimal power flow using particle swarm optimization," Electrical Power Energy System, Vol. 24, pp. 563-571, 2002.

[21] Zambelli M., Siqueira T. G., Cicogna M., et al., "Deterministic versus stochastic models for long term hydrothermal scheduling," In Proceedings of IEEE Power Engineering Society General Meeting, 2006.

[22] Heredia F. J., Nabonal N. L., "Optimum short-term hydrothermal scheduling with spinning reserve through network flows," IEEE Transactions on Power System, Vol. 10, No. 3, pp. 1642-1651, 1995.

Call for Papers

Asia-Pacific Power and Energy Engineering Conference (APPEEC 2010)

March 28-31, 2010 Chengdu, China

http://www.scirp.org/conf/appeec2010

This conference is sponsored by IEEE Power & Energy Society (PES), State Grid of China, Sichuan University, Chongqing University and Wuhan University. The conference proceedings will be published by IEEE. **All papers accepted will be included in IEEE Xplore and indexed by EI and ISTP.** This conference will be held in Chengdu where "The Land of Abundance" is located.

Sponsors: IEEE Power Engineering Society (PES), State Grid of China, Sichuan University, Chongqing University and Wuhan University.

Topics

Power Generation-Conventional and Renewable

- Hydropower technologies and applications
- Thermal power technologies and applications
- Nuclear energy generation and utilization
- Wind power generation and utilization
- Bio-energy technologies, process and utilization
- Geothermal and tidal wave energy
- Photovoltaic for solar power application
- New technologies and design for energy efficiency
- New technologies for minimizing CO2 generation
- Environmental-friendly technologies for power generation

Power Transmission and Distribution

- Ultra High Voltage (UHV) technologies
- HVDC and flexible AC transmission system (FACTS)
- Over-voltage, lightning protection and grounding
- Electromagnetic transient in high voltage power systems
- Insulation condition monitoring in power systems
- Advanced distribution and SCADA technologies
- Electromagnetic compatibility in power systems
- Plasma physics and the pulsed power technology
- Electromagnetic analysis in power systems

Power System Management

- Power system management technologies
- Integrated substation automation technologies
- Power system monitoring and mitigation technologies
- Online monitoring and fault diagnosis system
- Control strategies for modern power system stability
- Modeling and simulation of large power systems
- Application of wide area measurement system (WAMS)
- Power system analysis and optimization
- Load modeling, estimation and forecast
- Power system planning and operation

Smart Grid

- Concept and structure frame
- Operation and control
- Distributed generation and renewable energy application
- Information and smart meter reading
- Integrated energy and communications

Submission Requirements: The working language of the conference is English. All papers must be submitted in IEEE electronic format. Instructions and full information on the conference are posted on the conference website. Anyone wishing to propose a special session or a tutorial should contact us: appeec@scirp.org.

Important Dates:

Sept. 30, 2009 Deadline for Full Paper Submission

Nov. 30, 2009 Notification of Acceptance

Contact Information:

Website: http://www.scirp.org/conf/appeec2010

E-mail: appeec@scirp.org

Energy and Power Engineering, 2009, 01-64
Published Online August 2009 in SciRes (http://www.scirp.org/journal/epe).

TABLE OF CONTENTS

Volume 1, Number 1, August 2009

ISSN: 1949-243X

977194924300X 01